

# Photophysical Characterizations of OLED Relevant Cu(I) Complexes Exhibiting Thermally Activated Delayed Fluorescence (TADF)



Dissertation

zur Erlangung des Doktorgrades der Naturwissenschaften (Dr. rer. nat.)  
an der Fakultät für Chemie und Pharmazie  
der Universität Regensburg

vorgelegt von  
**Markus J. Leitl**  
aus Winzer

2015





Promotionsgesuch eingereicht am: 22. Januar 2015  
Tag der mündlichen Prüfung: 9. März 2015

Die Arbeit wurde angeleitet von Prof. Dr. Hartmut Yersin am Institut für  
Physikalische und Theoretische Chemie der Universität Regensburg.

Prüfungsausschuss: Prof. Dr. Werner Kunz, Vorsitzender  
Prof. Dr. Hartmut Yersin, Erster Gutachter  
Prof. Dr. Bernhard Dick, Zweiter Gutachter  
Prof. Dr. Alfons Penzkofer

## Parts of this thesis have been published previously

**Markus J. Leidl**, Valentina A. Krylova, Peter I. Djurovich, Mark E. Thompson, Hartmut Yersin

*Phosphorescence versus Thermally Activated Delayed Fluorescence. Controlling Singlet-Triplet Splitting in Brightly Emitting and Sublimable Cu(I)-Compounds*

Journal of the American Chemical Society **2014**, *136*, 16032.

Hartmut Yersin, **Markus J. Leidl**, Rafał Czerwieńiec

*TADF for Singlet Harvesting – Next Generation OLED Materials Based on Brightly Green and Blue Emitting Cu(I) and Ag(I) Compounds*

Proceedings of the SPIE **2014**, *9183*, 91830N-1.

Charlotte L. Linfoot, **Markus J. Leidl**, Patricia Richardson, Andreas F. Rausch, Oleg Chepelin, Fraser J. White, Hartmut Yersin, Neil Robertson

Selected as cover article

*Thermally Activated Delayed Fluorescence (TADF) and Enhancing Photoluminescence Quantum Yields of [Cu<sup>I</sup>(diimine)(diphosphine)]<sup>+</sup> Complexes – Photophysical, Structural, and Computational Studies*

Inorganic Chemistry **2014**, *53*, 10854.

**Markus J. Leidl**, Fritz-Robert KÜchle, Hermann A. Mayer, Lars Wesemann, Hartmut Yersin

*Brightly Blue and Green Emitting Cu(I) Dimers for Singlet Harvesting in OLEDs*

The Journal of Physical Chemistry A **2013**, *117*, 11823.

## Further publications

Daniel A. Kunz, **Markus J. Leitl**, Lukas Schade, Jasmin Schmid, Beate Bojer, Ulrich T. Schwarz, Geoffrey A. Ozin, Hartmut Yersin, Josef Breu  
*Quasi-Epitaxial Growth of [Ru(bpy)<sub>3</sub>]<sup>2+</sup> by Confinement in Clay Nanoplatelets Yields Polarized Emission*  
Small **2015**, *11*, 792.

Matthias Stöter, Bernhard Biersack, Sabine Rosenfeldt, **Markus J. Leitl**, Hussein Kalo, Rainer Schobert, Hartmut Yersin, Stefan Förster, Josef Breu  
*Encapsulation of Functional Organic Compounds in Nanoglass for Optically Anisotropic Coatings*  
Angewandte Chemie International Edition **2015**, DOI: 10.1002/anie.201411137.

Matthias Stöter, Bernhard Biersack, Sabine Rosenfeldt, **Markus J. Leitl**, Hussein Kalo, Rainer Schobert, Hartmut Yersin, Stefan Förster, Josef Breu  
*Nanoglas-Verkapselung funktionaler organischer Verbindungen für optisch anisotrope Beschichtungen*  
Angewandte Chemie **2015**, DOI: 10.1002/ange.201411137.

Timo Gneuß, **Markus J. Leitl**, Lars H. Finger, Nicholas Rau, Hartmut Yersin, Jörg Sundermeyer  
*A New Class of Luminescent Cu(I) Complexes with Tripodal Ligands – TADF Emitters for the Yellow to Red Color Range*  
Dalton Transactions **2015**, DOI: 10.1039/C4DT02631D.

Alberto Bossi, Andreas F. Rausch, **Markus J. Leitl**, Rafał Czerwieniec, Matthew T. Whited, Peter I. Djurovich, Hartmut Yersin, Mark E. Thompson  
*Photophysical Properties of Cyclometalated Pt(II) Complexes: Counterintuitive Blue Shift in Emission with an Expanded Ligand  $\pi$  System*  
Inorganic Chemistry **2013**, *52*, 12403.

Sebastian Maderlehner, **Markus J. Leitl**, Hartmut Yersin, Arno Pfitzner  
*Halocuprates(I) with DABCO Cations – Syntheses and Photophysical Characterizations*  
in preparation.

Rafał Czerwieniec, **Markus J. Leitl**, Thomas Hofbeck, Robert Meier, Hartmut Yersin  
*Unprecedentedly Long-Lived Phosphorescence of Cu(I) Complexes*  
in preparation.

## Filed patents

Timo Gneuß, **Markus J. Leitl**, Jörg Sundermeyer, Hartmut Yersin  
*Kupfer(I)- und Silber(I)-Verbindungen mit Tripod Liganden für verbessertes Singulett-Harvesting durch kombinierte Singulett- und Triplett-Emission für OLEDs und andere optoelektronische Vorrichtungen*  
filed 2014.

Rafał Czerwieniec, Thomas Hofbeck, **Markus J. Leitl**, Uwe Monkowius, Hartmut Yersin  
*Erweitertes Singulett-Harvesting für OLEDs und andere optoelektronische Vorrichtungen*  
DE102013106426A1, WO2014202675A1, filed 2013.

Rafał Czerwieniec, **Markus J. Leitl**, Hartmut Yersin  
*Optische Sauerstoff-Sensoren mit Kupfer(I)-Komplexen*  
DE102012101067A1, WO2013117460A2, WO2013117460A3, filed 2012.

Fritz-Robert Kühle, **Markus J. Leitl**, Hermann A. Mayer, Lars Wesemann, Sophie Wernitz, Hartmut Yersin  
*Komplexverbindungen mit einem Liganden mit einem N- und einem P-Donor und ihre Verwendung im opto-elektronischen Bereich*  
DE201110079856A1, EP2737557A1, WO2013014066A1, filed 2011.





# Contents

<b>Motivation</b>	<b>11</b>
<b>1 Introduction to Organic Light Emitting Diodes</b>	<b>15</b>
1.1 Electroluminescence . . . . .	15
1.2 Device Structure and Principle of Operation . . . . .	16
1.3 Triplet Harvesting and Singlet Harvesting . . . . .	20
<b>2 Photophysical Properties of Transition Metal Complexes</b>	<b>27</b>
2.1 Electronic States . . . . .	27
2.2 Spin-Orbit Coupling . . . . .	30
2.3 Temperature Dependence of Emission . . . . .	32
<b>3 Dinuclear Copper Complexes</b>	<b>35</b>
3.1 Complexes with Aminophosphine Ligands . . . . .	36
3.1.1 Crystal Structures . . . . .	36
3.1.2 Computational Investigations . . . . .	39
3.1.3 Spectroscopic Introduction . . . . .	41
3.1.4 Thermally Activated Delayed Fluorescence . . . . .	46
3.1.5 The Triplet State $T_1$ . . . . .	50
3.1.6 Concluding Remarks . . . . .	56
3.2 Complexes with Diphosphine Ligands . . . . .	58
3.2.1 DFT and TDDFT Calculations . . . . .	58
3.2.2 Spectroscopic Discussion . . . . .	60
3.2.3 Comparative Discussion and Conclusion . . . . .	63

---

<b>4 Mononuclear Copper Complexes</b>	<b>69</b>
4.1 Cu(I) Complexes with two Bidentate Ligands . . . . .	69
4.1.1 Spectroscopic Discussion . . . . .	70
4.1.2 Temperature Dependent Measurements . . . . .	77
4.1.3 Conclusion . . . . .	79
4.2 Cu(I) Complexes with Three Coordinations . . . . .	81
4.2.1 Ambient Temperature Phosphorescence versus TADF . . . . .	81
4.2.2 Compound 2 – Typical Triplet Emitter . . . . .	84
4.2.3 Compound 1 – Thermally Activated Delayed Fluorescence . . . . .	86
4.2.4 Controlling TADF by Ligand Orientation . . . . .	88
4.2.5 Conclusion . . . . .	93
<b>Experimental Section</b>	<b>97</b>
<b>Summary</b>	<b>99</b>
<b>Conclusion</b>	<b>105</b>
<b>Bibliography</b>	<b>107</b>

## Motivation

For a long time, the more than hundred years ago developed light bulb has been the most widely spread artificial light source. This could change in the near future.

Organic light-emitting diodes (OLEDs) represent a new technology for the generation of light which is highly attractive for the use in displays as well as for illumination purposes.<sup>1,2</sup> In the display sector, the application of this new technology offers clear advantages compared to state of the art liquid crystal displays (LCDs), for example, drastically higher in picture contrast, vast independence of the viewing angle, low energy consumption, and orders of magnitudes faster image refreshing rates. Furthermore, the OLED technology allows the realization of extremely thin and in addition flexible displays which opens up completely new perspectives for the design of respective devices. All these factors render OLEDs highly attractive and resulted in the fact that more and more cell phones with displays based on this technology are commercially available nowadays.

OLEDs are also assigned to possess a huge market potential in the lighting sector. However, respective products do not qualify for mass production as of yet. In Germany, this issue has been addressed by large scale research projects initiated by the “Bundesministerium für Bildung und Forschung” (German Ministry of Education and Research), for example by funding programs like “Organische Elektronik – Grundlagen der Technologie und Anwendungsszenarien” (Organic Electronics – Principles of the Technology and Scenarios for Applications).<sup>3</sup> Such research initiatives are intended to help OLEDs entering the lighting market. In this regard, the launch of pilot production lines for OLEDs for illumination purposes, one of them being located at the OSRAM OLED GmbH in Regensburg, can be seen as a big step towards this direction.<sup>4</sup>

Of particular importance for the emission and performance properties of an OLED is the emitter material used which, after the injection of electrical charges, is stimulated to emit light. It turned out that third row transition metal complexes are particularly well suited for this purpose.<sup>1</sup> In contrast to conventional fluorescent, purely organic compounds, these complexes exhibit a pronounced phosphorescence from their lowest excited triplet state with high emission quantum yields and short emission decay times.<sup>1,5-7</sup> The underlying mechanism for this is the efficient coupling of spin and orbital angular momentum induced by the central metal ion. Furthermore and most importantly, the application of phosphorescent compared to conventional fluorescent emitters results in a four times higher OLED device performance as phosphorescent materials can show the triplet harvesting effect.<sup>1,8-10</sup> This mechanism allows utilizing all electrically injected excitons, singlets and triplets, for the generation of light. For this reason, phosphorescent materials are strongly preferred to conventional fluorescent ones.

At the moment, triplet emitters based on the elements iridium and platinum are of particular relevance for commercial applications. However, this material class exhibits several disadvantages. On the one hand, iridium and platinum are noble metals that are extremely rare and therefore, emitters based on these materials are very cost intensive. This fact would render the introduction of a wide spread OLED based illumination uneconomic. On the other hand, there are problems with the photophysical properties of this material class. For example, despite intense research efforts during the last two decades the development of long-term stable and efficient emitters for the blue color range still remains a major challenge.<sup>11,12</sup>

Although copper complexes are significantly more attractive due to the drastically lower costs,<sup>13</sup> at first sight, they do not seem to be a viable alternative to the more expensive noble metal compounds. As copper possesses a considerably smaller spin orbit coupling constant compared to the distinctly heavier elements iridium and platinum it is expected that the phosphorescence decay times are significantly longer.<sup>5,6</sup> This would result in pronounced saturation effects and as a consequence in significant efficiency losses when applied in electroluminescent devices. However, if the ligands are properly chosen, copper complexes can exhibit a very small energy separation  $\Delta E(S_1 - T_1)$  between the first excited singlet  $S_1$  and triplet  $T_1$  state. Therefore, at ambient temperature a thermal population of the singlet state  $S_1$  from the energetically lower lying triplet state  $T_1$  can occur. This mechanism opens an additional, highly effective radiative decay path to the  $S_0$  ground state and represents a thermally activated delayed fluorescence (TADF).<sup>5,6</sup>

Furthermore, as the emission in this case mainly occurs via the singlet state  $S_1$ , a drastic reduction of the emission decay time is observed at ambient temperature. Importantly, emitters that exhibit a TADF also show the Singlet Harvesting effect.<sup>5,6</sup> Accordingly, when applied in OLEDs the same high efficiencies can be achieved with them as with materials exhibiting the Triplet Harvesting effect.

The attractiveness of TADF compounds for electroluminescence applications has stimulated the development of new Cu(I) based emitter materials in recent years. However, it still remains a challenge to understand the correlations between chemical structure and emission properties and therefore, to specifically develop new materials with improved luminescence properties like higher emission quantum yields and shorter emission decay times. Gaining deeper insights into these structure-property relationships and developing a more detailed understanding for the photophysical processes of Cu(I) complexes represents the motivation for this thesis.

After a brief introduction to the basic concept of electroluminescence in chapter 1, a general overview over the electronic structure of transition metal compounds is given in chapter 2. The main part of this thesis, however, focuses on the investigation of different classes of Cu(I) complexes with spectroscopic and also with computational methods. In chapter 3, the discussion hereby centers around Cu(I) complexes containing two metal ions. In the first section of this chapter complexes in which an aminophosphine ligand is coordinated to each copper center and where the two copper centers themselves are bridged by two halides are studied. This allows a detailed examination of the influence of the halide on the emission properties. In the second part, the investigations are extended to a dinuclear Cu(I) compound with diphosphine ligands and its respective Ag(I) homologue and therefore gives insight how varying the chelating ligands and the central metal ions affects the electronic structure of these complexes. In chapter 4, Cu(I) compounds with one metal center are examined. In the first part, a pair of two tetrahedrally coordinated complexes is spectroscopically characterized. It is demonstrated how a slight chemical substitution can drastically increase the emission quantum yield. In addition, the effects of the surrounding matrix environment on the emission behavior are studied in detail. The second part focuses on the investigation of two structurally related three coordinated Cu(I) compounds, one of them showing a highly effective thermally activated delayed fluorescence, the other one showing intense phosphorescence at ambient temperature. This distinct difference in the emission behavior is rationalized by applying spectroscopic and computational methods. The thesis closes with a conclusion.



# Introduction to Organic Light Emitting Diodes

## 1.1 Electroluminescence

The working principle of organic light emitting diodes (OLEDs) is based on the phenomenon of electroluminescence (EL), that is the generation of light by the application of an electrical field to the sample under investigation.<sup>14-16</sup> Fundamental research in this field goes back to the first half of the 20<sup>th</sup> century. For the first time, electroluminescence was reported by Destriau when he investigated a powder sample of zinc sulfide which however was spoiled – nowadays this would be called doped – with copper.<sup>17</sup> For organic compounds the observation of EL has been described by Bernanose et al. for the first time in 1953.<sup>18,19</sup> In contrast to these two experiments, in which an alternating current voltage was required for the observation of EL, Pope et al. described luminescence from an anthracene single-crystal under application of a direct current voltage of several hundred Volts in 1963.<sup>20</sup> However, the experiments of Destriau, Bernanose, and Pope required high driving voltages which limited EL to a laboratory environment. As a consequence, EL was of very limited relevance for technological applications. In the following years the driving voltages could be significantly reduced to well below 100 V. This was achieved by shrinking the thickness of the devices to only a couple of 100 nm through the use of vacuum deposition in the production process. But also these devices did not become technologically relevant due to extremely short device lifetimes of only a couple of minutes which was mainly owed to the still relatively large voltages needed for operation.<sup>21</sup> A major breakthrough could be achieved by Tang and van Slyke in 1987 by reducing the voltage necessary for operation to less than 10 V.<sup>22</sup> This was possible by using a layered device structure in their experiments. More specifically, they applied

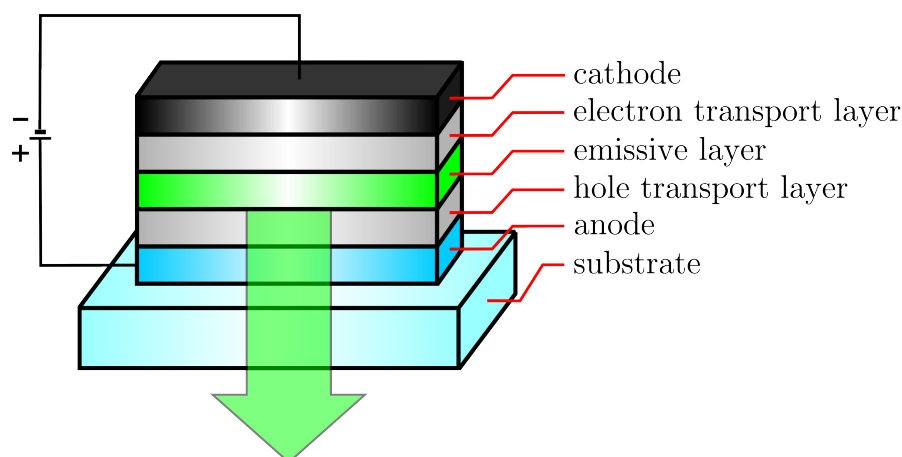


Figure 1.1: Schematic representation of a three-layer OLED stack.

two different materials for the transport of electrons and holes from the cathode and anode, respectively, through the device to the recombination zone. On the one hand, this allowed an efficient injection and transport of the charge carriers without significant ohmic losses. On the other hand, in this way the recombination zone of electrons and holes could be limited to a narrow area on the interface of the two transport layers. This approach resulted in an at this time highly efficient device with an external emission quantum yield of about 1%. In fact, this device structure laid the foundation for further developments and represented the starting point for extensive research in the field of organic light emitting diodes.

## 1.2 Device Structure and Principle of Operation

In general, an OLED can be even simpler than the two layer device suggested by Tang and van Slyke as in principle it is sufficient to sandwich one organic emissive layer between the anode and the cathode. In contrast to multilayer stacks though, such an approach suffers from inferior device performance, especially, regarding the device efficiency and lifetime.<sup>2,7,23,24</sup> As the most simple device design that is of practical relevance a three layer stack can be considered. Figure 1.1 shows the structure of a such a device. In the following, the purpose of the individual components will be explained briefly.

The core component of every OLED is the emissive layer where the light emitting molecules are located. In the case of a small molecule OLED it consists of a hole *and* electron conducting matrix material into which the desired emitter is doped. Emitter ma-



materials that exhibit phosphorescence or thermally activated delayed fluorescence (TADF) are preferred as they can exhibit a four times larger electroluminescence emission quantum yield and therefore a four times larger device efficiency compared to conventional purely fluorescent emitters (compare section 1.3).<sup>1,2,6-8,23,24</sup> At the moment, iridium(III)- and platinum(II)-complexes represent the most efficient class of phosphorescent emitters<sup>25-27</sup> whereas copper(I)-complexes are entering the field of TADF emitters.<sup>13,28-43</sup> Independently, recently also the potential of purely organic compounds that exhibit a TADF was recognized for the use in OLEDs.<sup>5,44-48</sup> An interesting aspect is the emitter concentration in the emissive layer. Usually, large emitter concentrations are desired to realize OLEDs with high brightness. However, for iridium complexes and most other emitters it has been shown that an increase of the emitter concentration results in a decrease of the emission quantum yield due to intermolecular interactions such as triplet-triplet annihilation.<sup>49-51</sup> Therefore, the doping concentration of the emissive layer is typically limited to the range between 5% and 15%. In contrast to this, copper compounds frequently do not exhibit such a self-quenching effect<sup>6,13,33,35,36</sup> and could therefore be applied in much higher doping concentrations even up to 100%.<sup>13,52,53</sup>

The emissive layer is sandwiched between two layers which are intended to increase the mobility of the charge carriers and are therefore called electron transport layer (ETL) and hole transport layer (HTL), respectively. Interestingly, the thickness of these layers does not have a significant impact on the electrical properties of the device but the optical properties can be improved by choosing an appropriate thickness for these layers. For example, an increase of the ETL thickness increases the distance between emissive layer and cathode. As a consequence, a possible loss channel, the coupling of the radiating dipole of the emitter with the metal cathode, can be minimized.<sup>7,54-57</sup> Another important aspect is that by appropriately doping the transport layers, the ratio of injected holes to injected electrons can be adjusted and ideally be brought close to one. This prevents an excess of carriers of one type and therefore enhances the device efficiency.<sup>7,10,58</sup>

An electrical contact for the three layer stack described above, is provided by two electrodes. For the anode preferentially indium tin oxide (ITO) is used due to its high electrical conductivity and optical transparency.<sup>59</sup> For the cathode, metals with a low work function are suited, e. g. aluminum or magnesium.<sup>59</sup> As all layers together with the two electrodes are significantly thinner than 1  $\mu\text{m}$  a substrate is needed for mechanical stability. For this purpose glass is often used. If flexibility of the entire stack is desired polymer foils are an alternative.<sup>60</sup>

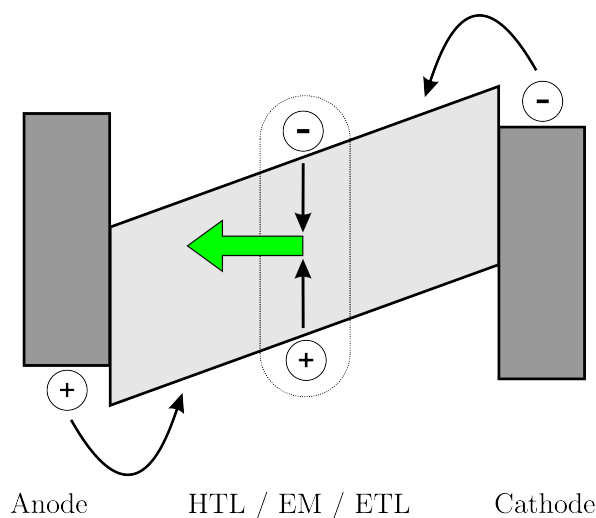


Figure 1.2: Principle of operation of an OLED.

The fundamental processes that lead to light emission from an OLED are displayed in Figure 1.2.<sup>2,7,23,24</sup> With the application of an external voltage to the two electrodes, negatively charged electrons are injected from the cathode into the LUMO (lowest unoccupied molecular orbital) of an electron transport layer molecule. Similarly, positively charged holes are injected into the HOMO (highest occupied molecular orbital) of a hole transport layer molecule. As the external voltage results in a strong electric field across the layer stack, both charge carrier types, electrons and holes, start to migrate towards the emissive layer. In contrast to charge transport mechanisms in inorganic semiconductors or metals where the carriers can move almost freely through the respective material, in the case of organic materials the transport occurs via thermally activated hopping processes between adjacent molecules. Formally, this corresponds to a series of redox reactions. Eventually, one of the two particles is trapped on a matrix or an emitter molecule. If an oppositely charged carrier comes close enough, electrostatic attraction between both particles becomes relevant and this leads to the formation of a bound state called exciton. Furthermore, the attraction between both particles results in the localization of electron and hole on the same molecule which can then be considered being in an excited state. Ideally, this should occur on an emitter molecule, so that a photon can be emitted when the molecule relaxes radiatively to the ground state. Typically, the generated light then leaves the OLED towards the direction of the (transparent) anode.

As the energy efficiency of an OLED strongly depends on the design of the layer stack,

it is helpful to define a quantity for the evaluation of the light generation efficiency. A key parameter that is suitable for this purpose is the emission quantum yield  $\eta$ .<sup>7,61,62</sup> It is furthermore reasonable, to distinguish between the internal  $\eta_{int}$  and the external emission quantum yield  $\eta_{ext}$ . Hereby,  $\eta_{int}$  corresponds to the probability with which a photon is generated by an exciton in the emissive layer whereas  $\eta_{ext}$  also respects the outcoupling probability of the generated photon from the device to the outside world. At first, the discussion will be focused on the internal emission quantum yield.

$$\eta_{int} = \beta \cdot \Phi_{PL} \cdot \gamma \quad (1.1)$$

As can be seen from this equation, three factors contribute to  $\eta_{int}$ . In the following, each factor will be discussed briefly. The spin-statistics factor is represented by  $\beta$ . This factor is determined by the emitter material class used. Conventional fluorescent emitters possess a value of  $\beta = 0.25$  whereas phosphorescent emitters and emitters that exhibit a thermally activated delayed fluorescence have a four times larger value of  $\beta = 1$ .<sup>6,8,9,23</sup> A more detailed discussion of the spin-statistics factor is given in section 1.3.

The second contribution to the internal quantum efficiency is given by the photoluminescence quantum yield  $\Phi_{PL}$  of the emitter material used. This quantity describes the probability with which the absorption of a photon results in the emission of another photon and is therefore given by the ratio of photons emitted to photons absorbed. In an equivalent formulation  $\Phi_{PL}$  can be expressed as the ratio of the radiative rate and the sum of radiative and nonradiative rate.<sup>63</sup> Currently, for the application in OLEDs emitters based on phosphorescent iridium complexes are of particular interest. These materials can reach high photoluminescence quantum yields of close to 100%.<sup>5,6,49,50,64–67</sup> However, such high emission quantum yields are in general only found for iridium complexes exhibiting green emission. Due to the presence of emission quenching ligand field (dd\*) states, it still remains a challenge to develop highly desired efficient blue emitting Ir(III) compounds.<sup>5</sup> In contrast to this, Cu(I) complexes possess a closed d-shell and therefore no excited ligand field states are present. This renders Cu(I) compounds a promising emitter class for OLEDs especially for the blue range of the spectrum. Recently, several examples for such blue emitting Cu(I) compounds with photoluminescence quantum yields as high as 90% have been reported.<sup>13,33,36,37,39,68</sup> Also, the complexes presented in chapter 3 and 4 are promising as they exhibit quantum yields of up to 76%.

The last term in equation 1.1 represents the charge-balance factor  $\gamma$  which describes the ratio of injected electrons and holes to excitons formed.<sup>61</sup> A charge balance factor smaller than 1 indicates that there is an excess of charge carriers of one kind accumulating in the device which then cannot contribute to the generation of light. However, by careful device design  $\gamma$  factors of close to 1 can be reached and have already been demonstrated.<sup>10</sup> It is noted that in contrast to the spin-statistics factor  $\beta$  and to the photoluminescence quantum yield  $\Phi_{PL}$ , the charge balance factor  $\gamma$  is in a first approximation independent of the emitter material used but does strongly depend on the design of the OLED layer stack.

Compared to the internal quantum efficiency  $\eta_{int}$  the external emission quantum yield  $\eta_{ext}$  also takes the outcoupling efficiency  $\chi_{out}$  of the generated photons into account.<sup>7,24,55</sup>

$$\eta_{ext} = \eta_{int} \cdot \chi_{out} \quad (1.2)$$

Whereas in modern devices internal quantum efficiencies of close to 1 can be reached and have already been demonstrated more than one decade ago,<sup>10</sup> typical outcoupling efficiencies amount only to about 0.2. Two main loss channels could be identified to be responsible for this. (1) The organic layers and the substrate typically exhibit indices of refraction larger than about  $n = 1.5$ . As a result, total reflection on the layer interfaces and especially, on the substrate/air interface occurs. This leads to trapping of the generated photons in the device. An approach to minimize this loss channel is structuring the surface of the devices e. g. with arrays of micro lenses or spheres.<sup>24,69,70</sup> (2) As the emitting molecule can be considered a radiating dipole, coupling of this dipole to the metal cathode is possible. As a consequence, electron oscillations (surface plasmons) can be excited in the metal. A reduction of this loss channel can be achieved by placing the dipole more far away from the metal cathode for example by increasing the thickness of the electron transport layer. Another approach is to align the emitter molecules in a way that the the coupling to the metal cathode is minimized.<sup>7,24,55-57</sup>

### 1.3 Triplet Harvesting and Singlet Harvesting

In the previous section, it has already been mentioned that with emitters exhibiting a phosphorescence or a thermally activated delayed fluorescence a four times higher

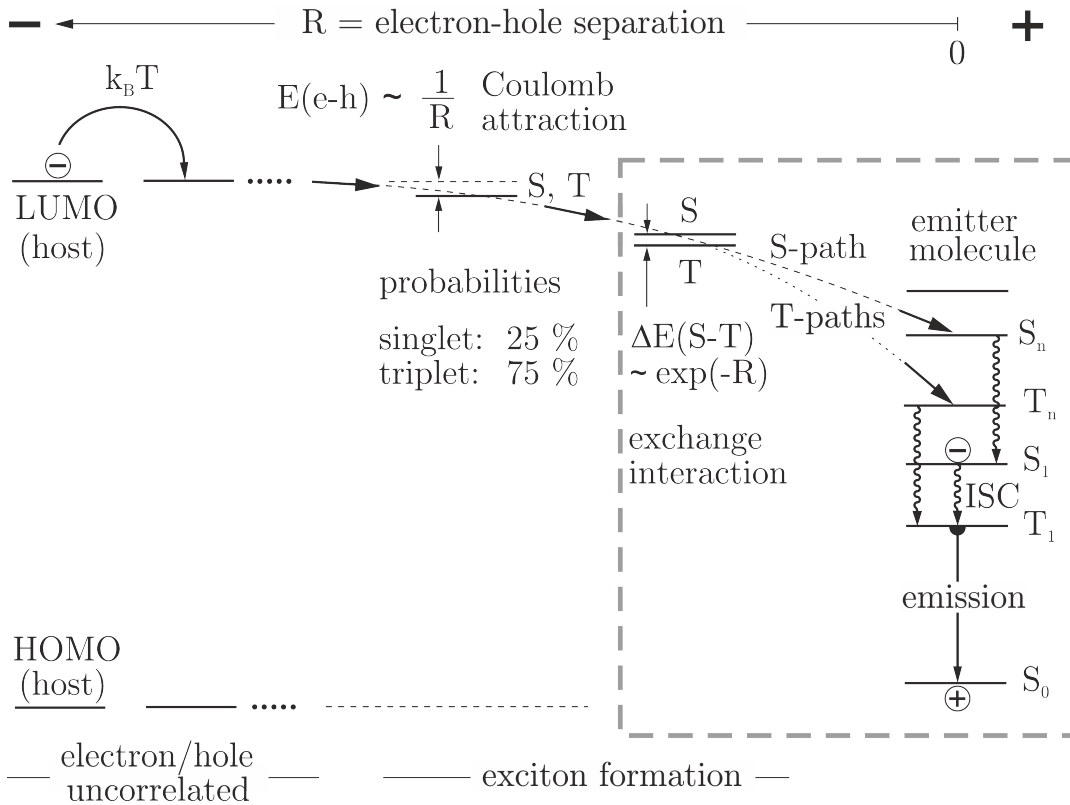


Figure 1.3: Simplified scheme of the exciton formation and recombination process in a host/guest system.  $E(e-h)$ : binding energy of electron and hole,  $R$ : spatial separation of electron and hole,  $\Delta E(S_1 - T_1)$ : energy separation of singlet (S) and triplet state (T), ISC: intersystem crossing. Adapted from references 23, 72.

emission quantum yield can be achieved in electroluminescent devices compared to purely fluorescent materials.<sup>5,8,13,23,40</sup> In order to understand this different behavior, the mechanisms that lead to exciton formation in the emissive layer and as a result to the population of the excited states of the emitter molecules have to be analyzed. The following discussion of this is based on the one given in references 5, 23, 71, 72.

A simplified scheme of the exciton formation process is displayed in Figure 1.3. For the following considerations it is assumed that the EML consists of a host material in which the emitter is doped at a low concentration. Furthermore, it is assumed that an electron and a hole have already been injected into the EML and that the hole is already localized at the emitter molecule.

Driven by the external electrical potential the electron now starts to migrate towards

the hole through thermally activated hopping processes. Both particles can be considered as uncorrelated as long as they are far apart from each other. As the electron approaches the hole, Coulomb interaction between the oppositely charged particles becomes effective. As a consequence of this electrostatic attraction, the distance between electron and hole decreases further. When the separation  $R$  between electron and hole falls below a critical value  $R_c$  both particles can be considered to form a bound state – an exciton. This is the case when the Coulomb energy  $E(e - h)$  becomes larger than the thermal energy  $E_{th}$ .

$$E(e - h) = \frac{e^2}{4\pi\epsilon\epsilon_0 R} \stackrel{!}{=} k_B T = E_{th} \quad (1.3)$$

In this equation,  $e$  represents the elementary charge,  $\epsilon_0$  and  $\epsilon$  the permittivity of the vacuum and the matrix material, respectively,  $k_B$  the Boltzmann constant, and  $T$  the temperature.

According to this equation, if a value of  $\epsilon = 3$  is assumed, at ambient temperature an exciton is already formed at a relatively large distance of electron and hole of about  $R_c = 180 \text{ \AA}$ . This means that electron and hole do not have to be located on one molecule in order to form a bound state but that they can still be separated by a large number of matrix molecules.

As soon as electron and hole are considered to be correlated also the spin of both particles has to be taken into account. As both particles carry a spin of  $1/2$  the total spin of the formed exciton can either amount to  $S = 0$ , corresponding to a singlet state with multiplicity  $M = 1$ , or to  $S = 1$ , corresponding to a triplet state with multiplicity  $M = 3$ . Consequently, electron and hole can form four different exciton states, one of them being a singlet and three of them representing the triplet. As at this point all states are nearly degenerate an even population of all four states is expected. In a statistical limit this leads to a ratio of singlet to triplet excitons of 1 : 3.<sup>73</sup>

When the electron approaches the hole within a radius of about  $15 \text{ \AA}$  the wave functions of both particles may be regarded to start to overlap. At this point, the exchange interaction between the two particles cannot be neglected anymore. As a result, the formerly degenerate singlet and triplet states are now energetically split by twice the exchange integral.

Eventually, the attraction of electron and hole will lead to a localization of both particles on the same emitter molecule. This situation corresponds to this molecule being

in an excited state. Subsequently, the emitter molecule relaxes to the lowest excited singlet or triplet state depending on the total spin of the respective exciton. Typically, this occurs on a picosecond time scale or faster.

It is emphasized that from exciton formation to the population of the excited emitter states the spin is conserved meaning that singlet excitons can only populate singlet and triplet excitons only triplet states of the emitter molecule. As a consequence, 75 % of the emitter molecules will be in their lowest excited triplet while only 25 % will be in their lowest excited singlet state.

Starting from this situation (Figure 1.4b), the further relaxation processes depend on the class of the emitter material used. A graphical representation of possible relaxation paths is displayed in Figure 1.4 for three different emitter types.

In conventional purely organic molecules (Figure 1.4a) the population of the first excited singlet state  $S_1$  can result in an efficient radiative deactivation to the ground state via a fluorescence which typically occurs at a time scale in the order of several ns and with quantum yields of up to 100 %.<sup>63</sup> Also an intersystem crossing process (ISC) from the  $S_1$  to the  $T_1$  state can occur. However, due to the absence of effective spin-orbit coupling (SOC) in purely organic molecules the time scale for this process is significantly longer (up to several milliseconds) than the fluorescence decay time.<sup>63</sup> Therefore, the contribution of ISC to the deactivation of the  $S_1$  state can be neglected. In contrast to the highly allowed  $S_1 \rightarrow S_0$  transition, the  $T_1 \rightarrow S_0$  transition is strongly spin-forbidden. This results in phosphorescence decay times which can be as long as several seconds. As such long decay times favor the occurrence of nonradiative deactivation processes the probability for a radiative transition is rather small. Accordingly, in purely organic molecules only the singlet excitons (25 %) can be used for the generation of light in an electroluminescent device, while all triplet excitons (75 %) are lost for this purpose. This fact limits the internal quantum yield of OLEDs using fluorescent emitters to  $\eta_{int} = 0.25$ .

The situation is different when transition-metal compounds are looked at (Figure 1.4c). In this case, the central metal atom induces significant SOC. As a consequence, the time constant for the ISC process is drastically decreased to values in the pico- or even femtosecond region.<sup>74-79</sup> Under the condition that singlet and triplet state are separated by several  $10^3 \text{ cm}^{-1}$ , an emission from the singlet state cannot be observed anymore as almost all singlet excitations are transferred to the triplet state before a fluorescence can occur. Furthermore, SOC adds significant allowedness to the otherwise spin-forbidden transition from the triplet to the ground state. For compounds with particularly effective

SOC, emission decay times can be as short as 1 or 2  $\mu\text{s}$ , while emission quantum yields approaching 100 % can be achieved.<sup>5,26,27,56,64,65,80</sup> Thus, in contrast to purely organic emitters, the triplet excitations are not lost for the emission process. As a consequence, OLEDs utilizing phosphorescent emitters can reach an internal emission quantum yield of  $\eta_{int} = 1$ . As according to this mechanism all excitations are collected in the triplet state, this is called the *triplet harvesting effect*.

On the other hand, in many other, especially 1<sup>st</sup> row, transition metal compounds SOC is significantly less effective which results in relatively long triplet decay times of up to several milliseconds.<sup>5,32,33,35,36,81</sup> Emitters exhibiting such long decay times are rather ineffective when applied in OLEDs as pronounced saturation effects, such as triplet-triplet annihilation or efficiency roll-off, would occur.<sup>51</sup> These problems can be overcome if the long triplet emission decay time does not become effective, for example, if emitters are used that exhibit only a small energy separation  $\Delta E(S_1 - T_1)$  between first excited singlet and triplet state, so that a thermal re-population of the singlet from the triplet state reservoir is possible at ambient temperature (Figure 1.4d). Such a mechanism corresponds to a thermally activated delayed fluorescence and leads to an effective reduction of the overall emission decay time as a significant part of all excitations is radiatively deactivated via the short lived singlet state.<sup>82</sup> Moreover, in OLEDs utilizing TADF emitters all injected excitons, singlets and triplets, can be converted to light. Consequently, the internal emission quantum yield of such devices can also amount to  $\eta_{int} = 1$ . In analogy to the triplet harvesting effect, this mechanism is termed *singlet harvesting effect* as at ambient temperature the radiative deactivation is occurring almost exclusively via the singlet state.<sup>5,13,33,35-37</sup>



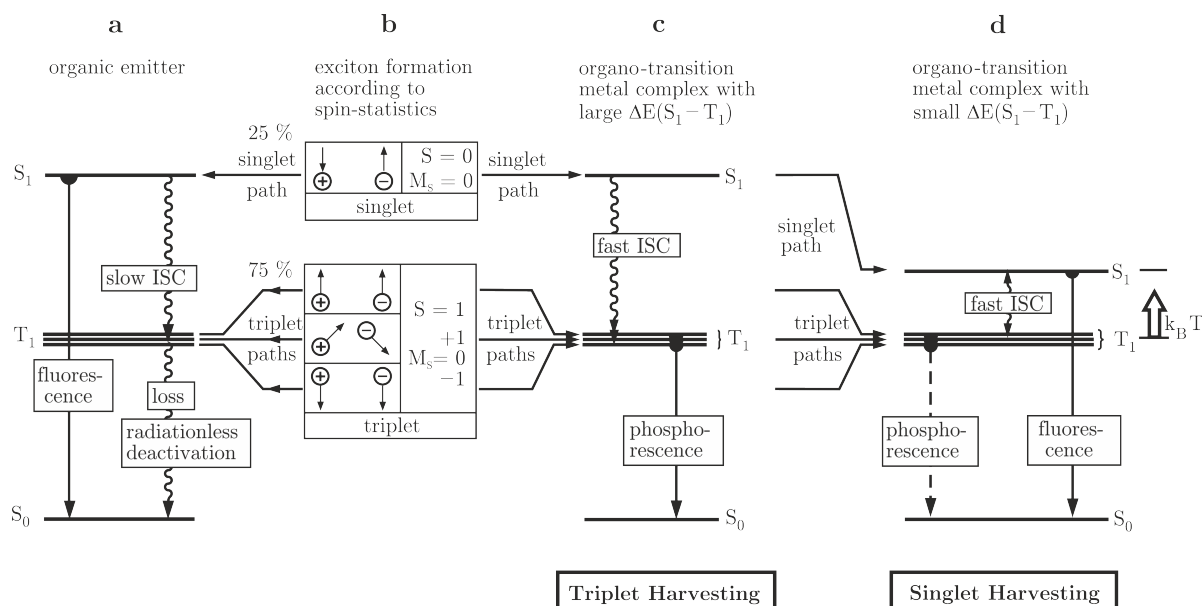


Figure 1.4: Schematic representation of the electroluminescence excitation process for different emitter classes. (b) Spin statistics results in 25 % singlet and 75 % triplet state population. (a) In conventional purely fluorescent emitters, only emission from the singlet state occurs. All triplet excitations are lost for the emission of light. (c) In transition metal complexes all singlet excitations are transferred to the triplet state via fast intersystem crossing (ISC). From the triplet state, an efficient radiative deactivation through a  $T_1 \rightarrow S_0$  phosphorescence is possible. As a result, all excitations, singlets and triplets can be harvested in the triplet state and utilized for the generation of light (triplet harvesting effect). (d) In compounds that exhibit a small energy separation  $\Delta E(S_1 - T_1)$  between the first excited singlet and triplet state, a thermally activated delayed fluorescence (TADF) can occur. In this case, also all excitons can be converted to light but the emission results from the highly allowed  $S_1 \rightarrow S_0$  transition (singlet harvesting effect). Adapted from reference 5.



## Photophysical Properties of Transition Metal Complexes

In the last chapter, it has already been pointed out that transition metal compounds possess high potential for application as emitters in electroluminescent devices. In this chapter, aspects of the electronic structure and emission properties of such complexes will be discussed. As this thesis focuses on the photophysical investigation of Cu(I) compounds, the following discussion will be centered around this material class. Where it seems necessary, also comparisons to the well investigated class of platinum and iridium compounds will be drawn.

### 2.1 Electronic States

As for all transition metal complexes, also for Cu(I) compounds the emission properties are largely determined by their frontier orbitals, that are the highest occupied and lowest unoccupied molecular orbitals (MOs). From these MOs, the lowest excited electronic states result. In a rather simple approximation, the frontier orbitals can be described by the occupied  $\pi$  and unoccupied  $\pi^*$  orbitals of the ligand(s) and the occupied d and unoccupied  $d^*$  orbitals of the central metal ion. In such a model system, four different one electron excitations can occur. An illustration of this is given in Figure 2.1. It is noted that all considerations presented here are only valid for molecules exhibiting a singlet ground state.

The excitation of an electron from a  $\pi$  to a  $\pi^*$  orbital corresponds to a ligand centered (LC) transition. Hereby,  $\pi$  and  $\pi^*$  orbitals are usually located on the same ligand.

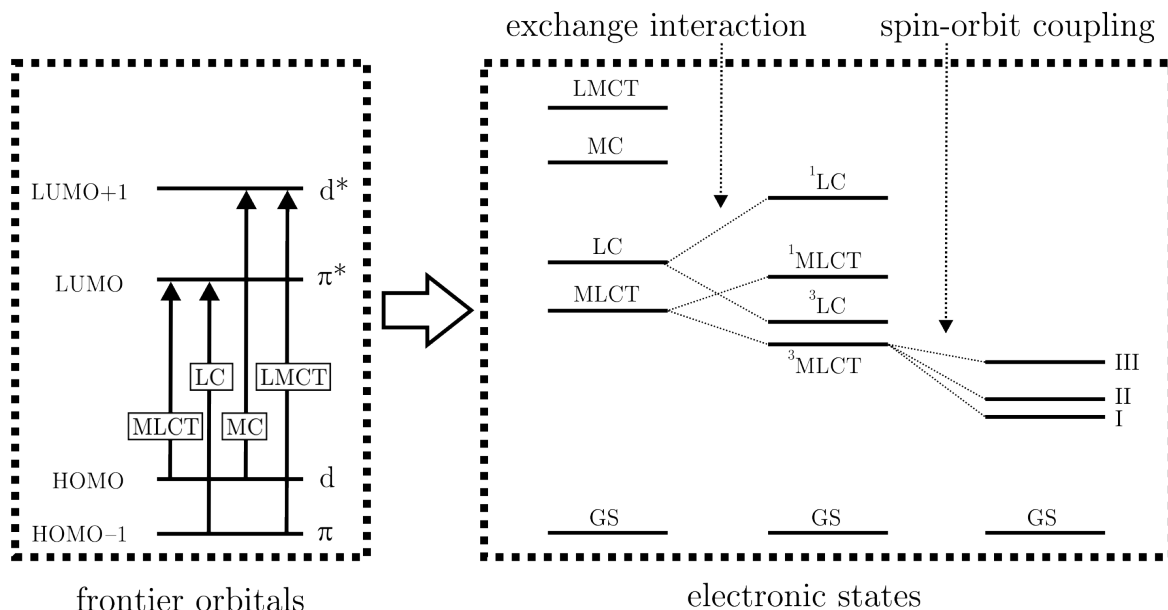


Figure 2.1: Frontier orbitals and the resulting excited states of a transition metal complex. Only one electron excitations are displayed. Inclusion of the exchange interaction results in an energetic splitting of otherwise degenerate singlet and triplet states. If further spin-orbit coupling is included an energy splitting of the three triplet substates occurs. Adapted from reference 83.

However, in heteroleptic complexes, an electron can also be transferred from a  $\pi$  orbital of one ligand to the  $\pi^*$  orbital of another ligand. In this case, the process is termed ligand-to-ligand charge transfer (LLCT). In the literature, many examples for platinum compounds exhibiting ligand centered transitions have been reported. For copper compounds, this transition type is less relevant but also here some examples exist.<sup>78,84</sup>

Metal centered (MC) transitions occur if an electron is excited from a  $d$  orbital of the central metal atom to another unoccupied metal orbital. Typically, the unoccupied orbital is of  $d^*$  type. In this case, the resulting  $dd^*$  state can also be termed as ligand field (LF) state. In iridium and platinum compounds, these LF states generally are not the lowest lying excited states but they can be energetically close enough so that a thermal population from the emissive state can occur even at ambient temperature. As LF states are frequently not emissive they represent a major source for nonradiative deactivation and even molecular dissociation, especially for blue emitting compounds in which emissive and LF state can be as close as only a few thousand wavenumbers. In contrast to this, LF states do not have an influence on the emission behavior of Cu(I)

compounds, as the d-shell of Cu(I) possesses a  $d^{10}$  configuration and is therefore fully occupied, so that no empty accessible  $d^*$  orbitals and therefore no LF states exist. For this reason, Cu(I) compounds might be well suited for the development of stable blue emitters with high emission quantum yields. Moreover, in Cu(I) clusters, also metal centered  $ds^*$  excitations can occur. In contrast to LF states these states can be highly emissive and contribute to the emission (compare for example reference 85).

Metal-to-ligand charge transfer (MLCT) transitions occur if on excitation significant charge is transferred from the central metal ion to one of the ligands. This transition type largely determines the emission behavior of most OLED relevant iridium and platinum complexes. In particular, through the involvement of the metal center in the emitting states, strong spin-orbit coupling can be induced which can result in high emission yields and short emission decay times. In contrast to this, for Cu(I) complexes SOC is significantly less effective (presumably) due to the smaller SOC constant of copper. This would lead to distinctly longer emission decay times and smaller emission quantum yields. However, the charge transfer character is generally much more pronounced for copper compared to platinum and iridium complexes. As a consequence, a thermally activated delayed fluorescence can occur for Cu(I) compounds.

It is crucial to note that in this simple molecular orbital picture an important aspect, the interaction of the two unpaired electrons with each other, via Coulomb and exchange interaction, is neglected. An inclusion of these effects results in a splitting of each state, except for the ground state, into two states with different spin configuration, in the case of a singlet ground state into a singlet and a triplet excited state. These two states are energetically split by approximately twice the exchange integral  $K$ . The following example displays a situation frequently found in Cu(I) compounds. Typically, in such complexes the lowest excited singlet and triplet state is of MLCT character where the HOMO is mainly located on the d-orbitals of the metal center whereas the LUMO is mainly located on the ligand's  $\pi^*$  orbital. In this situation, the energy splitting between the first excited singlet and triplet state  $\Delta E(S_1 - T_1)$  is given by:

$$\Delta E(S_1 - T_1) \approx 2K = 2 \left\langle d(r_1)\pi^*(r_2) \left| \frac{e^2}{4\pi\epsilon_0 r_{12}} \right| d(r_2)\pi^*(r_1) \right\rangle \quad (2.1)$$

Hereby,  $d$  and  $\pi^*$  represent the wavefunctions of the HOMO and LUMO, respectively,  $r_1$  and  $r_2$  the electron coordinates, and  $r_{12}$  their spatial separation. From this equation it is

apparent that the exchange integral depends on the (spatial) overlap of the wavefunctions of the molecular orbitals involved in the transition. For a  $d\pi^*$  charge transfer transition, this overlap can be rather small as  $d$  and  $\pi^*$  orbitals are located at different parts of the molecule. In this situation, a small exchange integral and therefore a small splitting between first excited singlet and triplet state result. The situation is different for localized transitions, for example for ligand centered transitions of  $\pi\pi^*$  character. In this case, a strong spatial overlap of the electron wavefunctions occurs as HOMO and LUMO are located at the same ligand. Consequently, the exchange integral and the splitting between first excited singlet and triplet state are large. More general, it can be stated that the singlet-triplet energy splitting decreases with increasing charge transfer character of the transition. It is remarked that the considerations made above only represent an approximation to the real situation found in transition metal complexes, where molecular orbitals typically consist of mixtures between ligand and metal centered orbitals. Accordingly, also the states represent mixtures.

## 2.2 Spin-Orbit Coupling

The central metal ion has a further strong impact on the properties of the electronic states of transition metal complexes. In particular, the metal center induces significant spin-orbit coupling (SOC) which results in fast intersystem crossing (ISC) between singlet and triplet states. For Pt(II) compounds, ISC times as fast as 50 fs have been observed.<sup>23,76</sup> In contrast to this, for Cu(I) compounds significantly longer ISC time constants of about 10 ps have been reported.<sup>79,86,87</sup> However, this is still orders of magnitude faster than time constants for prompt fluorescence which typically range between 1 ns and 100 ns. As a consequence, prompt fluorescence can in general not be observed in transition metal complexes.

Furthermore, SOC allows an efficient coupling of different states. Of particular interest in this regard is the coupling of singlet states to the lowest excited triplet state. Through this, significant singlet character can be mixed into this triplet state which adds allowedness to the otherwise spin-forbidden  $T_1 \rightarrow S_0$  transition. Consequently, short phosphorescence decay times and high emission quantum yields for this transition result. Efficient coupling between two electronic states according to the direct SOC process can hereby only occur if the following three conditions are fulfilled:

1. The interacting states must not result from the same molecular orbitals.
2. The two interacting states must result from two molecular orbitals that share the same metal center. Ideally, this metal center should exhibit a large SOC constant.
3. The interacting states must result from different metal d-orbitals.

From this it can be concluded that direct SOC is mainly effective for states resulting from molecular orbitals that have significant contributions from metal d-orbitals. Therefore, coupling between MLCT states is most efficient whereas LC states can neither couple to a MLCT nor to another LC state. For an evaluation of the SOC efficiency in real molecular systems the radiative  $T_1 \rightarrow S_0$  transition rate  $k_r$  can be used. Hereby, it is important to note, that the three triplet substates, in the following marked with the index  $i$ , experience different admixtures from higher lying singlet states and therefore exhibit different radiative rates. A quantitative expression for  $k_r(i)$  can be given by the following equation which is obtained from perturbation theoretical considerations:<sup>88</sup>

$$k_r(i) = \frac{64\pi^4\bar{\nu}^3}{3hc^3} \sum_m \left| \frac{\langle S_m | \mathbf{H}_{\text{SO}} | T_1(i) \rangle}{E(S_m) - E(T_1)} \right|^2 |\langle S_0 | e\mathbf{r} | S_m \rangle|^2 \quad (2.2)$$

In this equation,  $\bar{\nu}$  represents the transition energy in wavenumbers,  $\mathbf{H}_{\text{SO}}$  the Hamilton operator for SOC, S and T the unperturbed wavefunctions of the coupling singlet and triplet states with the energies  $E(S)$  and  $E(T)$ , respectively, and  $e\mathbf{r}$  the dipole operator.

Furthermore, SOC also leads to an alteration of the energies of the coupling states. For the three substates of the lowest excited triplet state  $T_1$ , an energy stabilization occurs. As each substate experiences different amounts of admixtures from higher lying singlet and triplet states, a different energy stabilization for each individual triplet substate results. Similarly as described above, also an expression for the energy splitting of the three triplet substates can be obtained from the perturbation theory formalism:<sup>88</sup>

$$E(i) = E(T_1) - \sum_{n,j} \frac{|\langle T_n(j) | \mathbf{H}_{\text{SO}} | T_1(i) \rangle|^2}{E(T_n) - E(T_1)} - \sum_m \frac{|\langle S_m | \mathbf{H}_{\text{SO}} | T_1(i) \rangle|^2}{E(S_m) - E(T_1)} \quad (2.3)$$

This splitting is also observed in the absence of a magnetic field. Therefore, the energy separation of the energetically lowest and highest lying triplet substate is termed zero

field splitting (ZFS).

For completeness it is mentioned that also the process of indirect SOC exists. However, this process is significantly less effective compared to the direct one. A more detailed discussion of this and other aspects of SOC can be found in reference 88.

## 2.3 Temperature Dependence of Emission

In transition metal complexes emission is not occurring from a single electronic state. For example, if other states are energetically close, they can be thermally populated and contribute to the emission. Hereby, each state exhibits an individual deactivation rate  $k_i$  to the ground state. Under the assumption, that all states are in a fast thermal equilibrium, the states are populated according to a Boltzmann distribution and the total deactivation rate  $k(T)$  of all states to the ground state in dependence of the temperature  $T$  is given by:<sup>1,28,89</sup>

$$k(T) = \frac{\sum_{i=1}^p k_i \exp\left[-\frac{\Delta E(i-i_0)}{k_B T}\right]}{\sum_{i=1}^p \exp\left[-\frac{\Delta E(i-i_0)}{k_B T}\right]} \quad (2.4)$$

In this equation,  $k_B$  represents the Boltzmann constant and  $\Delta E(i - i_0)$  the energy separation between  $i$ -th state and the energetically lowest excited state  $i_0$ . However, emission decay times  $\tau$  are experimentally better accessible than rates  $k$ . Therefore, it is helpful to rephrase equation 2.4 accordingly, using  $\tau = k^{-1}$ . For a four level system consisting of the lowest excited singlet ( $S_1$ ) and triplet ( $T_1$ ) state, whereby the triplet consists of the three substates  $I$ ,  $II$ , and  $III$ , the emission decay time can be written as a function of temperature according to the following equation:<sup>39,65,89</sup>

$$\tau(T) = \frac{1 + \exp\left[-\frac{\Delta E(II-I)}{k_B T}\right] + \exp\left[-\frac{\Delta E(III-I)}{k_B T}\right] + \exp\left[-\frac{\Delta E(S_1-I)}{k_B T}\right]}{\tau_I^{-1} + \tau_{II}^{-1} \exp\left[-\frac{\Delta E(II-I)}{k_B T}\right] + \tau_{III}^{-1} \exp\left[-\frac{\Delta E(III-I)}{k_B T}\right] + \tau_{S_1}^{-1} \exp\left[-\frac{\Delta E(S_1-I)}{k_B T}\right]} \quad (2.5)$$

For molecular systems, in which no TADF occurs and in which therefore the en-



energetic separation between first excited singlet and triplet state  $\Delta E(S_1 - I)$  is large ( $> 3000 \text{ cm}^{-1}$ ), the last term in the nominator and denominator in equation (2.5) is small and can be neglected. This leads to:<sup>1,65</sup>

$$\tau(T) = \frac{1 + \exp\left[-\frac{\Delta E(II-I)}{k_B T}\right] + \exp\left[-\frac{\Delta E(III-I)}{k_B T}\right]}{\tau_I^{-1} + \tau_{II}^{-1} \exp\left[-\frac{\Delta E(II-I)}{k_B T}\right] + \tau_{III}^{-1} \exp\left[-\frac{\Delta E(III-I)}{k_B T}\right]} \quad (2.6)$$

A situation frequently found for Cu(I) complexes is that the zero field splitting (ZFS =  $\Delta E(III - I)$ ) is small ( $< 1$  to  $2 \text{ cm}^{-1}$ ). In this case, it is justified to assume  $\Delta E(II - I) = \Delta E(III - I) = 0$ . Then, equation (2.5) simplifies to:

$$\tau(T) = \frac{3 + \exp\left[-\frac{\Delta E(S_1-I)}{k_B T}\right]}{3\tau_{T_1}^{-1} + \tau_{S_1}^{-1} \exp\left[-\frac{\Delta E(S_1-I)}{k_B T}\right]} \quad (2.7)$$

Note that  $\Delta E(S_1 - I)$  often is also termed as  $\Delta E(S_1 - T_1)$ .

Importantly, by fitting equations (2.5) – (2.7) to experimental data, more specifically to the temperature dependent behavior of the emission decay time, the energy splitting of the emitting states as well as their individual decay constants can be determined for the investigated compounds. As in contrast to Pt(II) and Ir(III) generally for Cu(I) complexes no highly resolved spectra can be obtained even at a temperature of  $T = 1.3 \text{ K}$  (compare chapters 3 and 4) this indirect method provides detailed access to properties of the electronic states.



## Dinuclear Copper Complexes

In the last decades, Cu(I) complexes have been intensely studied due to their interesting luminescence properties. Research in this field has been additionally stimulated, since the potential of these compounds as emitters in organic light-emitting diodes was recognized. Hereby, most investigations focused on Cu(I) complexes exhibiting one copper center that is pseudo-tetrahedrally coordinated by two bidentate ligands.<sup>5,6,28,33,35,38,42,78,79,84,86,87,90–99</sup>

In contrast to this, dinuclear Cu(I) compounds are significantly less explored, especially with regard to their emission behavior. Only recently, respective investigations have been published, suggesting that also this material class can show very promising properties at ambient temperature, such as short emission decay times, high emission quantum yields, and the possibility to tune the emission energy over a wide spectral range, from the deep blue to the dark red.<sup>13,30,32,37,100–106</sup> In addition, for some of these complexes it was demonstrated that they exhibit a thermally activated delayed fluorescence,<sup>30,32,102,106</sup> making them highly attractive for the use in OLEDs. Interestingly, the activation energy for the TADF process can be as low as only  $350\text{ cm}^{-1}$  for the dimers,<sup>30,102</sup> significantly smaller than for monomeric Cu(I) complexes for which the activations energies are typically about two to three times larger.<sup>5,6,28,33,35,39,42</sup>

Therefore, in this chapter a new class of Cu(I) dimers is studied in detail to get a deeper insight into the emission processes. The complexes represent dinuclear compounds in which one bidentate ligand is coordinated to each copper center and where the copper centers themselves are bridged by two halides. In the first section of this chapter, the investigation focuses on the influence of the halides on the emission behavior. In the second section, the ligands and the metal ions are modified to study the respective effects on the emission properties.

### 3.1 Complexes with Aminophosphine Ligands

In this section, the four halide bridged copper complexes  $[\text{Cu}(\mu\text{-Cl})(\text{PNMe}_2)]_2$  (**1**),  $[\text{Cu}(\mu\text{-Br})(\text{PNMe}_2)]_2$  (**2**),  $[\text{Cu}(\mu\text{-I})(\text{PNMe}_2)]_2$  (**3**), and  $[\text{Cu}(\mu\text{-I})(\text{PNpy})]_2$  (**4**) are investigated (compare Figure 3.1). The two copper centers in each compound are bridged by two halide atoms (chlorine, bromine, iodine). As chelating ligands, the aminophosphines  $\text{Ph}_2\text{P}(\text{o-C}_6\text{H}_4)\text{-N}(\text{CH}_3)_2$  ( $\text{PNMe}_2$ ) and  $\text{Ph}_2\text{P}(\text{o-C}_6\text{H}_4)\text{-NC}_4\text{H}_8$  ( $\text{PNpy}$ ) are used. A detailed photophysical characterization is carried out focusing on the TADF mechanism and on the lowest excited singlet and triplet state properties. In particular, the triplet state, studied down to  $T = 1.3\text{ K}$ , reflects details of the effectiveness of spin-orbit coupling (SOC) in halide-bridged copper compounds. The discussion given in this section is essentially following the one given in reference 36.

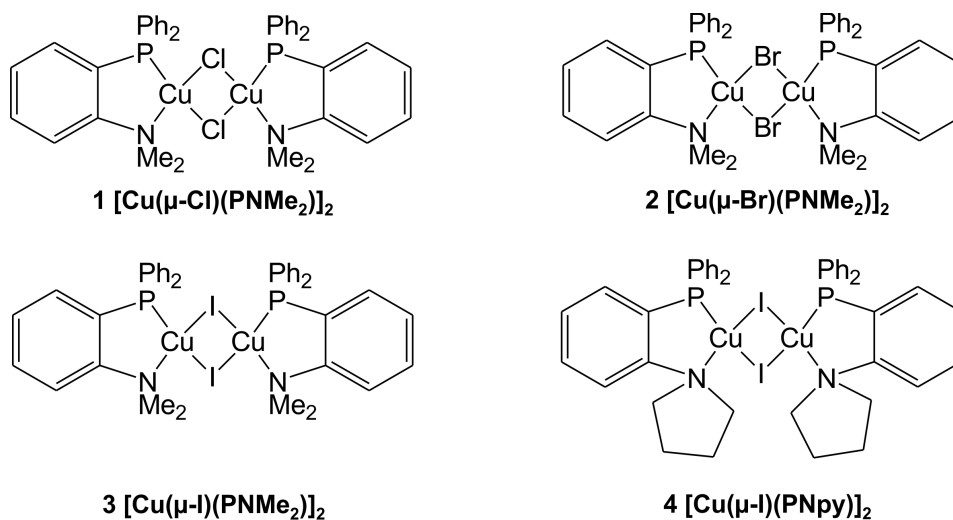


Figure 3.1: Chemical structures of compounds 1–4. Ph = Phenyl, Me = Methyl.

#### 3.1.1 Crystal Structures

In Figure 3.2, the structures of the four investigated compounds are displayed as received from X-ray measurements.<sup>i</sup> Important interatomic distances and angles are summarized in Table 3.1.

Two different coordination structures were found for the investigated substances. In compound **1**, the copper and halide atoms are located in one plane representing a planar

<sup>i</sup>X-ray measurements were performed by Fritz-Robert Kühle, University of Tübingen

Table 3.1: Selected interatomic distances and angles of the copper complexes **1**–**4** as obtained from X-ray analyses and from DFT calculations performed on the B3LYP/def2-SVP level of theory (calc.). X-ray data were provided by Fritz-Robert Küchle, University of Tübingen.

compound	<b>1</b>	<b>2</b>	<b>3</b>	<b>3</b> (calc.)	<b>4</b>
Cu(2)–X(1) [Å]	2.283(1)	2.499(1)	2.634(1)	2.695	2.646(1)
Cu(1)–X(1) [Å]	2.369(1)	2.418(1)	2.582(1)	2.660	2.597(1)
Cu(1)–X(2) [Å]	2.283(1)	2.542(1)	2.666(1)	2.695	2.646(1)
Cu(2)–X(2) [Å]	2.369(1)	2.417(1)	2.590(1)	2.659	2.597(1)
Cu(1)–Cu(2) [Å]	2.983(1)	2.559(1)	2.574(1)	2.689	2.688(1)
Cu(1)–N(1) [Å]	2.305(2)	2.248(1)	2.250(3)	2.566	2.328(3)
Cu(2)–N(2) [Å]	2.305(2)	2.231(1)	2.232(3)	2.573	2.328(3)
Cu(1)–P(1) [Å]	2.175(1)	2.190(1)	2.210(1)	2.284	2.222(1)
Cu(2)–P(2) [Å]	2.175(1)	2.189(1)	2.213(1)	2.283	2.222(1)
Cu(1)–X(1)–Cu(2) [°]	79.8(1)	62.7(2)	59.1(1)	60.3	61.7(2)
Cu(1)–X(2)–Cu(2) [°]	79.8(1)	62.1(2)	58.6(1)	60.3	61.7(2)
X(1)–Cu(1)–X(2) [°]	100.2(1)	100.0(1)	105.5(2)	112.5	107.4(1)
X(1)–Cu(2)–X(2) [°]	100.2(1)	101.3(1)	106.2(2)	112.5	107.4(1)
N(1)–Cu(1)–P(1) [°]	84.4(1)	83.6(1)	83.3(1)	77.3	82.4(1)
N(2)–Cu(2)–P(2) [°]	84.4(1)	85.0(1)	84.2(1)	77.1	82.4(1)
X(1)–Cu(2)–Cu(1)–X(2) [°]	0	128.2(1)	132.7(1)	148.1	139.6(1)

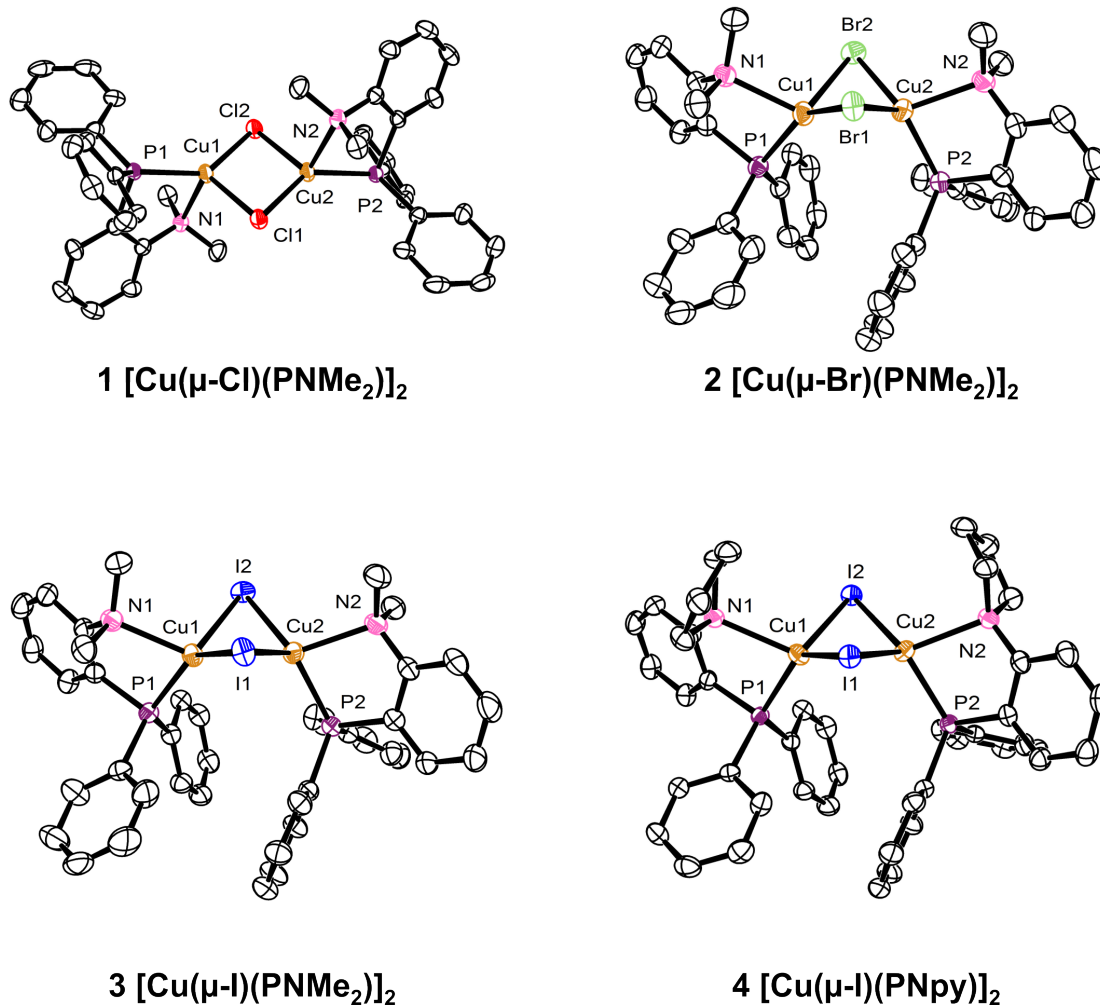


Figure 3.2: ORTEP representation (50% ellipsoids) of compounds **1–4** from X-ray structure determinations. Hydrogen atoms are not displayed for clarity. Crystal structures were provided by Fritz-Robert KÜchle, University of Tübingen.

geometry of the copper halide core. In contrast, for the compounds **2–4** these atoms include distinct dihedral angles  $\text{Br}(1)\text{-Cu}(2)\text{-Cu}(1)\text{-Br}(2)$  of  $128.2^\circ$  (**2**),  $\text{I}(1)\text{-Cu}(2)\text{-Cu}(1)\text{-I}(2)$  of  $132.7^\circ$  (**3**), and  $\text{I}(1)\text{-Cu}(2)\text{-Cu}(1)\text{-I}(2)$  of  $139.6^\circ$  (**4**) representing a butterfly type geometry of the copper halide core. Additionally, the orientation of the two ligands relative to each other differs between these two types of structures. More specifically, in the planar coordination, the phosphorus and nitrogen atoms of the ligands are in trans positions, whereas in the butterfly coordination they are in cis positions.

An analysis of the interatomic distances of the substances containing the  $\text{PNMe}_2$  ligand (compounds **1–3**) reveals that the lengths of the copper halide bonds ( $\text{Cu}(1)\text{--X}(1)$ ) increases from **1** (2.369 Å) to **2** (2.418 Å) to **3** (2.582 Å). This trend is also reflected in the other  $\text{Cu}\text{--X}$  bonds ( $\text{Cu}(1)\text{--X}(2)$ ,  $\text{Cu}(2)\text{--X}(1)$ , and  $\text{Cu}(2)\text{--X}(2)$ ) and is expected, as the radii of the halide atoms increase in the order  $\text{Cl} < \text{Br} < \text{I}$ . Moreover, a slightly larger  $\text{Cu}(1)\text{--Cu}(2)$  distance is found for **3** (2.574 Å) than that for **2** (2.559 Å). Replacing the  $\text{PNMe}_2$  ligand (compound **3**) by  $\text{PNpy}$  (compound **4**) leads to a significant increase of the  $\text{Cu}(1)\text{--Cu}(2)$  distance to 2.688 Å due to the increased steric demand of the ligand, more specifically of the cyclopentyl groups. However, compound **1** exhibits the largest  $\text{Cu}(1)\text{--Cu}(2)$  distance (2.983 Å), which is a result of the planar structure of the copper halide core of this molecule. Thus, large variations of the the  $\text{Cu}(1)\text{--Cu}(2)$  distances ranging from 2.56 Å to 2.98 Å are observed for the studied complexes **1–4**. Similarly large variations also occur for other halide-bridged dinuclear copper complexes.<sup>13,30,32,37,100–105</sup>

### 3.1.2 Computational Investigations

The type of the electronic transition and the characters of the involved molecular orbitals that contribute to the emission can be elucidated by carrying out density functional theory (DFT) and time-dependent density functional theory (TDDFT) calculations. Applying the B3LYP functional and the def2-SVP basis set, as suggested by Jesser et al.,<sup>107</sup> HOMO and LUMO contour curves are obtained for compound **3** for the (optimized) ground state geometry (Figure 3.3).

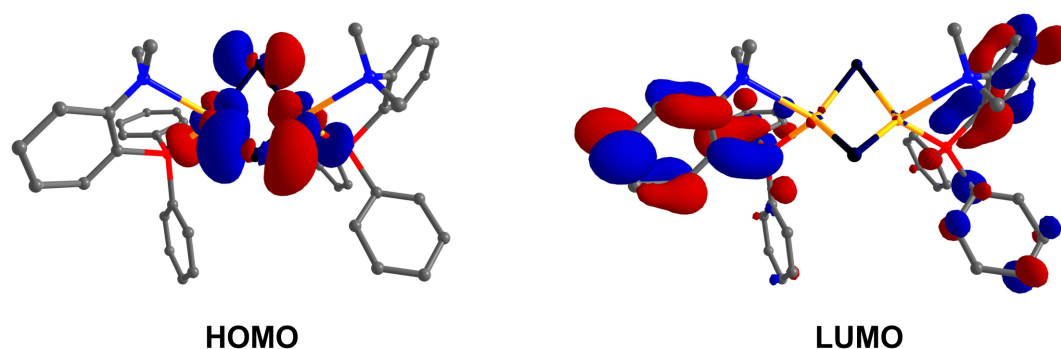


Figure 3.3: HOMO and LUMO of compound **3** for the ground state  $S_0$  geometry in the gas phase. The basis set used was def2-SVP. B3LYP was used as the functional.

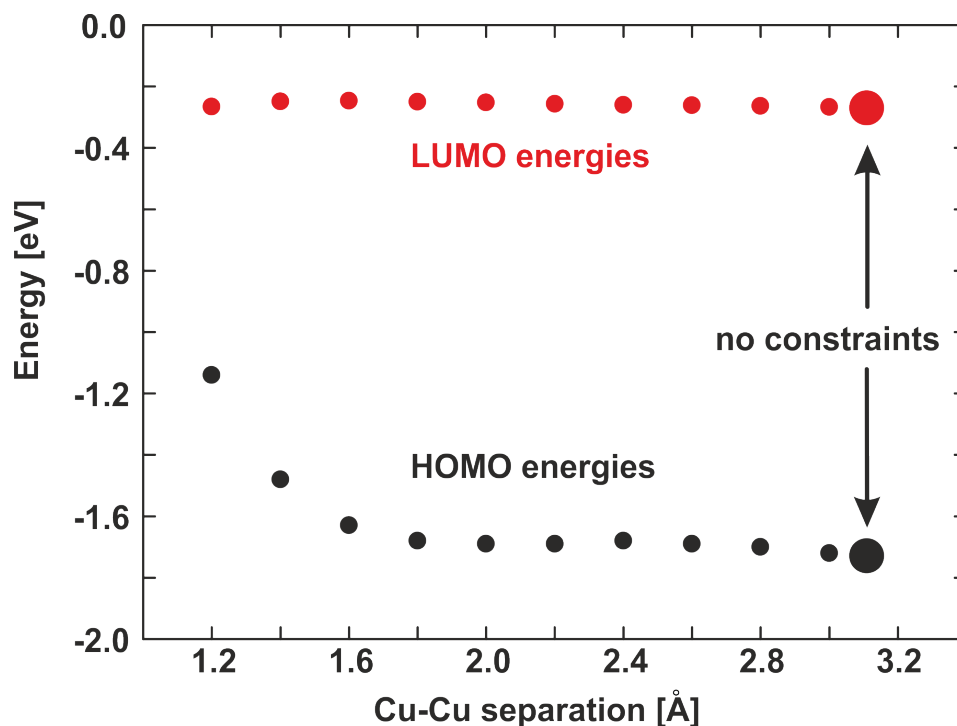


Figure 3.4: HOMO and LUMO energies of compound **1** in dependence of the Cu(1)–Cu(2) separation. For the results marked with the small dots, the Cu(1)–Cu(2) separations were constrained. The large dots indicate the results of a calculation without constraints. Calculations were performed on the B3LYP/def2-SVP level of theory.

The pronounced spatial separation of these frontier orbitals indicates that the HOMO–LUMO transition possesses significant charge transfer (CT) character. More specifically, with an excitation charge is transferred from the d orbitals of the copper and the p orbitals of the iodine atoms to the unoccupied orbitals. The latter ones are mainly located on the PNMe<sub>2</sub> ligands. Therefore, this transition can be assigned to be of (metal+halide)-to-ligand charge transfer ((M+X)LCT) character.

TDDFT calculations give an insight into the molecular orbital contributions to the electronic energy states. For example, for compound **3** the HOMO–LUMO transition contributes to the lowest excited singlet and triplet state by  $\approx 90\%$  and  $\approx 60\%$ , respectively. A further significant amount comes from the HOMO–2 to LUMO+1 transition, which amounts to  $\approx 10\%$  for the singlet and  $\approx 20\%$  for the triplet state. All contributing occupied orbitals (HOMO, HOMO–2) are located on copper and iodine, whereas all contributing unoccupied orbitals (LUMO, LUMO+1) are located on the



ligands. This means that the lowest excited states represent  $^1,^3(\text{M}+\text{X})\text{LCT}$  states. Such a significant CT character is usually connected with relatively broad and unstructured spectra. Indeed, the experimentally determined emission spectra are broad even at low temperatures and thus in agreement with this prediction (see next section and Figure 3.5).

DFT calculations also allow to investigate the influence of the Cu(1)–Cu(2) separation on the emission behavior. For this, the geometry of compound **1** was optimized while the separation of the Cu(1)–Cu(2) atoms was constraint to values between 1.2 Å and 3.0 Å. Without the constraint, a Cu(1)–Cu(2) separation of 3.1 Å is found. Interestingly, in a wide range of Cu(1)–Cu(2) separations, from about 1.8 Å to 3.1 Å, the HOMO and LUMO energies do not change significantly, indicating that also the emission energy should not change. While the LUMO energy is not affected if the distance of the copper centers is further decreased to values below 1.8 Å, an increase of the HOMO energy is observed presumably due to metal-metal interactions and a red shifted emission would be expected. However, compounds that exhibit such small Cu–Cu separations are not known. Therefore, it can be concluded that the Cu(1)–Cu(2) separation has negligible impact on the emission energy, especially for the compounds investigated in this section. A graphical representation of these results is displayed in Figure 3.4.

### 3.1.3 Spectroscopic Introduction

The studied compounds show intense blue (**3**, **4**) and green (**1**, **2**) luminescence under UV excitation. At first, the discussion will focus on the photophysical properties of compound **3**. The measurements were performed with powder samples due to the limited chemical stability of the substances in solution.<sup>108</sup> A justification for this approach is given below. Figure 3.5 shows the emission and excitation spectra measured at ambient and at liquid nitrogen temperature, respectively. With temperature variation, distinct changes of the emission properties are observed. At  $T = 77\text{ K}$ , the emission maximum lies at  $\lambda_{max}(77\text{ K}) = 471\text{ nm}$  (50% high energy flank at 443 nm), the decay time amounts to  $\tau(77\text{ K}) = 270\text{ }\mu\text{s}$ , and the quantum yield  $\Phi_{PL}(77\text{ K})$  is as high as almost 100%. According to this relatively long decay time and due to the detailed investigations at lower temperatures ( $T = 1.3\text{ K}$ , compare section 3.1.5), the emitting state at low temperature is assigned to be the triplet state  $T_1$  with a singlet ground state  $S_0$ . With temperature increase to  $T = 300\text{ K}$ , a slight blue-shift of the emission to

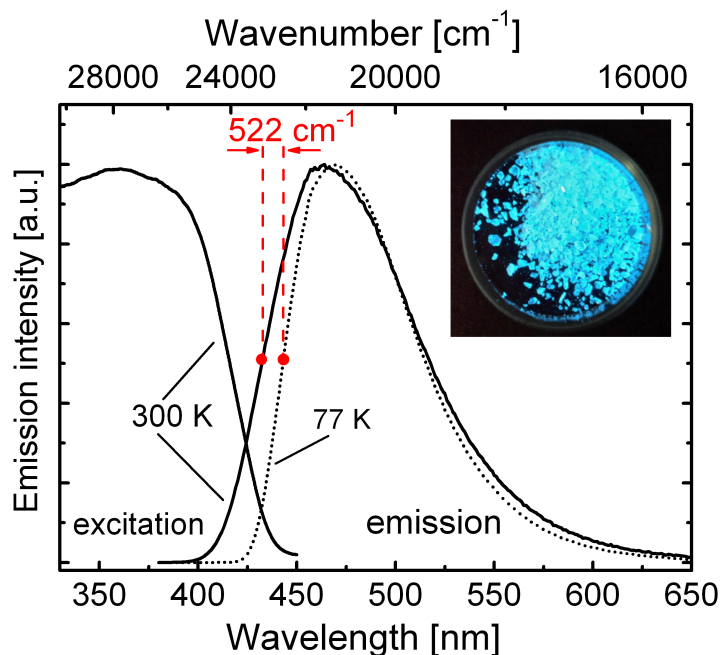


Figure 3.5: Emission and excitation spectra of compound **3** (powder) at ambient temperature (solid line) and at 77 K (dotted line). The emission spectrum was recorded under excitation at  $\lambda_{exc} = 360$  nm, and the excitation spectrum was detected at  $\lambda_{det} = 470$  nm. The inset shows a photo of the powder sample of compound **3** excited at 365 nm.

$\lambda_{max}(300\text{ K}) = 464$  nm (50 % high energy flank at 433 nm) and a drastic decrease of the emission decay time to  $\tau(300\text{ K}) = 4.6\ \mu\text{s}$  are observed, while the quantum yield decreases only slightly to  $\Phi_{PL}(300\text{ K}) = 65\%$ . A comparison of the quantum yields and decay times at the different temperatures reveals an interesting behavior. According to  $k_r = \Phi_{PL} \tau^{-1}$ , the corresponding radiative rates can be determined. The radiative rate increases from  $k_r(77\text{ K}) = 3.7 \times 10^3\ \text{s}^{-1}$  to  $k_r(300\text{ K}) = 1.4 \times 10^5\ \text{s}^{-1}$ , that is by more than a factor of 40. Obviously, with a temperature increase from 77 K to 300 K, a different emission process is thermally activated. In the following section, this behavior is assigned as a thermally activated delayed fluorescence (TADF).

Interestingly, concentration quenching in the powder samples, being usually connected with energy-transfer processes between adjacent molecules,<sup>109</sup> does not seem to be of importance for the studied complexes. This is indicated by the observed high emission quantum yields and the monoexponential decay behavior in the whole temperature range from approximately 30 K to 300 K. This behavior can be rationalized when the

character of the electronic transition is analyzed. On excitation, a significant amount of charge is transferred from the copper centers to the ligands resulting in a formal (partial) oxidation of Cu(I) to Cu(II). As Cu(I) prefers a tetrahedral whereas Cu(II) prefers a planar coordination environment, excitation results in a flattening distortion and in a lowering of the excited state energy.<sup>5,30,33,35,38,42,90–97,110</sup> As a consequence, the energy cannot be transferred from an excited to an adjacent non-excited molecule as the resonance condition for this process is not fulfilled. A related self-trapping behavior has been discussed in reference 111. In addition, it is remarked that in powders of other Cu(I) complexes such a self-trapping effect does not necessarily occur. In particular, this is observed for compounds that exhibit low-lying ligand-centered transitions of  $\pi\pi^*$  character with no significant geometry change and therefore no significant energy stabilization of the excited state on excitation.<sup>78,84</sup>

In Figure 3.6, ambient temperature emission spectra are reproduced for the four investigated compounds. Interestingly, for substances **3** and **4**, which both contain iodine as the bridging halide, no significant differences in the emission energy and shape of the spectrum are observed, although the Cu(1)–Cu(2) separations differ by more than 0.1 Å. This is in agreement with the DFT calculations presented in the previous section (Figure 3.4) which show that a change of the Cu(1)–Cu(2) separation from 2.6 Å to 2.7 Å should not have an impact on the emission energy. On the other hand, a remarkable blue-shift of the emission energies occurs in the series from **1** to **2** to **3,4**. The emission peak maxima lie at 506 nm (Cl), 490 nm (Br), and 464 or 465 nm (I). A similar shift is also observed for the emission maxima at  $T = 77$  K (mainly representing the triplet state emissions). DFT calculations show that the energy shift is essentially caused by a stabilization of the HOMO in the series from Cl, Br, and I, whereas the LUMO remains almost at the same energy. For completeness, it is remarked that this trend is in agreement with the effect that one would expect from a decrease of the ligand field strength in the series  $\text{Cl}^- > \text{Br}^- > \text{I}^-$ .<sup>102,112</sup>

In Table 3.2, photophysical data for the investigated compounds are summarized. The emission quantum yields at  $T = 300$  K are equal within limits of experimental error for the compounds **2–4** ( $\Phi_{PL} = 65\%$ ), whereas compound **1** exhibits a lower value of  $\Phi_{PL} = 45\%$ . However, the chemical structure of compound **1** differs from those of the other substances in the position of the copper and halide atoms relative to each other as well as in the orientation of the ligands (compare Figure 3.2). Therefore, a direct comparison of the photophysical properties of these two structure types is difficult.

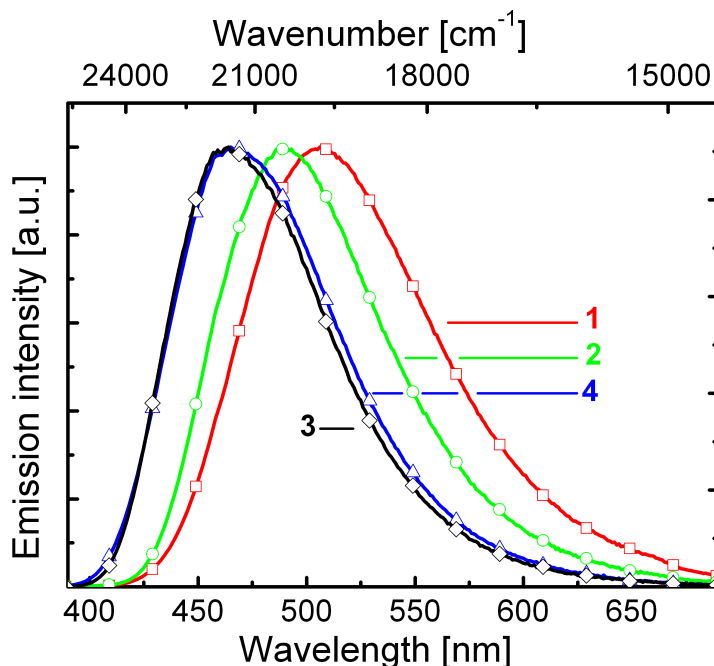
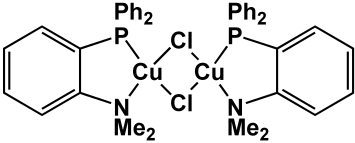
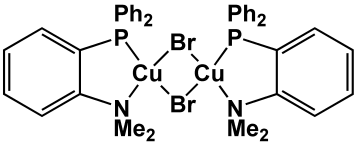
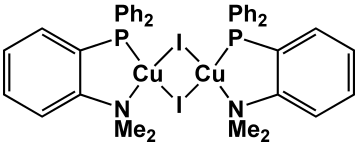
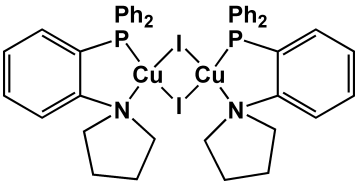


Figure 3.6: Emission spectra of substances  $[\text{Cu}(\mu\text{-Cl})(\text{PNMe}_2)]_2$  (**1**),  $[\text{Cu}(\mu\text{-Br})(\text{PNMe}_2)]_2$  (**2**),  $[\text{Cu}(\mu\text{-I})(\text{PNMe}_2)]_2$  (**3**), and  $[\text{Cu}(\mu\text{-I})(\text{PNpy})]_2$  (**4**) measured as powders at ambient temperature ( $\lambda_{exc} = 360$  nm).

Presumably, the lower quantum yield of **1** is related to a more flexible structure with respect to the excited state geometry changes, which results in an increase of nonradiative deactivation processes. Indeed, the much larger Cu(1)–Cu(2) separation found for **1** as compared to that of **2–4** (Table 3.1) supports this model. Furthermore, a comparison of the  $\Phi_{PL}$  values at ambient and liquid nitrogen temperatures reveals that an increase of the quantum yields occurs with decreasing temperature. A behavior like this is not unusual and is related to a decrease of the nonradiative deactivations on cooling.

The emission decay times measured at  $T = 300$  K for the four compounds do not differ significantly. They lie between about 4  $\mu\text{s}$  and 7  $\mu\text{s}$ . These values are mainly determined by the energy separations between the excited singlet  $S_1$  and triplet  $T_1$  states. A detailed discussion is found in the next section. On the other hand, at  $T = 77$  K, the emission decay times of the different compounds deviate significantly and range from 220  $\mu\text{s}$  to 930  $\mu\text{s}$ . These differences are related to spin-orbit coupling (SOC) being differently effective in the four compounds. Corresponding effects are discussed in more detail in section 3.1.5.

Table 3.2: Photophysical properties of the compounds **1**–**4** measured at ambient and at liquid nitrogen temperature in the powder phase.

compound	Temp. [K]	$\lambda_{max}$ [nm]	$\tau$ $\mu s$	$\Phi_{PL}$ [%]	$k_r$ [s <sup>-1</sup> ]
<b>1</b> 	300	506	6.6	45	$6.8 \times 10^4$
	77	513	220	100	$4.5 \times 10^3$
<b>2</b> 	300	490	4.1	65	$1.6 \times 10^5$
	77	498	930	100	$1.1 \times 10^3$
<b>3</b> 	300	464	4.6	65	$1.4 \times 10^5$
	77	471	270	100	$3.7 \times 10^3$
<b>4</b> 	300	465	5.6	65	$1.2 \times 10^5$
	77	465	250	100	$4.0 \times 10^3$

Similar as already described above for **3**, compounds **1** and **2** exhibit a red-shift of the emission when cooled to  $T = 77$  K. (For compound **4** this red-shift is only displayed at the high energy flanks of the emission spectra). The red-shift is accompanied by the drastic increase of the emission decay time but is not paralleled by an equally strong increase of the emission quantum yield. Obviously, cooling results in a drastic lowering of the radiative rates. This effect is most pronounced for compound **2** for which the radiative rate decreases by almost a factor of 150. The decrease of the radiative rates along with the red-shift of the emission with decreasing temperature indicates that all studied materials show the effect of TADF at ambient temperature. In the following section, this mechanism will be discussed in more detail.

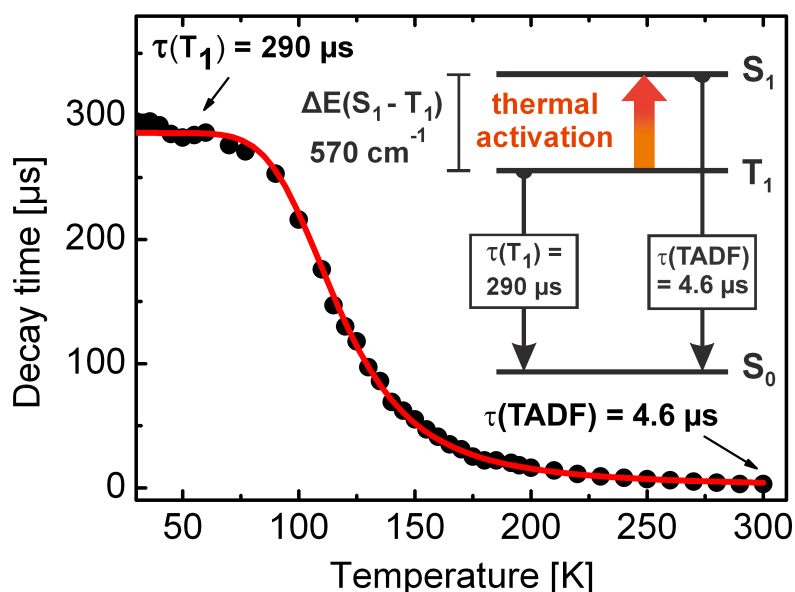


Figure 3.7: Temperature dependence of the emission decay time of substance **3** as powder. The solid red line represents a fit of the experimental data according to equation 3.1. The compounds were excited with a pulsed laser at a wavelength of 355 nm (pulse width  $\approx$  8 ns). The emission was detected at the maximum of each emission spectrum.

### 3.1.4 Thermally Activated Delayed Fluorescence

A deeper understanding of the emission properties is obtained by studying the decay time as a function of temperature in the range between 30 K and 300 K. In the entire temperature range, the decay is monoexponential. The result is depicted in Figure 3.7 for the example complex **3**.

For this compound, the emission decay time is almost constant in the temperature range between about 30 K and 60 K and one observes a plateau with  $\tau \approx 290 \mu\text{s}$ . According to the long decay time, this emission is assigned as phosphorescence from the triplet state T<sub>1</sub> to the ground state S<sub>0</sub>. Further evidence for the triplet character of this state is given in the next section. According to the discussion presented in the previous section, this triplet is of <sup>3</sup>(M+X)LCT parentage. With temperature increase, a strong reduction of the emission decay time is observed. This is attributed to a thermal activation of a higher lying electronic state, which carries significantly more allowedness for the transition to

the ground state than the  $T_1$  state. Therefore, the corresponding state is assigned as the lowest excited singlet state  $S_1$  being of  ${}^1(M+X)LCT$  character. This effect represents a TADF. At temperatures above  $T \approx 120$  K, the contribution of the singlet state to the emission dominates (see below, Figure 3.8). For thermally equilibrated states, the emission decay time of the two excited state system can be expressed as a function of the temperature according to equation 3.1. In the literature, such an approach has been described before for similar systems.<sup>1,6,8,9,32,33,35,39,42</sup>

$$\tau(T) = \frac{3 + \exp\left[-\frac{\Delta E(S_1 - T_1)}{k_B T}\right]}{3 \tau(T_1)^{-1} + \tau(S_1)^{-1} \exp\left[-\frac{\Delta E(S_1 - T_1)}{k_B T}\right]} \quad (3.1)$$

In this equation,  $k_B$  represents the Boltzmann constant, and  $\tau(S_1)$  and  $\tau(T_1)$  are the emission decay times of the singlet state  $S_1$  and triplet state  $T_1$ , respectively, in the absence of thermalization.  $\Delta E(S_1 - T_1)$  is the energy separation (activation energy) between these two states. Because in the temperature range investigated a monoexponential decay behavior was found, it can be concluded that in fact a fast thermalization between the two excited states occurs, and thus, equation 3.1 can be applied. Fitting the equation to the measured data allows determining the decay time of the prompt fluorescence to  $\tau(S_1) = 90$  ns, the decay time of the phosphorescence to  $\tau(T_1) = 290$   $\mu$ s (corresponding to the plateau seen in Figure 3.7), and the energy separation between the two states to  $\Delta E(S_1 - T_1) = 570$   $\text{cm}^{-1}$ . The short decay time of  $\tau(S_1) = 90$  ns determined for the thermally activated state substantiates its singlet character. Thus, the measured emission decay time at  $T = 300$  K of  $\tau(\text{TADF}) = 4.6$   $\mu$ s represents a  $S_1 \rightarrow S_0$  fluorescence, which, however, because it is fed from the long-lived triplet state reservoir, represents a delayed fluorescence. It is remarked that despite this short decay time of the singlet state, no prompt fluorescence is directly observed. This indicates that  $S_1 \rightarrow T_1$  intersystem crossing (ISC) is much faster than the emission process. Experimentally determined ISC times of  $\approx 10$  ps found for other Cu(I) compounds support this.<sup>79,86,87</sup>

The energy separation between the singlet  $S_1$  and the triplet  $T_1$  states with  $\Delta E(S_1 - T_1) = 570$   $\text{cm}^{-1}$  is very small as compared to other organo-transition metal complexes, such as Pd(II) or Pt(II) compounds with  $\Delta E(S_1 - T_1)$  values of several  $10^3$   $\text{cm}^{-1}$ .<sup>76,113</sup> This behavior of the Cu(I)-compounds is ascribed to be a consequence of the distinct spatial separation of the occupied and unoccupied frontier orbitals, in particular, of the

HOMO and LUMO, which leads to a small electron exchange interaction and therefore to a small singlet-triplet energy splitting (compare for example reference 114).

An alternative approach to determine the energy separation  $\Delta E(S_1 - T_1)$  is to compare the emission spectra at  $T = 77$  K (almost pure triplet emission) and  $T = 300$  K (almost pure singlet emission). The energy separation of these spectra, taken at the high-energy flank at 50 % of the maximum intensity, amounts to  $\Delta E(S_1 - T_1) = 522 \text{ cm}^{-1}$  (Figure 3.6) and thus matches well to the value found from the fit procedure. The spectral blue-shift of the emission towards higher temperatures substantiates further that an energetically higher lying electronic state is thermally populated. This strongly indicates that TADF is the dominant emission mechanism of this compound at high temperatures. It is remarked that the determination of  $\Delta E(S_1 - T_1)$  from the spectral shift is less accurate compared to the indirect method based on the analysis of the temperature dependent change of the emission decay time. One reason for this is that on heating temperature induced spectral broadening can occur which can mask spectral shifts.

For the compounds **1**, **2**, and **4**, similar investigations with respect to the temperature dependence of the decay times have been carried out. The resulting data are summarized in Table 3.3. An analysis of these data allows to come to a better understanding of the emission process. All compounds exhibit small values for the singlet-triplet splitting  $\Delta E(S_1 - T_1)$  ranging from  $460 \text{ cm}^{-1}$  to  $630 \text{ cm}^{-1}$  and therefore, show pronounced TADF at ambient temperature. For the triplet decay times  $\tau(T_1)$ , distinctly different values are found. A more detailed discussion of this property is presented in the following section. For the decay time of the singlet state  $\tau(S_1)$  (obtained from the fitting procedure), values amounting to 90 ns to 210 ns are determined. Hereby, compounds **2**, **3**, and **4** show very similar singlet decay times of 90 ns to 110 ns, while compound **1** exhibits a by a factor of about two longer decay time of 210 ns. This can be a consequence of a more distinct charge transfer that is connected with a smaller transition dipole moment of the corresponding transition, leading to a weaker allowedness. Moreover, the more pronounced charge transfer character should also result in a smaller value for  $\Delta E(S_1 - T_1)$  as the wave functions' overlap is smaller, which results in a smaller exchange interaction. Indeed, complex **1** shows the smallest  $\Delta E(S_1 - T_1)$  value of the investigated substances. A detailed discussion of this aspect is given in section 3.2.3. The more distinct charge transfer character of the  $S_1 \rightarrow S_0$  fluorescence in compound **1** could be a result of the different molecular geometry of compound **1** compared to the other substances (compare Figure 3.2). This assumption is supported by the investigations



Table 3.3: Overview of the properties of the first excited singlet and triplet states of the investigated substances

compound (powder)	<b>1</b>	<b>2</b>	<b>3</b>	<b>4</b>
$\Delta E(S_1 - T_1)^a$ [cm <sup>-1</sup> ]	460	510	570	630
$\tau(T_1)^a$ [ $\mu$ s]	250	1200	290	250
$\tau(S_1)^a$ [ns]	210	110	90	100
$\tau(\text{TADF})^b$ [ $\mu$ s]	6.6	4.1	4.6	5.6

<sup>a</sup> From the fit<sup>b</sup> Measured at  $T = 300$  K

performed in section 4.2 which reveal a strong dependence of the singlet-triplet energy separation on the coordination geometry. At ambient temperature, the decay times of the delayed fluorescence  $\tau(\text{TADF})$  range from 4.1  $\mu$ s to 6.6  $\mu$ s. These values are governed by the singlet decay times  $\tau(S_1)$  and the singlet-triplet energy splittings  $\Delta E(S_1 - T_1)$  of the respective compounds. The influence of the triplet decay time  $\tau(T_1)$  on  $\tau(\text{TADF})$  can be neglected for these compounds at ambient temperature. Interestingly, compound **1**, which exhibits the smallest  $\Delta E(S_1 - T_1)$  value, also shows the longest delayed fluorescence decay time of  $\tau(\text{TADF}) = 6.6 \mu$ s. This is a consequence of the relatively long singlet decay time of  $\tau(S_1) = 210$  ns, as is discussed in detail in the section 3.2.3.

It is illustrative to visualize the percentage of the emission intensity originating from the singlet  $I(S_1)$  and from the triplet state  $I(T_1)$  relative to the total emission intensity  $I_{tot}$  in dependence of the temperature.  $I(S_1)$  is proportional to the population of the singlet state  $N(S_1)$  and to the radiative rate constant  $k_r(S_1)$  of this state for the deactivation to the groundstate.

$$I(S_1) = \alpha k_r(S_1)N(S_1) \quad (3.2)$$

In the same way,  $I(T_1)$  is given by

$$I(T_1) = \alpha k_r(T_1)N(T_1) \quad (3.3)$$

Hereby,  $\alpha$  is a proportionality constant that is equal in both equations. The radiative rate  $k_r(S_1)$  and  $k_r(T_1)$  can be expressed in terms of the quantum yields and the emission decay times according to  $k_r = \Phi_{PL} \tau^{-1}$ . For this rough estimate, it is further assumed that the quantum yields  $\Phi_{PL}(S_1)$  and  $\Phi_{PL}(T_1)$  do not depend on the temperature. With this,  $I_{tot} = I(S_1) + I(T_1)$ , and assuming that the populations of both states follow a Boltzmann distribution (fast equilibration), one obtains

$$\begin{aligned} \frac{I(T_1)}{I_{tot}} &= \left[ 1 + \frac{k_r(S_1)g(S_1)}{k_r(T_1)g(T_1)} e^{-\frac{\Delta E(S_1-T_1)}{k_B T}} \right]^{-1} \\ &= \left[ 1 + \frac{\Phi_{PL}(S_1)\tau(T_1)}{3\Phi_{PL}(T_1)\tau(S_1)} e^{-\frac{\Delta E(S_1-T_1)}{k_B T}} \right]^{-1} \end{aligned} \quad (3.4)$$

$g(S_1) = 1$  and  $g(T_1) = 3$  are the degeneracy factors for the singlet and triplet states, respectively. Using  $I(T_1) = I_{tot} - I(S_1)$  leads to

$$\frac{I(S_1)}{I_{tot}} = 1 - \left[ 1 + \frac{\Phi_{PL}(S_1)\tau(T_1)}{3\Phi_{PL}(T_1)\tau(S_1)} e^{-\frac{\Delta E(S_1-T_1)}{k_B T}} \right]^{-1} \quad (3.5)$$

Applying equations 3.4 and 3.5 and using the fit parameters as determined for compound **3** ( $\Delta E(S_1 - T_1) = 570 \text{ cm}^{-1}$ ,  $\tau(S_1) = 90 \text{ ns}$ ,  $\tau(T_1) = 290 \text{ }\mu\text{s}$ ,  $\Phi_{PL}(S_1) = 0.65$ , and  $\Phi_{PL}(T_1) = 1.0$ ), the plots shown in Figure 3.8 are obtained. At low temperature ( $T < 60 \text{ K}$ ), only a  $T_1$  phosphorescence occurs. With temperature increase, the intensity contributed from the  $T_1$  state decreases, while the intensity stemming from the  $S_1$  state increases. At  $T = 300 \text{ K}$ , almost all intensity (98 %) stems from the singlet state.

### 3.1.5 The Triplet State $T_1$

The triplet state  $T_1$  of the studied Cu(I) complexes is assigned as being of  $^3(M+X)LCT$  character, which is based on DFT and TDDFT calculations (Figure 3.3). Additionally, the occurrence of only broad-band emission spectra even at low temperatures and of small  $\Delta E(S_1 - T_1)$  values support this assignment. Literature classifications carried out for similar Cu(I) complexes come to equivalent characterizations.<sup>13,30,32,37,100-106</sup> The triplet state usually splits into three triplet substates. In organo-transition metal complexes, the corresponding energy splitting of the three substates, the zero-field

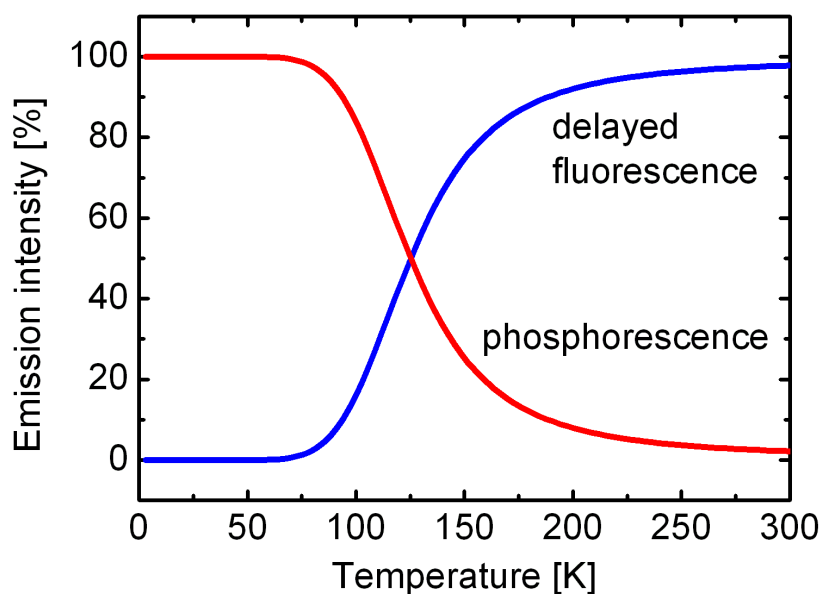


Figure 3.8: Emission intensities stemming from the singlet state  $S_1$  (delayed fluorescence) and the triplet state  $T_1$  (phosphorescence), normalized to the total intensity  $I_{tot} = I(S_1) + I(T_1)$  in dependence of temperature according to equations 3.4 and 3.5. The parameters used are the ones found for compound **3** ( $\Delta E(S_1 - T_1) = 570 \text{ cm}^{-1}$ ,  $\tau(T_1) = 290 \text{ }\mu\text{s}$ ,  $\tau(S_1) = 90 \text{ ns}$ ,  $\Phi_{PL}(S_1) = 0.65$ , and  $\Phi_{PL}(T_1) = 1.0$ ).

splitting (ZFS), is essentially determined by spin-orbit coupling to higher lying singlet and triplet states.<sup>5,6,88,92,115,116</sup> For emitting complexes, it is interesting to learn about these substates. However, detailed studies for Cu(I) complexes are only rarely found. For example, theoretical investigations are reported in reference 92, while first experimental investigations have been carried out only recently.<sup>33,106</sup> The reason why an experimental access to triplet substate properties of Cu(I) complexes is difficult is related to the occurrence of only very broad charge-transfer spectra (resulting from strong electron-phonon coupling<sup>23</sup>) and thus to the difficulty of resolving the individual substates. Moreover, at temperatures higher than about 15 K, relaxation processes thermalize the individual population of the three substates in a time faster than that of the individual substate emission. Therefore, the information about the individual substate is lost. Accordingly, adequate investigations require measurements at very low temperature, that is when fast processes of thermalization due to spin-lattice relaxation (SLR) are largely

frozen out, at least for small  $\Delta E(\text{ZFS})$  values.<sup>33,75,76,117–120</sup> If so, individual substates can become observable, at least indirectly on the basis of the decay time behavior. Hence, the investigations of the triplet state properties are extended down to  $T = 1.3\text{ K}$ . In the following, the discussion will focus on compound **1**.

Figure 3.9 displays the emission decay behavior of compound **1** in dependence of the temperature. In the range of  $15\text{ K} < T < 300\text{ K}$ , the decay is monoexponential, and a very similar trend is observed as that for compound **3** (compare Figure 3.7). Fitting the measured data with equation 3.1 gives values of  $\Delta E(\text{S}_1 - \text{T}_1) = 460\text{ cm}^{-1}$  and  $\tau(\text{S}_1) = 210\text{ ns}$  (compare Figure 3.9, inset). The decay time of the  $\text{T}_1$  state, represented by the plateau, lies at  $\tau(\text{T}_1) = 250\text{ }\mu\text{s}$ . This value displays the emission decay time of all three triplet substates if thermally equilibrated (compare Figure 3.9 right-hand side, blue marked range). However, below  $T \approx 15\text{ K}$ , the emission decay becomes more and more non-monoexponential, and at  $T = 1.3\text{ K}$ , the decay curve can be fitted well with a tri-exponential function which gives the three decay components  $\tau_I = 2.8\text{ ms}$ ,  $\tau_{II} = 1.0\text{ ms}$ , and  $\tau_{III} = 90\text{ }\mu\text{s}$  (Figure 3.10). A similar three-component decay has frequently been observed for other organo-transition metal compounds, such as Pd(II),<sup>76,121</sup> Pt(II),<sup>76,122,123</sup> Ir(III),<sup>119</sup> Re(I),<sup>120</sup> and other Cu(I)<sup>33</sup> complexes. The different decay components have been assigned to the emissions from the three individual triplet substates, which are zero-field split by less than 1 or  $2\text{ cm}^{-1}$  and in several cases even much less.<sup>75,76</sup> Such a behavior is a consequence of very slow spin-lattice relaxation (SLR) processes between energetically near-lying substates at very low temperature.<sup>ii</sup> An equivalent assignment is also applied to the investigated Cu(I) compound and thus, the energy level diagram shown as inset in Figure 3.10 is obtained.

Obviously, the discussion presented above implies that below  $T \approx 15\text{ K}$ , equation 3.1 does not hold to describe the decay behavior (no thermalization). Nevertheless, in Figure 3.9, the plot is extended to temperatures below  $15\text{ K}$  to visualize the drastic increase of the longest emission decay component. Interestingly, below  $T \approx 3\text{ K}$ , a second plateau is observed for this long component. It simply signifies that a further temperature decrease would not lead to a significant population change between the different substates.

In the case of a fast thermalization and for  $\Delta E(\text{ZFS}) \ll k_B T$ , the averaged emission

---

<sup>ii</sup>An occurrence of a distinctly larger energy separation  $\Delta(\text{ZFS})$  between the triplet substates is not probable because a splitting of already a few  $\text{cm}^{-1}$  would induce decay components of less than a few  $\mu\text{s}$  according to fast spin-lattice relaxation processes even at  $T = 1.3\text{ K}$  (compare references 75, 124–126). However, correspondingly short decay components have not been observed.

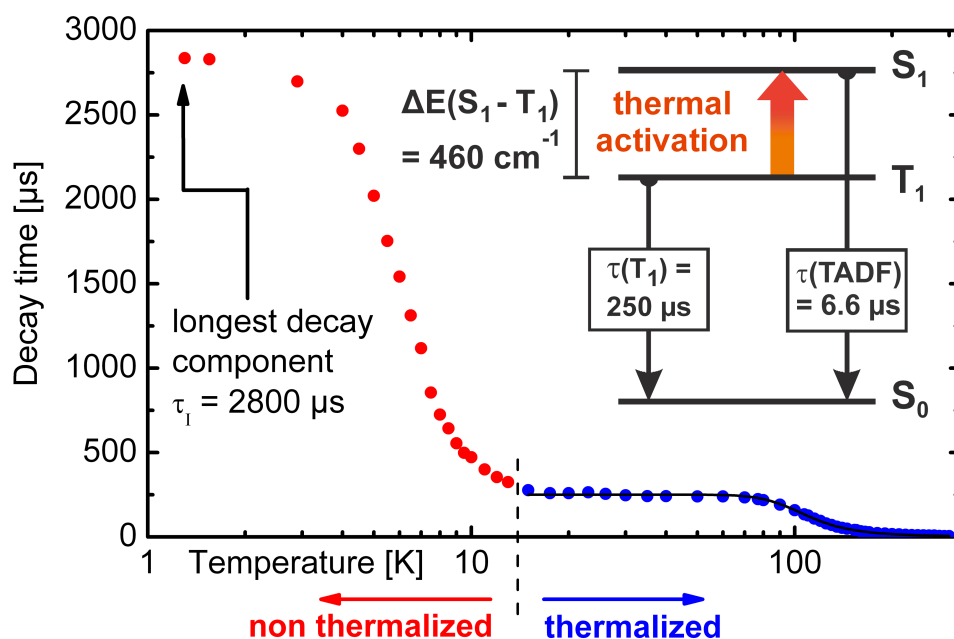


Figure 3.9: Emission decay time of compound **1** versus temperature. In the temperature range above  $\approx 15$  K, the three triplet substates are in a fast thermal equilibrium and only one decay component can be observed. At temperatures higher than  $\approx 60$  K, the singlet state  $S_1$  becomes thermally populated, resulting in a reduction of the emission decay time. At ambient temperature, the process of TADF leads to a decay time of  $\tau(\text{TADF}) = 6.6 \mu\text{s}$ . In the inset, an energy level diagram of compound **1** is shown. With decreasing temperature below  $\approx 15$  K, the emission decay deviates more and more from a monoexponential decay. In this part of the plot, only the longest decay component of the non-monoexponential function is displayed (compare Figure 3.10).

decay time  $\tau_{av}$  of the three triplet substates can be expressed by the three individual decay times according to equation 3.6.<sup>76,117</sup>

$$\tau_{av} = 3 \left[ \frac{1}{\tau_I} + \frac{1}{\tau_{II}} + \frac{1}{\tau_{III}} \right]^{-1} \quad (3.6)$$

$\tau_I$ ,  $\tau_{II}$ , and  $\tau_{III}$  represent the emission decay times of the individual triplet substates I, II, and III.

If the individual substate decay times as determined from the 1.3 K decay curve (Figure

3.10) are inserted, a value of  $\tau_{av} = 241 \mu\text{s}$  is obtained. This value agrees well with the observed decay time of the plateau of  $\tau(T_1) = 250 \mu\text{s}$ . The pronounced correspondence substantiates that the three decay components determined at  $T = 1.3 \text{ K}$  originate indeed from the three triplet substates of the  $T_1$  state.

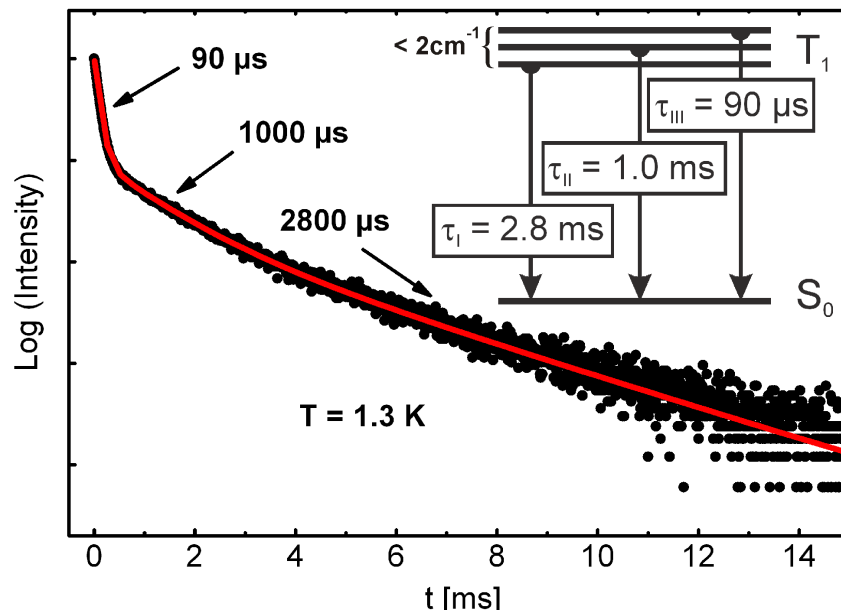


Figure 3.10: Emission decay behavior of compound **1** at  $T = 1.3 \text{ K}$ . Pulsed excitation at  $\lambda_{exc} = 355 \text{ nm}$ . The inset shows the triplet state  $T_1$  with its substates I, II, and III and their respective individual decay times. The corresponding zero-field splitting is less than  $2 \text{ cm}^{-1}$ .

Equivalent studies as discussed above have also been carried out for the compounds **2**, **3**, and **4** (Table 3.4). For example, the decay components of **3** were determined to be  $\tau_{\text{I}} = 1.8 \text{ ms}$ ,  $\tau_{\text{II}} = 630 \mu\text{s}$ , and  $\tau_{\text{III}} = 110 \mu\text{s}$ . Using equation 3.6, this results in  $\tau_{av} = 267 \mu\text{s}$ . Within limits of experimental error of about 10 %, also this value fits well to the measured decay time in the range of the plateau with  $\tau = 290 \mu\text{s}$ . This holds similarly for the compounds **2** and **4**.

The individual decay components display some interesting trends. If the nonradiative processes are ignored ( $T = 1.3 \text{ K}$ ), the radiative decay time can be used as a measure of the allowedness of the radiative transition rate. Thus, it is seen that all transition rates are very small. This becomes apparent when the corresponding values are compared to those of other transition metal complexes, such as the triplet substates of  $\text{Ir}(\text{ppy})_3$ ,

Table 3.4: Emission decay times of the triplet state  $T_1$  and its respective substates I, II, and III.

compound	<b>1</b>	<b>2</b>	<b>3</b>	<b>4</b>	$\text{Ir}(\text{ppy})_3^a$
$\tau_I [\mu\text{s}]^b$	2800	2200	1800	1500	116
$\tau_{II} [\mu\text{s}]^b$	1000	1100	630	500	6.6
$\tau_{III} [\mu\text{s}]^b$	90	850	110	110	0.2
$\tau_{av} [\mu\text{s}]^c$	241	1181	267	255	
$\tau(30\text{ K}) [\mu\text{s}]^d$	250	1200	300	270	

<sup>a</sup> Data from reference 65 for comparison

<sup>b</sup> The error in the fit of the decay components is 10 %

<sup>c</sup> Decay time of the triplet state  $T_1$  calculated according to equation 3.6

<sup>d</sup> Experimentally determined decay time of the  $T_1$  state

given in Table 3.4 for comparison. In particular, the radiative rates of  $\text{Ir}(\text{ppy})_3$  are several orders of magnitude larger than those of the  $\text{Cu}(\text{I})$  complexes. Obviously, this is a consequence of the effectiveness of SOC of the corresponding substates to higher-lying singlet states.<sup>5,65,88,92,115,116,123,127–129</sup> Trends are also seen when the different copper complexes are compared. The decay time of substate I decreases in the series of **1** (Cl), **2** (Br), **3** (I), **4** (I) and thus displays some influence of the increasing SOC constant from Cl (SOC constant  $\xi = 587\text{ cm}^{-1}$ ), to Br ( $\xi = 2460\text{ cm}^{-1}$ ), to I ( $\xi = 5069\text{ cm}^{-1}$ ).<sup>130</sup> However, a corresponding trend does not occur for the decay times of substate III if **1** (Cl) is compared with **2** (Br), but these compounds have different chemical structures (Figure 2). Apparently, the individual structure influences the effectiveness of SOC. Interestingly, the trend of increasing SOC induced by the halides is again observed (with respect to substate III) if **2** (Br) and **3** (I) are compared. Both compounds have similar molecular structures.

Interestingly, most organo-transition metal compounds frequently exhibit orders of magnitude different emission decay times of the three triplet substates (compare the values given for  $\text{Ir}(\text{ppy})_3$  (Table 3.4) and many other compounds discussed in reference 5). This trend is also clearly seen for compounds **1**, **3**, and **4** but not for compound **2**. Obviously, for this compound, SOC of all three substates to higher-lying singlets is not very different. In this respect, compound **2** represents a very rare example. It is remarked that more

detailed assignments concerning SOC paths would require theoretical calculations that include SOC. Such investigations have not been carried out for the studied compounds and only very rarely for other organo-transition metal compounds.<sup>115,127–129,131</sup>

A further aspect should be addressed. The lowest triplet states of the studied copper complexes have been assigned as  $^3(\text{M}+\text{X})\text{LCT}$  states. According to Figure 3.3, the Cu(I) metal and halide atoms X are involved in the HOMO and, as discussed in section 3.1.3, also in the HOMO–1. Because, according to TDDFT calculations, transitions from these occupied MOs determine the lowest excited triplet and singlet states, one would expect that the relatively heavy atoms with SOC constants of  $\xi(\text{Cu}) = 857 \text{ cm}^{-1}$  and  $\xi(\text{I}) = 5069 \text{ cm}^{-1}$  for **3** and **4** would have a strong influence on the triplet state properties such as large ZFSs and short triplet decay times. However, this is not observed experimentally. Obviously, further investigations are required in this respect.

### 3.1.6 Concluding Remarks

In this chapter four halide bridged Cu(I) dimers with chelating aminophosphine ligands were structurally analyzed and photophysically characterized. At ambient temperature, the complexes exhibit high photoluminescence quantum yields (up to 65 %) and relatively short emission decay times (as low as about 4  $\mu\text{s}$ ), and the emission color can be tuned from green to blue by variation of the halide X. The involved electronic transitions are assigned to (metal+halide)-to-ligand CT character. Accordingly, the lowest excited singlet ( $\text{S}_1$ ) and triplet ( $\text{T}_1$ ) states are designated as  $^1,^3(\text{M}+\text{X})\text{LCT}$  states. With these transitions, a distinct CT is connected. Hence, the quantum mechanical exchange interaction and, thus, the resulting energy separations between the  $\text{S}_1$  and  $\text{T}_1$  states  $\Delta E(\text{S}_1 - \text{T}_1)$  are expected to become relatively small. Indeed, the experimentally determined values amount only to a few hundred  $\text{cm}^{-1}$  and thus belong to the smallest energy separations reported for Cu(I) compounds reported so far. As a consequence, these materials are highly attractive candidates for studies and applications of TADF. For example, compound **3** ( $[\text{Cu}(\mu\text{-I})(\text{PNMe}_2)]_2$ ), representing a blue-light emitter ( $\lambda_{\text{max}} = 464 \text{ nm}$ , CIE color coordinates (0.16;0.22)) exhibits an activation energy for the TADF process of  $\Delta E(\text{S}_1 - \text{T}_1) = 570 \text{ cm}^{-1}$ . According to the drastically higher allowedness of the  $\text{S}_1 \rightarrow \text{S}_0$  with respect to the  $\text{T}_1 \rightarrow \text{S}_0$  transition, radiative deactivation occurs via the  $\text{S}_1$  state, if thermally activated. Thus, at ambient temperature, the observed emission stems almost completely from the  $\text{S}_1$  state (98 %). Only 2 % results from the  $\text{T}_1$  state. Consequently,



the ambient temperature emission represents a fluorescence, though thermally activated from the long-lived triplet state reservoir. Hence, the emission is a  $S_1 \rightarrow S_0$  delayed fluorescence. For compound **3**, it decays with a time constant of  $\tau(\text{TADF}) = 4.6 \mu\text{s}$  at ambient temperature. For compound **3**, an overview of the relevant states for the emission process and their respective decay paths is given in Figure 3.11. For completeness, it is remarked that a prompt fluorescence has not been observed. Obviously, this is a consequence of a down-ISC time from the  $S_1$  to the  $T_1$  state being significantly shorter than the prompt emission decay time of 90 ns as determined from a fit procedure. This is in agreement with ISC time constants of about 10 ps found for other Cu(I) compounds.<sup>79,86,87</sup>

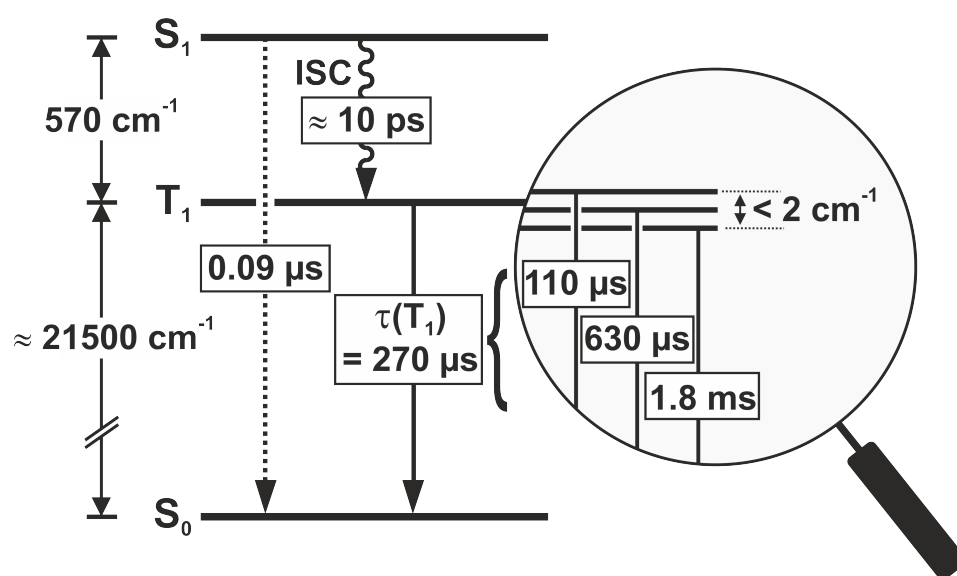


Figure 3.11: Energy level diagram and decay times of the lowest excited states for  $[\text{Cu}(\mu\text{-I})(\text{PNMe}_2)_2]_2$  (compound **3**). Adapted from reference 106.

## 3.2 Complexes with Diphosphine Ligands

In this section, the Cu(I) complex  $\text{Cu}_2\text{Cl}_2(\text{dppb})_2$  and the corresponding Ag(I) homologue  $\text{Ag}_2\text{Cl}_2(\text{dppb})_2$  are investigated (Figure 3.12). Similarly as for the complexes discussed in the previous section, the two metal centers are bridged by two halide, more specifically, by two chlorine atoms. Here, as chelating ligand dppb (1,2-bis-(diphenylphosphino)benzene), representing a diphosphine ligand, was used, in contrast to the aminophosphine ligand from the previous section. Parts of this chapter have been published previously in reference 41.

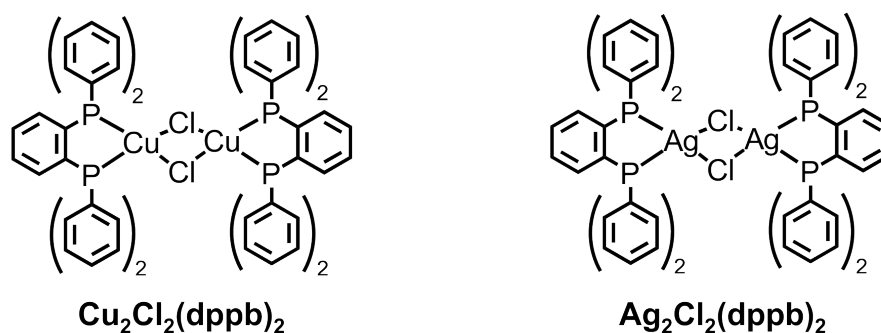


Figure 3.12: Chemical structures of the investigated compounds.

### 3.2.1 DFT and TDDFT Calculations

To get insight into the electronic structures of  $\text{Cu}_2\text{Cl}_2(\text{dppb})_2$  and  $\text{Ag}_2\text{Cl}_2(\text{dppb})_2$ , density functional theory (DFT) and time-dependent density functional theory (TDDFT) calculations were performed on the B3LYP/def2-SVP level of theory, which has shown to give good results for other Cu(I) complexes.<sup>107</sup> As input geometry, the atom coordinates received from X-ray structure determination of  $\text{Cu}_2\text{Cl}_2(\text{dppb})_2$  were used.<sup>iii</sup> For the calculations of  $\text{Ag}_2\text{Cl}_2(\text{dppb})_2$ , the Cu atoms in the input file were replaced by Ag as for this complex no crystals suitable for X-ray structure determinations could be obtained.

At first, geometry optimizations for the singlet ground state were performed for both compounds. For these geometries, it was found that the first excited singlet and triplet states largely result from transitions between molecular orbitals that are centered at the metals and the chlorides and at the ligands, respectively. Accordingly, the corresponding transitions are of (metal+halide)-to-ligand charge transfer ((M+X)LCT)

<sup>iii</sup>X-ray data provided by Rafał Czerwieniec, University of Regensburg

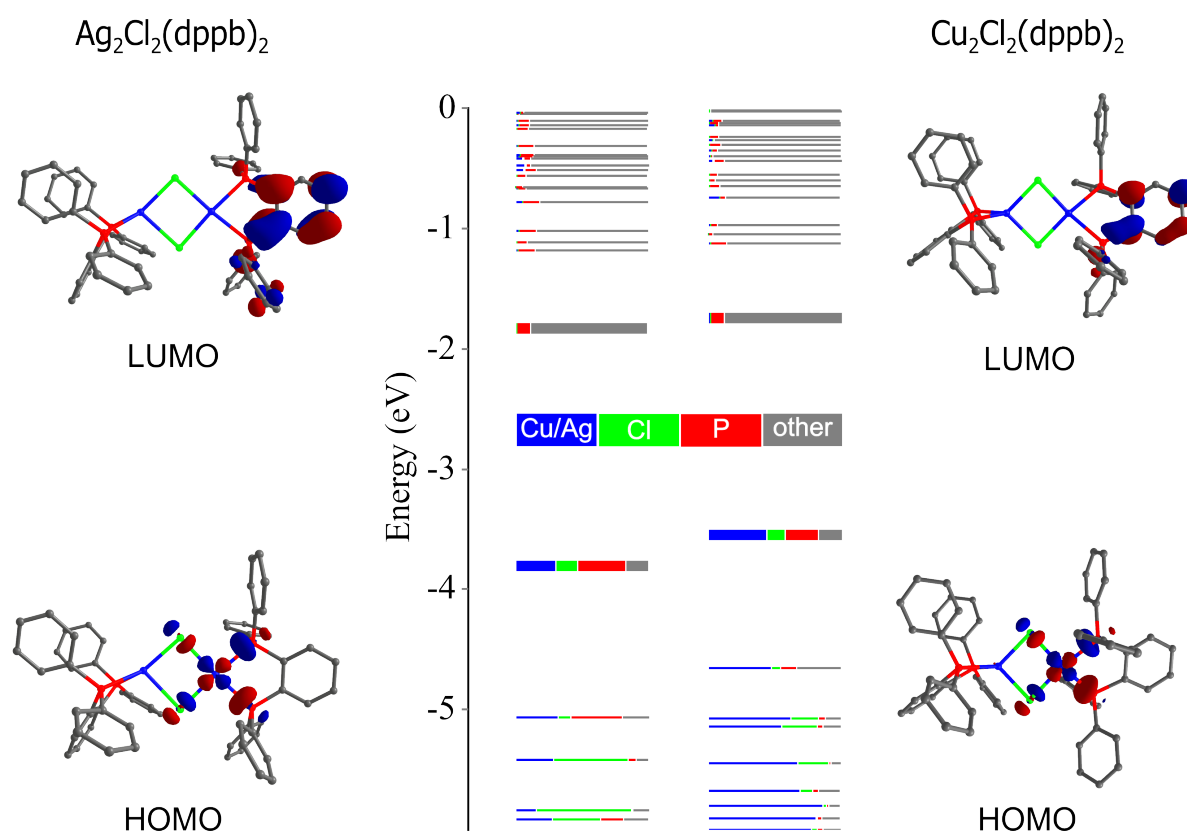


Figure 3.13: Energy positions of molecular orbitals of  $\text{Ag}_2\text{Cl}_2(\text{dppb})_2$  and  $\text{Cu}_2\text{Cl}_2(\text{dppb})_2$  as obtained from DFT calculations for the optimized  $T_1$  state geometry. HOMO and LUMO orbitals are represented by the bold lines. Relative contributions of the different atoms to the molecular orbitals are color coded. In addition, the contour plots of the HOMOs and LUMOs are displayed for both compounds.

character. This is in agreement with the results found for the aminophosphine complexes discussed in the previous section and with literature reports of other Cu(I) and Ag(I) complexes.<sup>30,100,102,106,132</sup> However, for a description of the emission properties of  $\text{Cu}_2\text{Cl}_2(\text{dppb})_2$  and  $\text{Ag}_2\text{Cl}_2(\text{dppb})_2$ , the triplet geometry is more suited. Therefore, an optimization of the lowest excited triplet state geometry was performed. The resulting structures differ distinctly from those of the ground state for both compounds. More specifically, in the triplet state geometry, *one* of the two dppb ligands is rotated by about  $90^\circ$  along the axis which connects the two metal centers. This significant distortion is a result of the (M+X)LCT character of the transition as has already been described before.<sup>30,102</sup> As a consequence, the symmetry of the compound is reduced which leads to

a localization of the frontier orbitals at one side of the compounds (compare Figure 3.13), in contrast to the situation in the ground state geometry, in which both metal-halide centers and both ligands were involved.

In the triplet state geometry, for both compounds the first excited singlet and triplet state almost completely result from HOMO–LUMO transitions. As these two frontier orbitals have only a small spatial overlap, the energy splittings between the first excited singlet and triplet state are expected to be rather small. From the calculations, values of  $\Delta E(S_1 - T_1) = 760 \text{ cm}^{-1}$  for  $\text{Cu}_2\text{Cl}_2(\text{dppb})_2$  and  $\Delta E(S_1 - T_1) = 1060 \text{ cm}^{-1}$  for  $\text{Ag}_2\text{Cl}_2(\text{dppb})_2$  are found. Although the calculations do not take the environment of the complexes into account (gas phase calculations), the results are in astonishingly good agreement with the experimental values of  $\Delta E(S_1 - T_1) = 600 \text{ cm}^{-1}$  for the Cu(I) and  $\Delta E(S_1 - T_1) = 980 \text{ cm}^{-1}$  for the Ag(I) complex (see below). In the case of the Ag(I) complex, the phosphorus contribution to the HOMO amounts to 35%, whereas for the Cu(I) homologue only 24% are found. As the phosphorus atoms also contribute to the LUMO, a larger spatial HOMO–LUMO overlap and therefore, a larger exchange interaction and a larger singlet-triplet splitting results for  $\text{Ag}_2\text{Cl}_2(\text{dppb})_2$ . Interestingly, also the experimentally observed blue-shift of  $\text{Ag}_2\text{Cl}_2(\text{dppb})_2$  compared to that of  $\text{Cu}_2\text{Cl}_2(\text{dppb})_2$  (compare section 3.2.2) is reflected in the calculations. It can mainly be attributed to a stabilization of the HOMO energy of Ag(I) as compared to the Cu(I) complex.

### 3.2.2 Spectroscopic Discussion

In Figure 3.14, the emission spectra of  $\text{Cu}_2\text{Cl}_2(\text{dppb})_2$  and  $\text{Ag}_2\text{Cl}_2(\text{dppb})_2$  are shown for ambient and for liquid nitrogen temperature. In accordance with the (M+X)LCT character of the emitting state, as predicted by the DFT and TDDFT calculations, the spectra are broad and featureless, even at a temperature of  $T = 1.6 \text{ K}$  (not shown). Compared to the Cu(I) complex, the Ag(I) homologue displays a by 65 nm ( $2500 \text{ cm}^{-1}$ ) blue-shifted emission with a maximum at  $\lambda_{max} = 480 \text{ nm}$  at 300 K. This blue-shifted emission can be rationalized with the second ionization potential of Ag being by 1.2 eV ( $9680 \text{ cm}^{-1}$  higher than that of Cu.<sup>133</sup> As the HOMO is mainly localized on the metal centers, the higher ionization potential results in a stabilization of the HOMO energy and therefore, in an increase of the HOMO–LUMO energy gap. Consequently, the emission of the Ag(I) complex is expected to be blue-shifted compared to the emission of the

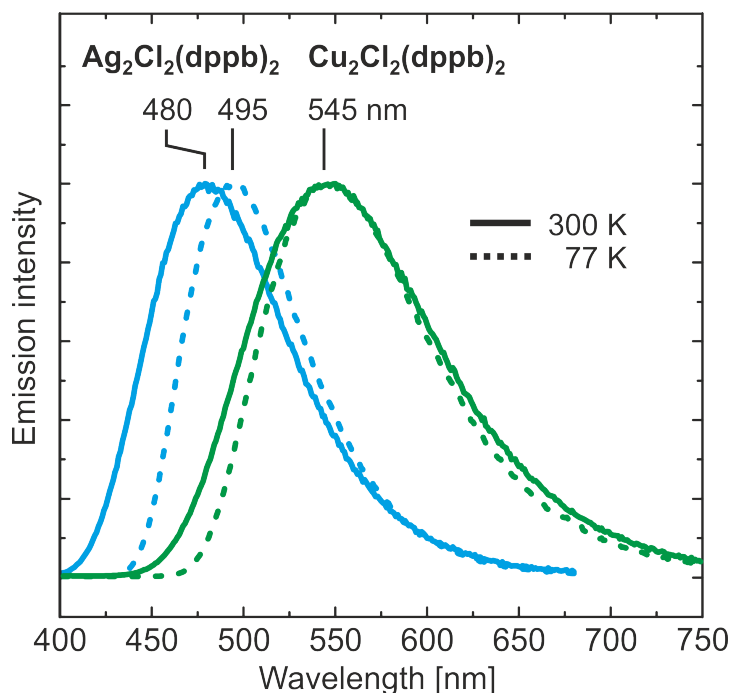


Figure 3.14: Emission spectra of  $\text{Cu}_2\text{Cl}_2(\text{dppb})_2$  and  $\text{Ag}_2\text{Cl}_2(\text{dppb})_2$  powders recorded at 300 K and 77 K. Excitation at  $\lambda_{exc} = 350$  nm

Cu(I) homologue, which matches the experimental observation. This trend is also nicely displayed by the DFT calculations presented in the previous section (compare Figure 3.13).

Similar as the dinuclear copper complexes with aminophosphine ligands discussed in section 3.1, also the diphosphine complexes presented in this section display a pronounced TADF behavior. For  $\text{Ag}_2\text{Cl}_2(\text{dppb})_2$ , a distinct blue-shift of the emission from 495 nm to 480 nm is observed on temperature increase from 77 K to 300 K. This blue-shift is paralleled by a drastic decrease of the emission decay time from 1100  $\mu\text{s}$  to 15  $\mu\text{s}$  while the emission quantum yield does not change significantly in this temperature range (compare Table 3.5). Consequently, the radiative rate increases from  $k_r(77\text{ K}) = 8.7 \times 10^2\text{ s}^{-1}$  to  $k_r(300\text{ K}) = 6.2 \times 10^4\text{ s}^{-1}$ , which is by more than a factor of 70. Such a large increase of the radiative rate on heating clearly indicates that the emission at ambient temperature represents a TADF. For  $\text{Cu}_2\text{Cl}_2(\text{dppb})_2$  an even larger increase of the radiative rate by a factor of more than 490 is found on heating from  $T = 77\text{ K}$  to 300 K (compare Table 3.5). However, the spectral shift on heating is not as obvious as for the Ag homologue. This is a consequence of thermal broadening effects that occur on heating which can

Table 3.5: Photophysical data of  $\text{Ag}_2\text{Cl}_2(\text{dppb})_2$  and  $\text{Cu}_2\text{Cl}_2(\text{dppb})_2$  powders. The energy separations  $\Delta E(\text{S}_1 - \text{T}_1)$  between the lowest excited triplet  $\text{T}_1$  and singlet  $\text{S}_1$  state as well as the decay times of  $\tau(\text{S}_1)$  result from fits according to equation 3.1 (see also Figure 3.15).

Powder	$\text{Ag}_2\text{Cl}_2(\text{dppb})_2$	$\text{Cu}_2\text{Cl}_2(\text{dppb})_2$
$\lambda_{max}(300\text{ K})$	480 nm	545 nm
$\lambda_{max}(77\text{ K})$	495 nm	545 nm
$\Phi_{PL}(300\text{ K})$	93 %	35 %
$\Phi_{PL}(77\text{ K})$	96 %	52 %
$\Delta E(\text{S}_1 - \text{T}_1)$	$980\text{ cm}^{-1}$	$600\text{ cm}^{-1}$
$\tau(\text{T}_1)(77\text{ K})$	1100 $\mu\text{s}$	2200 $\mu\text{s}$
$\tau(\text{S}_1)$	45 ns	70 ns
$\tau(\text{TADF})(300\text{ K})$	15 $\mu\text{s}$	3 $\mu\text{s}$
$k_r(300\text{ K})$	$6.2 \times 10^4\text{ s}^{-1}$	$11.7 \times 10^4\text{ s}^{-1}$
$k_r(77\text{ K})$	$8.7 \times 10^2\text{ s}^{-1}$	$2.4 \times 10^2\text{ s}^{-1}$
$k_r(300\text{ K})/k_r(77\text{ K})$	70	490

mask shifts of the emission energy caused by a TADF, especially if the energy separation  $\Delta E(\text{S}_1 - \text{T}_1)$  is small. Thus, instead of using the temperature induced spectral shift, it is helpful to use a more precise approach for determining the activation energy for the TADF process based on investigating the emission decay time as function of temperature.

In the following, the discussion will mainly focus on the  $\text{Ag}(\text{I})$  complex as silver compounds have been much less explored so far, especially with respect to their TADF properties. The emission decay behavior of this compound for the temperature range between 30 K and 300 K is displayed in Figure 3.15. At temperatures below about 100 K the decay time is essentially constant amounting to 1100  $\mu\text{s}$ . With increasing temperature, the decay time decreases drastically. At ambient temperature, it amounts to only 15  $\mu\text{s}$  which is almost two orders of magnitude shorter than at  $T = 30\text{ K}$ . This clearly shows that at ambient temperature a different electronic state dominates the emission behavior compared to low temperature. This state can be assigned to be the lowest excited singlet state  $\text{S}_1$ . From the monoexponentiality of the decays in the entire temperature range it can be concluded that the states involved in the emission process are in a thermal equilibrium. Therefore, it is justified to use equation 3.1 to fit the data points displayed

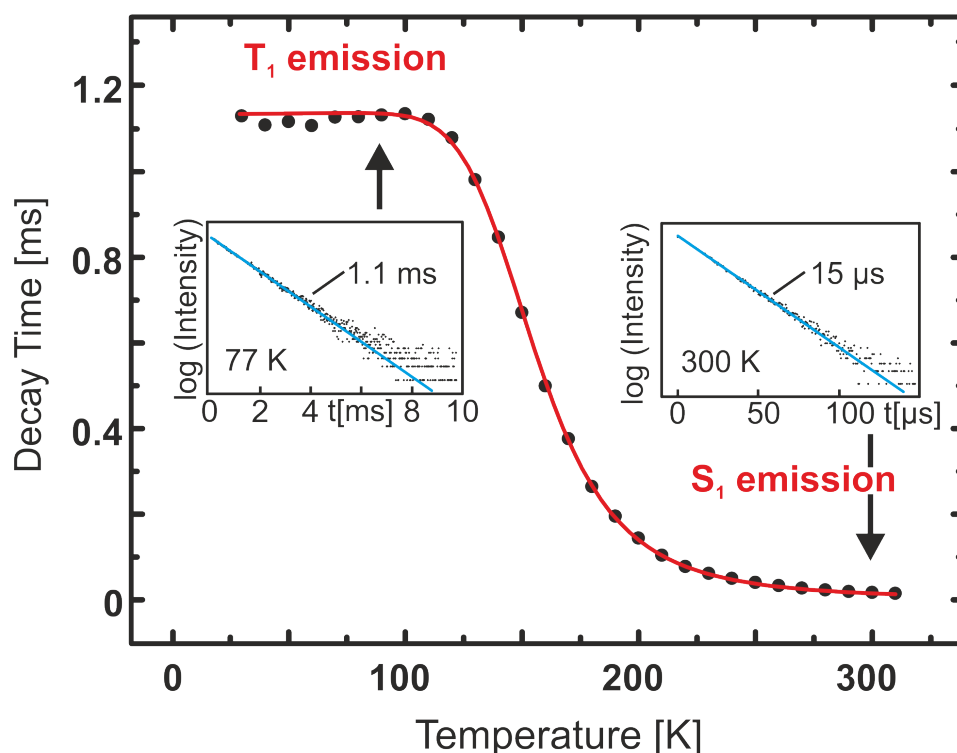


Figure 3.15: Emission decay time of  $\text{Ag}_2\text{Cl}_2(\text{dppb})_2$  powder versus temperature. The insets show the monoexponential decays at 77 K and 300 K, respectively.  $\lambda_{exc} = 378 \text{ nm}$ ,  $\lambda_{det} = 480 \text{ nm}$ . The curve connecting the data points represents a fit according to equation 3.1. The resulting fit parameters are summarized in Table 3.5.

in Figure 3.15. From this procedure, values for the decay times of the singlet  $S_1$  and triplet  $T_1$  states are obtained as well as the energy separation  $\Delta E(S_1 - T_1)$  of these states. They amount to  $\tau(S_1) = 45 \text{ ns}$ ,  $\tau(T_1) = 1100 \mu\text{s}$ , and  $\Delta E(S_1 - T_1) = 980 \text{ cm}^{-1}$ . It is remarked that a prompt fluorescence could not be observed for this compound. Similar measurements were also performed for the Cu(I) complex. The results are summarized in Table 3.5.

### 3.2.3 Comparative Discussion and Conclusion

In this section, a detailed photophysical investigation of the two complexes  $\text{Ag}_2\text{Cl}_2(\text{dppb})_2$  and  $\text{Cu}_2\text{Cl}_2(\text{dppb})_2$  has been carried out. It has been shown that for both complexes the emission behavior at ambient temperature is dominated by a thermally activated delayed fluorescence. The activation energy for the TADF process could be determined

to  $\Delta E(S_1 - T_1) = 980 \text{ cm}^{-1}$  for the Ag(I) and  $\Delta E(S_1 - T_1) = 600 \text{ cm}^{-1}$  for the Cu(I) complex.

A comparison of the TADF activation energies of the Cu(I) complex with diphosphine ligands presented in this section ( $\text{Cu}_2\text{Cl}_2(\text{dppb})_2$ ) and the corresponding Cu(I) complex with aminophosphine ligands presented in the previous section ( $[\text{Cu}(\mu\text{-Cl})(\text{PNMe}_2)]_2$ ) reveals an interesting trend. In the case of the complexes with diphosphine ligands, the experimentally determined TADF activation energy amounts to  $\Delta E(S_1 - T_1) = 600 \text{ cm}^{-1}$ , whereas for the complex featuring aminophosphine ligands it is about 25 % smaller amounting to  $\Delta E(S_1 - T_1) = 460 \text{ cm}^{-1}$ . This effect can be understood when the HOMO and LUMO compositions of the respective compounds are analyzed. In both cases, the HOMO is mainly located on the metal-halide core, whereas the LUMO is localized on the ligands. However, a significant portion of the HOMO is also located on the phosphorus atoms that coordinate to the two Cu(I) centers. In the case of the complex with diphosphine ligands the P contribution to the HOMO amounts to 24 % (6 % for each P atom). As the P atoms also contribute with 8 % to the LUMO, the largest spatial overlap of HOMO and LUMO is occurring on the P atoms. Importantly, this spatial overlap determines the singlet-triplet energy splitting.

In contrast to this, for the complexes with aminophosphine ligands it is found that the overall contribution of the P atoms to the HOMO is significantly smaller amounting to 12 %. This is simply a consequence of the reduced number of P atoms in these ligands as each P atom still contributes with 6 %. Interestingly, the two nitrogen atoms coordinating to the copper centers only have a negligible contribution ( $< 1 \%$  per nitrogen atom) to the HOMO. The spatial distribution of the LUMO is similar to the one found for the diphosphine complex. It is localized on the ligands, whereby the phosphorus atoms contribute with about 4 % while the nitrogen atoms' contribution is negligible. Thus, for the complexes with aminophosphine ligands a smaller singlet-triplet splitting is expected due to the smaller spatial overlap of HOMO–LUMO on the coordinating phosphorus and nitrogen atoms.

Continuing this thought, a complex featuring diamine ligands should exhibit an even smaller energy separation between singlet and triplet state as the nitrogen atoms coordinating to the Cu(I) centers should neither contribute significantly to the HOMO nor to the LUMO. As a consequence, the spatial overlap of HOMO and LUMO and therefore the energy splitting between the first excited singlet and triplet state should be small. To investigate this, a TDDFT calculation was performed for a model compound, which



is based on  $\text{Cu}_2\text{Cl}_2(\text{dppb})_2$  but all phosphorus atoms have been replaced by nitrogen. For this compound, the calculations predict a significantly smaller singlet triplet energy separation of less than  $100 \text{ cm}^{-1}$ .

This raises an interesting question: In order to reduce the overall TADF decay time at ambient temperature, is it sufficient to only reduce the energy splitting of the first excited singlet and triplet state? To answer this question it is helpful to have a closer look at equation 3.1. At first sight, a natural limit for the overall emission decay time is given when  $\Delta E(\text{S}_1 - \text{T}_1) = 0$ . In this case, and under the assumption that  $\tau(\text{T}_1) \gg \tau(\text{S}_1)$ , the equation simplifies to:

$$\tau(\text{T}) = \frac{3 + \exp\left[-\frac{\Delta E(\text{S}_1 - \text{T}_1)}{k_B T}\right]}{3 \tau(\text{T}_1)^{-1} + \tau(\text{S}_1)^{-1} \exp\left[-\frac{\Delta E(\text{S}_1 - \text{T}_1)}{k_B T}\right]} = 4 \tau(\text{S}_1) \quad (3.7)$$

Consequently, a lower limit for the overall emission decay time is given by four times the singlet decay time. For Cu(I) complexes, singlet decay times lying between about 30 ns and 210 ns have been reported (compare for example references 28, 32, 33, 35, 42 and the complexes presented in this chapter), which would limit the overall emission decay times to values between 120 ns and 840 ns. This would be shorter compared to conventional triplet emitters based on iridium and platinum which typically exhibit phosphorescence decay times in the microsecond range.<sup>5,6</sup>

However, in the approach above it is neglected that there is a correlation between the energy separation of the first excited singlet and triplet state  $\Delta E(\text{S}_1 - \text{T}_1)$  and the decay time of the first excited singlet state  $\tau(\text{S}_1)$ . Both quantities are determined by the spatial overlap of HOMO and LUMO.<sup>iv</sup> A small spatial overlap of these frontier orbitals results in a small exchange interaction and therefore a small singlet triplet splitting. However, a small spatial overlap of HOMO and LUMO also reduces the allowedness of the  $\text{S}_1 \rightarrow \text{S}_0$  transition resulting in longer decay times  $\tau(\text{S}_1)$  of the  $\text{S}_1$  state. This trend is clearly displayed by the experimental data obtained for the complexes presented in this chapter and a graphical representation of this correlation is given in Figure 3.16.

For the following considerations it is helpful to define an analytical function that correlates the experimentally found singlet decay times  $\tau(\text{S}_1)$  with the experimentally

<sup>iv</sup>For this consideration it is assumed that the first excited singlet and triplet state result from the HOMO-LUMO transition.

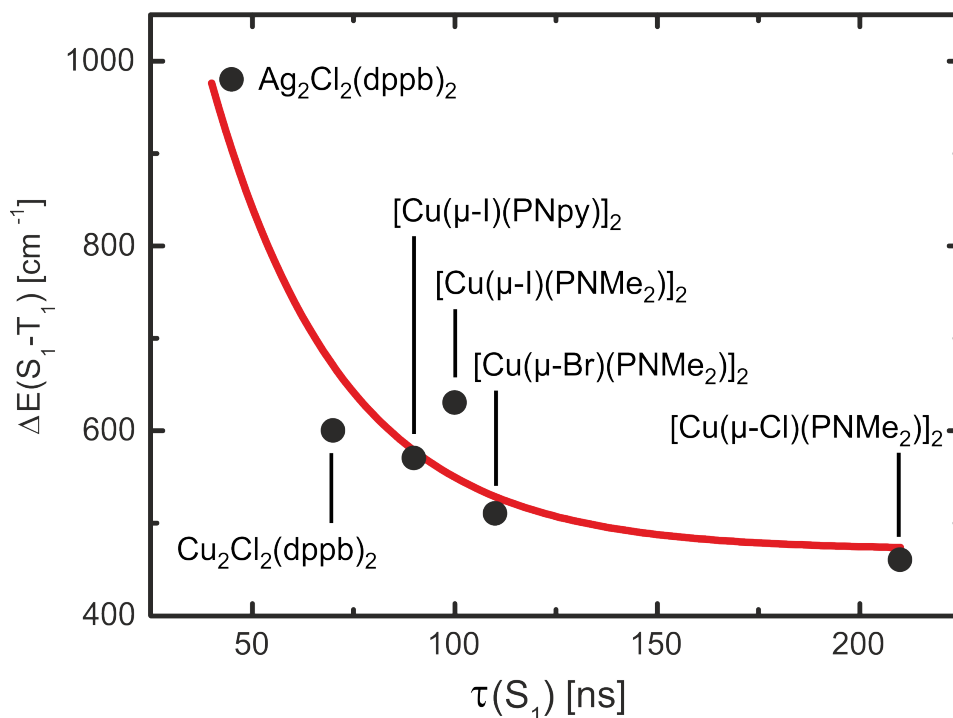


Figure 3.16: Emission decay time of the singlet state  $S_1$  versus energy separation of the first excited singlet and triplet state  $\Delta E(S_1 - T_1)$ . Data are given for the compounds presented in this chapter. The red line represents a fit of the data with a single exponential function.

determined singlet triplet energy separation  $\Delta E(S_1 - T_1)$ . It turns out that the data points in Figure 3.16 can be adequately fitted by a single exponential function:

$$\Delta E(S_1 - T_1)(\tau(S_1)) = y_0 + A \exp \left[ -\frac{\tau(S_1)}{\tau_0} \right] \quad (3.8)$$

It is strongly emphasized that this function is not derived from physical arguments but is only used to simplify the following discussion. From the fitting procedure the free parameters could be determined to  $y_0 = 470 \text{ cm}^{-1}$ ,  $A = 1750 \text{ cm}^{-1}$ , and  $\tau_0 = 33 \text{ ns}$ . Plugging equation 3.8 with the respective parameters into equation 3.1 and assuming

that  $\tau(T_1) \gg \tau(S_1)$  gives:

$$\begin{aligned}
 \tau(\tau(S_1)) &= \frac{3 + \exp\left[-\frac{\Delta E(\Delta E(S_1-T_1))}{k_B T}\right]}{3 \tau(T_1)^{-1} + \tau(S_1)^{-1} \exp\left[-\frac{\Delta E(\Delta E(S_1-T_1))}{k_B T}\right]} \\
 &\approx \frac{3 + \exp\left[-\frac{\Delta E(S_1-T_1)}{k_B T}\right]}{\tau(S_1)^{-1} \exp\left[-\frac{\Delta E(\Delta E(S_1-T_1))}{k_B T}\right]} \\
 &= \tau(S_1) \left[ 3 \exp\left[\frac{\Delta E(S_1 - T_1)}{k_B T}\right] + 1 \right] \\
 &= \tau(S_1) \left[ 3 \exp\left[\frac{y_0 + A \exp\left[-\frac{\tau(S_1)}{\tau_0}\right]}{k_B T}\right] + 1 \right] \\
 &= \tau(S_1) \left[ 3 \exp\left[\frac{470 \text{ cm}^{-1} + 1750 \text{ cm}^{-1} \exp\left[-\frac{\tau(S_1)}{33 \text{ ns}}\right]}{k_B T}\right] + 1 \right]
 \end{aligned} \tag{3.9}$$

In this way, an equation is obtained that gives a lower limit for the emission decay time  $\tau$  in dependence of the singlet decay time  $\tau(S_1)$  and therefore, via equation 3.9 also in dependence of  $\Delta E(S_1 - T_1)$ . In Figure 3.17, a graphical representation of equation 3.9 is shown for  $T = 300 \text{ K}$ . Interestingly, the graph exhibits a minimum for a singlet decay time of about  $\tau(S_1) = 110 \text{ ns}$  which corresponds to a singlet triplet energy splitting of  $\Delta E(S_1 - T_1) = 535 \text{ cm}^{-1}$ . Accordingly, for these values of  $\tau(S_1)$  and  $\Delta E(S_1 - T_1)$ , respectively, the overall TADF emission decay time  $\tau$  is minimal and amounts to  $\tau_{min} = 4.5 \mu\text{s}$ . This value seems to represent a fundamental lower limit that cannot be exceeded if only emission according to a TADF mechanism is considered. This result is also in agreement with the literature as until now no (radiative) emission decay times shorter than about  $4.5 \mu\text{s}$  have been reported.

However, in all consideration above it was assumed that the  $3 \tau(T_1)^{-1}$  term in equation 3.1 can be neglected. This approximation is justified for all complexes presented in this chapter due to their long triplet decay times. In section 4.2, however, a class of Cu(I) complexes is presented, of which the triplet decay times are orders of magnitude shorter. For these compounds, the triplet decay time has to be taken into account when calculating the lower limit of the overall emission decay time. Therefore, by providing an additional effective radiative decay path via the  $T_1 \rightarrow S_0$  transition a reduction of the

overall emission decay time to values lower than  $4.5 \mu\text{s}$  could be achieved.

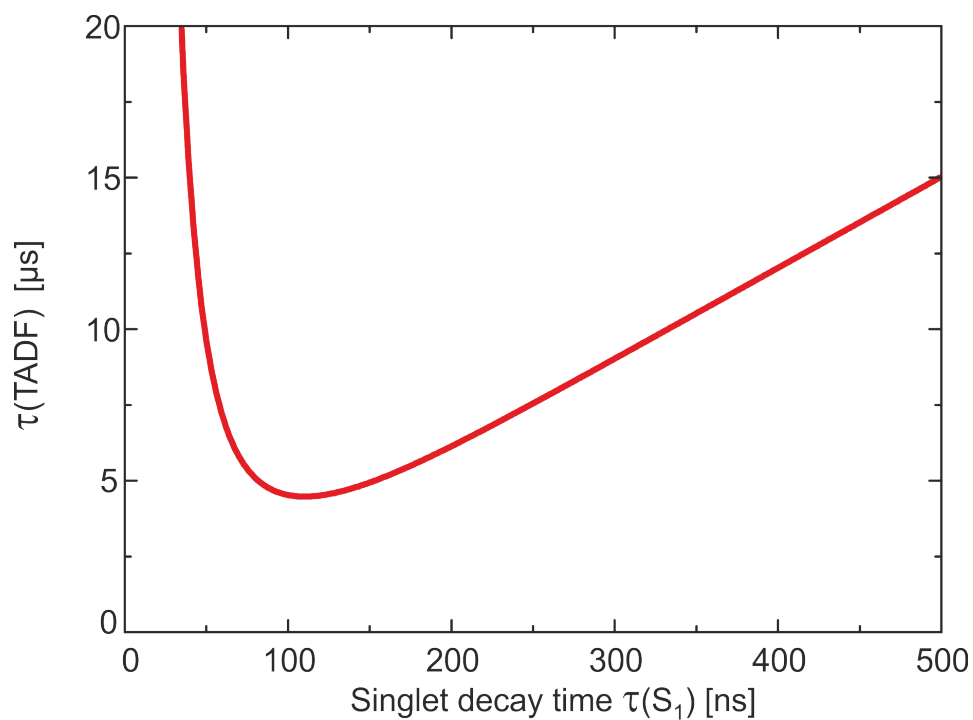


Figure 3.17: Overall emission decay time  $\tau$  versus decay time of the singlet state  $\tau(\text{S}_1)$  according to equation 3.9 for  $T = 300$  K

## Mononuclear Copper Complexes

### 4.1 Cu(I) Complexes with two Bidentate Ligands

In the last years, Cu(I) complexes have been intensely studied as their potential as low-cost emitters for the application in electroluminescent devices was recognized. Hereby, Cu(I) compounds that are pseudo-tetrahedrally coordinated by two bidentate ligands have been in the focus of research.<sup>5,6,33,35,42,78,86,95-97,134-137</sup> However, on excitation these compounds can undergo a formal (partial) oxidation from Cu(I) to Cu(II) due to the pronounced metal-to-ligand charge transfer (MLCT) character of the transition.<sup>5,6,13,30,32-38,40,42,52,68,85,86,95-97,134-139</sup> As a consequence, a geometry distortion from the pseudo-tetrahedral to a more planar coordination geometry occurs.<sup>5,30,33,35,90,91,93,94,96,97,110</sup> Such distortions typically result in strong non-radiative deactivation to the ground state. An approach to address this problem is the use of sterically demanding ligands that largely suppress flattening distortions. This concept has been successfully applied before for other Cu(I) complexes.<sup>33,35</sup> In this chapter, the two charged Cu(I) complexes [Cu(POP)(dmbpy)][BF<sub>4</sub>] (**1**) and [Cu(POP)(tmbpy)][BF<sub>4</sub>] (**2**) (dmbpy = 4,4'-dimethyl-2,2'-bipyridine; tmbpy = 4,4',6,6'-tetramethyl-2,2'-bipyridine; POP = bis[2-(diphenylphosphino)-phenyl]ether) are investigated. Their chemical structures are displayed in Figure 4.1. Both compounds consist of a bipyridine and a biphosphine ligand coordinated tetrahedrally to a Cu(I) center. In contrast to complex **1**, complex **2** possesses an additional pair of methyl groups at the 6,6' positions of the bipyridine ligand which introduces a strong sterical interaction with the POP ligand. As a result, flattening distortions on excitation are largely suppressed and the emission quantum yield is significantly increased (compare Figure 4.1). For a better understanding of this effect,



Figure 4.1: Structures of complexes **1** and **2** and their emission in ethanol recorded for similar compound concentrations. Note the striking differences in the brightness.

the complexes were investigated in different media under variation of the temperature. Furthermore, a detailed analysis of the temperature-dependent decay behavior of compound **2** reveals the occurrence of an efficient thermally activated delayed fluorescence (TADF) showing that compound **2** exhibits excellent properties for harvesting all singlet and triplet excitons in the lowest excited singlet state when applied as an emitter in an electroluminescent device (singlet harvesting effect).<sup>5,6,33</sup> It is noted that large parts of this chapter have been previously published in reference 42.

### 4.1.1 Spectroscopic Discussion

In Figure 4.2, the structure of compound **2** as determined from X-ray measurements is displayed.<sup>1</sup> From this, the slightly perturbed tetrahedral coordination environment around the Cu(I) center is apparent. More specifically, the angle between the N(41)–Cu–N(49) and the P(2)–Cu–P(28) plane amounts to  $82^\circ$  which only slightly deviates from the  $90^\circ$  of an ideal tetrahedron. Furthermore, also the steric blocking that is responsible for restricting the flattening distortion on excitation becomes obvious. Mainly, it can be attributed to an interaction between the phenyl groups present at the biphosphine ligand and the methyl groups present at the 6,6' positions of the bipyridine ligand. An overview of important bonding distances and angles is given in Table 4.1.

At first, the discussion of the photophysical properties will focus on compound **2**. In Figure 4.3, the absorption spectra of this complex and of the coordinating POP ligand recorded in ethanol (EtOH) are shown. In addition, also the absorption spectrum of bpy

<sup>1</sup>X-ray data were provided by Neil Robertson and Charlotte L. Linfoot, University of Edinburgh, GB.

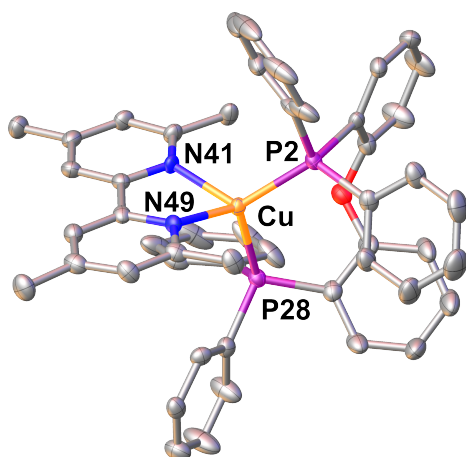


Figure 4.2: X-ray structure of **2** with probability ellipsoids set to 50%. H atoms are omitted for clarity. X-ray data were provided by Neil Robertson and Charlotte L. Linfoot, University of Edinburgh, GB.

(bipyridine) recorded in the same solvent is displayed, as replacement for tmbpy which was not available. However, the absorption spectra of bpy and tmbpy are not expected to deviate significantly.

In the range between about 220 nm and 330 nm an intense absorption band is observed for complex **2**. This band is also present in the spectra of the free ligands, indicating that it originates from ligand centered transitions. However, compared to the free ligands, the absorption band of the complex displays a slight red-shift which is likely a consequence of metalation. In contrast, between 330 nm and 450 nm the free ligands do not show an absorption but an absorption band for the complex is observed. Therefore, this band can be assigned to result from metal-to-ligand charge transfer (MLCT) transitions.

This assignment is supported by DFT and TDDFT calculations which show that the HOMO is mainly located on the copper center, whereas the LUMO is located on the bipyridine ligand (compare Figure 4.4) and that transitions between these frontier orbitals determine the lowest excited singlet and triplet state.

At ambient temperature, the powder exhibits yellow luminescence under UV light. The corresponding emission spectrum is broad and featureless, being in agreement with the charge-transfer character of the transition. The spectrum exhibits a peak at  $\lambda_{max} = 555$  nm, and the emission decay time amounts to  $\tau = 11$   $\mu$ s. Most notably, the compound's emission quantum yield is observed as  $\Phi_{PL} = 55$  %.

Interestingly, the emission quantum yield can be further increased by grinding the

Table 4.1: Selected bond lengths and bond angles for compound **2** as received from single crystal X-ray crystallography measurements and from DFT calculations performed on the B3LYP/def2-SVP level of theory. X-ray data were provided by Neil Robertson and Charlotte L. Linfoot, University of Edinburgh.

compound <b>2</b>	X-ray	DFT
Cu–N(41) [Å]	2.089(3)	2.170
Cu–N(49) [Å]	2.097(3)	2.172
Cu–P(2) [Å]	2.2518(11)	2.371
Cu–P(28) [Å]	2.2901(11)	2.379
N(41)–Cu–N(49) [°]	79.64(13)	78.09
N(41)–Cu–P(2) [°]	121.85(9)	117.74
N(49)–Cu–P(2) [°]	117.03(10)	113.04
N(41)–Cu–P(28) [°]	103.50(10)	108.40
N(49)–Cu–P(28) [°]	114.35(9)	121.73
P(2)–Cu–P(28) [°]	115.25(4)	113.35

substance, for example between two glass plates. After this procedure, a quantum yield of  $\Phi_{PL} = 74\%$  is obtained for the ground powder. In contrast to this, the quantum yield decreases to  $\Phi_{PL} = 39\%$ , when the powder is compressed by applying a pressure of  $6000 \text{ kg cm}^{-2}$  for approximately 20 minutes.<sup>ii</sup> This displays an interesting trend as the emission quantum yield seems to be correlated to the grain size of the powder. More precisely, a small grain size is correlated with a high quantum yield and vice versa. This trend is also represented for the radiative  $k_r$  and non-radiative rates  $k_{nr}$  which de- and increase, respectively, with growing grain size (compare Table 4.2). Furthermore, from Figure 4.5(b) it can be seen that also the emission energies are influenced by mechanical manipulations which results in a red-shift of the emission from  $\lambda_{max} = 555 \text{ nm}$  to  $\lambda_{max} = 565 \text{ nm}$  after compression. A rationalization for this behavior can be given when powder diffraction data are analyzed for the freshly synthesized and the compressed sample (Figure 4.5(a)). Clearly, it can be seen that after compression more peaks appear in the diffraction pattern indicating an increase of the the samples crystallinity. Such changes in the morphology can result in drastic changes of the emission properties, which

<sup>ii</sup>Compression performed by Sebastian Maderlehner, University of Regensburg



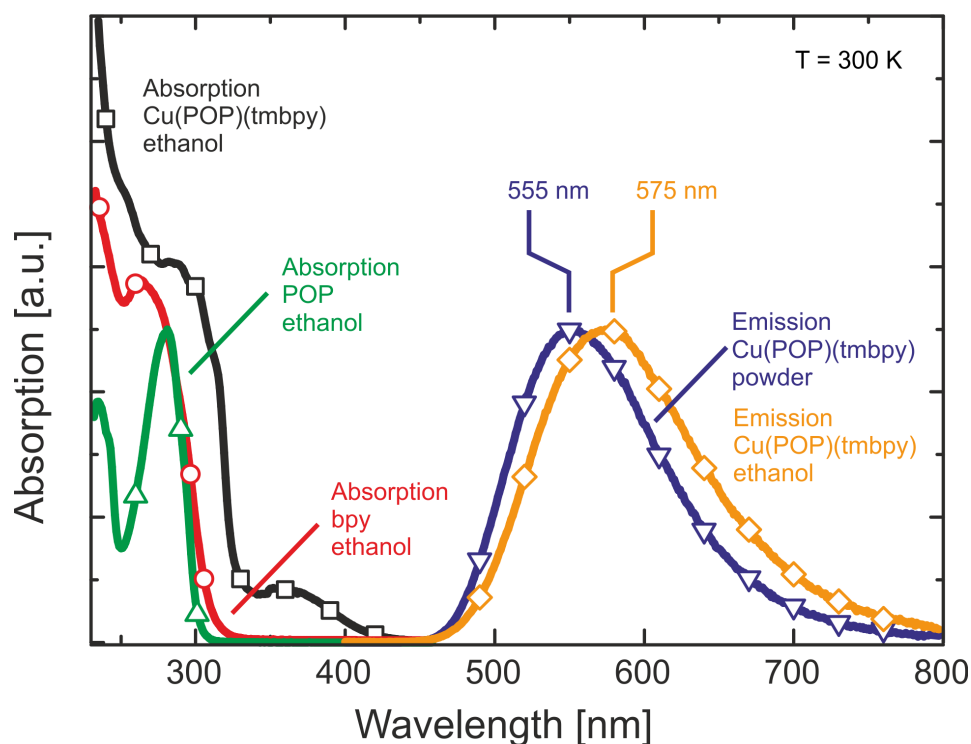


Figure 4.3: Absorption spectra of the complex  $[\text{Cu}(\text{POP})(\text{tmbpy})][\text{BF}_4]$  and of the ligands POP and bpy recorded in EtOH. Emission spectra are displayed for  $[\text{Cu}(\text{POP})(\text{tmbpy})][\text{BF}_4]$  as powder and in an EtOH solution. All spectra were recorded at ambient conditions.

has recently been shown for other Cu(I) compounds.<sup>140–142</sup> In the following, only the data for the untreated powder samples as received from synthesis will be discussed.

When compound **2** is dissolved in ethanol (EtOH), the emission is red-shifted ( $\lambda_{max} = 575 \text{ nm}$ ) compared to the powder ( $\lambda_{max} = 555 \text{ nm}$ ). In addition, the quantum yield decreases significantly from  $\Phi_{PL}(\text{powder}) = 55\%$  to  $\Phi_{PL}(\text{EtOH}) = 6\%$ . Also, the emission decay time decreases from  $\tau(\text{powder}) = 11 \mu\text{s}$  to  $\tau(\text{EtOH}) = 2.5 \mu\text{s}$ . Such a behavior has been reported also for other Cu(I) compounds in the literature and can be rationalized with the pronounced metal-to-ligand charge transfer (MLCT) character of the emitting state according to the following model:<sup>33,35</sup> On excitation, a significant amount of charge is transferred from the metal to a ligand resulting in a formal (partial) oxidation of the metal center from Cu(I) to Cu(II). As a consequence of this, a flattening distortion occurs, as Cu(II) prefers a planar coordination environment, in contrast to the tetrahedral one of Cu(I). Such structural reorganizations are connected with a stabilization of the

Table 4.2: Emission data for complexes **1** and **2** recorded in ethanol, powder, and doped into a polymethylmethacrylate (PMMA) matrix, respectively. For compound **2**, data are given for the powder as received from synthesis, after grinding, and after compression. For compound **1**, no obvious differences in the emission behavior were observed after mechanical manipulations.

	Temp.	[Cu(POP)(dmbpy)] <sup>+</sup> 1	[Cu(POP)(tmbpy)] <sup>+</sup> 2		
<b>EtOH</b>					
$\lambda_{max}$ [nm]	300 K	655		575	
$\tau$ [ $\mu$ s]	300 K	0.02		2.5	
$\Phi_{PL}$ [%]	300 K	< 1		6	
$k_r$ [ $10^4$ s <sup>-1</sup> ]	300 K			2.4	
$k_{nr}$ [ $10^4$ s <sup>-1</sup> ]	300 K			38	
$\lambda_{max}$ [nm]	77 K	605		535	
$\tau$ [ $\mu$ s]	77 K	16 <sup>a</sup>		73	
<b>Powder</b>					
$\lambda_{max}$ [nm]	300 K	575	555 <sup>b</sup>	555 <sup>c</sup>	565 <sup>d</sup>
$\tau$ [ $\mu$ s]	300 K	— <sup>e</sup>	11 <sup>b</sup>	13 <sup>c</sup>	11 <sup>d</sup>
$\Phi_{PL}$ [%]	300 K	9	55 <sup>b</sup>	74 <sup>c</sup>	39 <sup>d</sup>
$k_r$ [ $10^4$ s <sup>-1</sup> ]	300 K		5.0 <sup>b</sup>	5.7 <sup>c</sup>	3.5 <sup>d</sup>
$k_{nr}$ [ $10^4$ s <sup>-1</sup> ]	300 K		4.1 <sup>b</sup>	2.0 <sup>c</sup>	5.5 <sup>d</sup>
$\lambda_{max}$ [nm]	77 K	595	575 <sup>b</sup>		
$\tau$ [ $\mu$ s]	77 K	— <sup>e</sup>	87 <sup>b</sup>		
$\Phi_{PL}$ [%]	77 K		47 <sup>b</sup>		
$k_r$ [ $10^4$ s <sup>-1</sup> ]	77 K		0.5 <sup>b</sup>		
$k_{nr}$ [ $10^4$ s <sup>-1</sup> ]	77 K		0.6 <sup>b</sup>		
<b>PMMA</b>					
$\lambda_{max}$ [nm]	300 K	565		525	
$\tau$ [ $\mu$ s]	300 K	— <sup>e</sup>		— <sup>e</sup>	
$\Phi_{PL}$ [%]	300 K	6		64	

<sup>a</sup> Slightly deviating from monoexponential decay.

<sup>b</sup> Data refer to measurements on powder as received from synthesis.

<sup>c</sup> Data refer to measurements on powder after grinding.

<sup>d</sup> Data refer to measurements on powder after compression.

<sup>e</sup> Strongly non monoexponential decay.

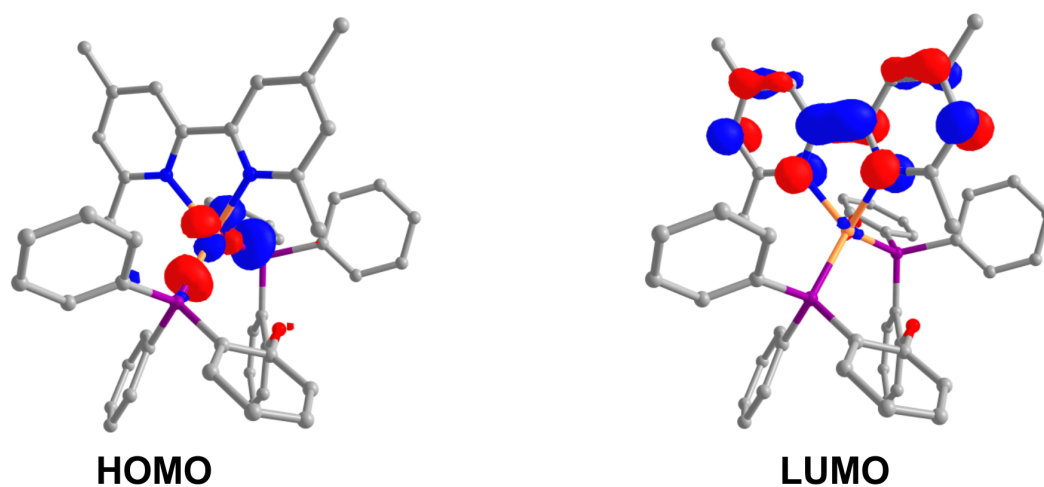


Figure 4.4: HOMO and LUMO of  $\text{Cu}(\text{POP})(\text{tmbpy})^+$  (**2**). Calculations performed on the B3LYP/def2-SVP level of theory.

emitting state and therefore with a red-shift of the emission energy. Hereby, the tendency of such major structural reorganizations to occur is especially pronounced in nonrigid environments. Accordingly, the emission is expected to be red-shifted in solution compared to the more rigid powder environment. This is in agreement with the experimental observations. Furthermore, structural reorganizations are expected to open a highly effective nonradiative relaxation channel due to increased Franck-Condon factors of the excited and the ground state.<sup>63</sup> As a result of the increase of the non-radiative deactivation rate, the emission quantum yield and the emission decay time are reduced in less rigid environments. Also this trend is observed experimentally. It is mentioned that cooling the ethanol solution to  $T = 77 \text{ K}$  leads to a rigid cage around the complex through freezing of the solvent. This prevents distinct geometry changes upon excitation. As a consequence, the emission spectrum is blue-shifted from  $\lambda_{max}(300 \text{ K}) = 575 \text{ nm}$  to  $\lambda_{max}(77 \text{ K}) = 535 \text{ nm}$ . Interestingly, when compound **2** is doped into a polymethylmethacrylate (PMMA) matrix, the emission is blue-shifted ( $\lambda_{max}(\text{PMMA}) = 525 \text{ nm}$ ) compared to that of the powder ( $\lambda_{max}(\text{powder}) = 555 \text{ nm}$ ). In addition, the emission quantum yield increases from  $\Phi_{PL}(\text{powder}) = 55 \%$  to  $\Phi_{PL}(\text{PMMA}) = 64 \%$ . At first sight this seems counterintuitive as a polymer matrix should provide a less rigid environment than the neat powder.<sup>5,33,35,37</sup> However, for this specific compound this might not be the case, rather it seems that the PMMA matrix provides more rigidity of the direct environment which is reflected in the blue-shifted emission and the increased emission quantum yield.

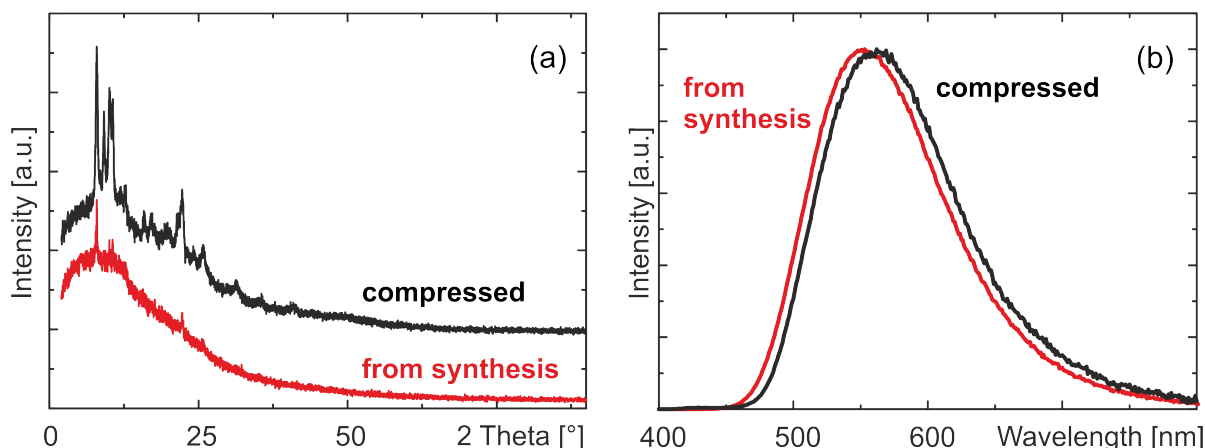


Figure 4.5: (a) Powder diffraction pattern recorded for the sample as received from synthesis (red) and after compression (black). (b) Emission spectra recorded before and after compression. Diffraction measurements were performed by Sebastian Maderlehner, University of Regensburg.

In the powder phase, the emission of compound **2** ( $\lambda_{max} = 555$  nm) is blue-shifted compared to compound **1** ( $\lambda_{max} = 575$  nm). Also, compound **2** exhibits a significantly higher emission quantum yield of  $\Phi_{PL} = 55\%$  compared to the value of  $\Phi_{PL} = 9\%$  found for compound **1**. These trends are also displayed for the complexes dissolved in EtOH solution and doped into a PMMA matrix, respectively (compare Table 4.2). Mainly, the higher quantum yield of compound **2** can be attributed to the 6,6'-methyl groups present on the bipyridine ligand. These groups act to sterically limit the flattening distortion on excitation thus preventing an effective nonradiative deactivation to the ground state. In compound **1** these groups are not present explaining its lower quantum yield. Furthermore, as discussed above, a flattening distortion results in a red-shift of the emission. Accordingly, the emission of **1** is expected to be red-shifted compared to **2**. Indeed, this is experimentally observed.

It is noted that also the electron donating character of the methyl groups has an influence on the emission energy. However, in the absorption spectra only a slight red-shift of the MLCT absorption band of compound **1** compared to **2** is observed. In emission, a similarly small energy shift would be expected. However, the observed energy shift in emission is significantly larger and therefore cannot be rationalized by the electron donating effect of the methyl groups. An overview of the emission parameters of compounds **1** and **2** is given in Table 4.2.

### 4.1.2 Temperature Dependent Measurements

For a more detailed understanding, the emission behavior of compound **2** (powder) was investigated under variation of temperature (Figures 4.6 and 4.7). At  $T = 77$  K, the emission decay time amounts to 87  $\mu$ s and is therefore assigned to be a phosphorescence originating from the lowest excited triplet state  $T_1$ . With increasing temperature, the decay time decreases drastically to 11  $\mu$ s at ambient temperature while the quantum yield does not change significantly between liquid nitrogen and ambient temperature ( $\Phi_{PL}(300\text{ K}) = 55\%$ ,  $\Phi_{PL}(77\text{ K}) = 47\%$ ). With this, the radiative rates can be calculated according to  $k_r = \Phi_{PL} \tau^{-1}$ . They amount to  $k_r(77\text{ K}) = 5.4 \times 10^3\text{ s}^{-1}$  and  $k_r(300\text{ K}) = 5.0 \times 10^4\text{ s}^{-1}$ , i. e. a pronounced increase of the radiative rate by almost a factor of 10 occurs on heating. This very strong increase is paralleled by a blue-shift of the emission from 575 nm to 555 nm (peak to peak, compare Figure 4.6). Both effects, the increase of the radiative rate and the blue-shift of the emission can be rationalized by a thermal population of the energetically higher lying singlet state  $S_1$  from the triplet state  $T_1$  (Figure 4.7, inset). Such an emission mechanism corresponds to a thermally activated delayed fluorescence (TADF). The energy separation between the first excited singlet and triplet state  $\Delta E(S_1 - T_1)$  can be estimated from the shift of the emission spectra from 77 K to 300 K, giving  $\Delta E(S_1 - T_1) = 630\text{ cm}^{-1}$  (Figure 4.6). A more accurate approach to determine this energy separation results from measuring the change of the emission decay time as a function of temperature (Figure 4.7) according to equation 4.1.<sup>5,6,28,89,143</sup>

$$\tau(T) = \frac{3 + \exp\left[-\frac{\Delta E(S_1 - T_1)}{k_B T}\right]}{3 \tau(T_1)^{-1} + \tau(S_1)^{-1} \exp\left[-\frac{\Delta E(S_1 - T_1)}{k_B T}\right]} \quad (4.1)$$

In this equation,  $\Delta E(S_1 - T_1)$  represents the energy separation between the first excited singlet and triplet state,  $\tau(S_1)$  and  $\tau(T_1)$  are the emission decay times of the first excited singlet and triplet state, respectively, and  $k_B$  the Boltzmann constant. From the fitting procedure, a value of  $\Delta E(S_1 - T_1) = 720\text{ cm}^{-1}$  results. This matches well the value obtained from the spectral shift. For the decay time of the first excited singlet state, a value of  $\tau(S_1) = 160\text{ ns}$  was found. Such a value is in agreement with the singlet nature of the of this state, however, being connected with a low oscillator strength of the  $S_1 \leftrightarrow S_0$  transition. An emission originating as a prompt fluorescence was not found,

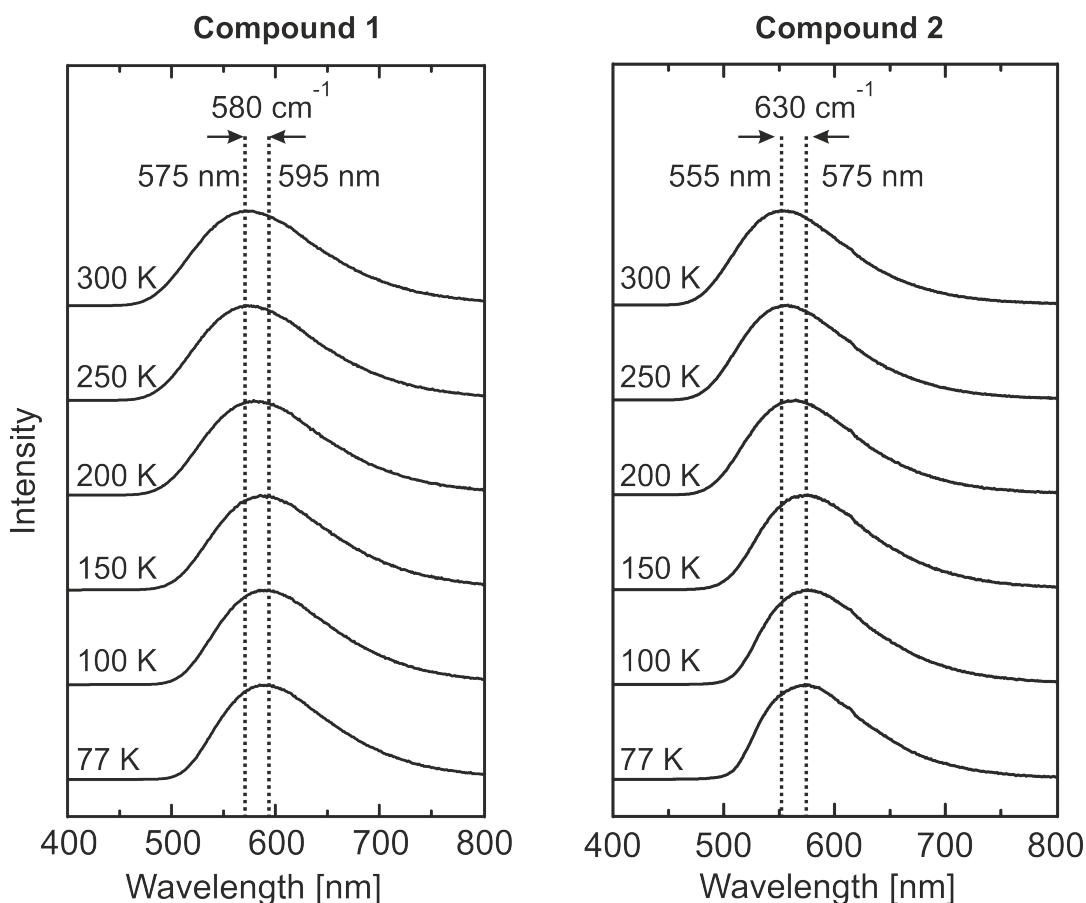


Figure 4.6: Emission spectra of  $[\text{Cu}(\text{POP})(\text{dmbyp})][\text{BF}_4]$  (**1**) and  $[\text{Cu}(\text{POP})(\text{tmbyp})][\text{BF}_4]$  (**2**) at different temperatures. The samples were excited at  $\lambda_{exc} = 350 \text{ nm}$ .

presumably due to the significantly faster intersystem crossing process between the  $S_1$  and  $T_1$  state.<sup>79,86,87</sup> Moreover, the value found for  $\tau(T_1) = 84 \mu\text{s}$  supports the assignment of a triplet state emission. It is noted that equation 4.1 can only be applied if the emitting states are in a thermal equilibrium. In the temperature range between 77 K and 300 K, this condition is fulfilled.

For completeness it is mentioned that for compound **1** a determination of the energy splitting  $\Delta E(S_1 - T_1)$  by measuring the emission decay time in dependence of the temperature could not be performed due to the large nonradiative contribution to the decay time. However, from the shift of the emission energy from  $T = 77 \text{ K}$  to 300 K the splitting can be estimated to amount to  $\Delta E(S_1 - T_1) = 580 \text{ cm}^{-1}$  (compare Figure 4.6) which is similar to the splitting found for compound **2**.

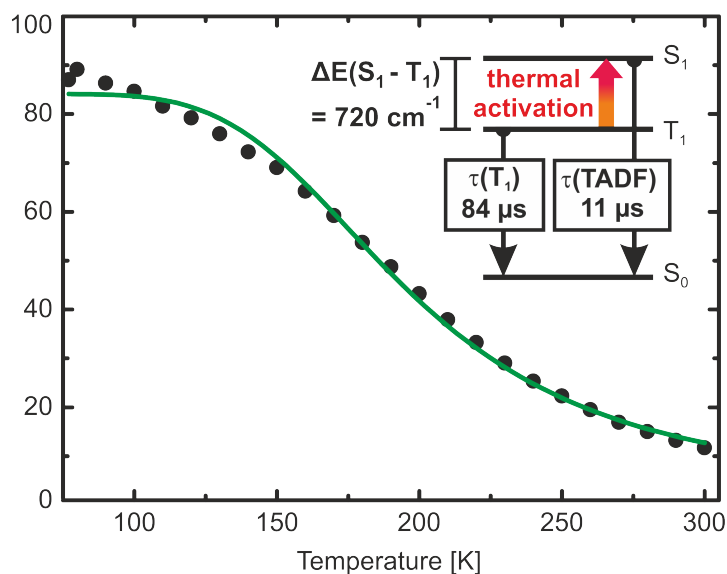


Figure 4.7: Emission decay time of compound **2** (powder) versus temperature. The decay times are close to monoexponential in the whole temperature range. The solid curve represents a fit according to equation 4.1. The parameters obtained from the fitting procedure amount to  $\Delta E(S_1 - T_1) = 720 \text{ cm}^{-1}$ ,  $\tau(T_1) = 84 \text{ }\mu\text{s}$ , and  $\tau(S_1) = 160 \text{ ns}$ .

### 4.1.3 Conclusion

In this section it was demonstrated how a slight modification of the chemical structure of a  $[\text{Cu}^{\text{I}}(\text{diimine})(\text{diphosphine})]^+$  can lead to a substantial increase of the emission quantum yield. In the case of the  $[\text{Cu}(\text{POP})(\text{dmbpy})]^+$  complex, this is achieved by the increase of the steric demand of the bipyridine ligand through the introduction of two additional methyl groups in the 6,6' positions resulting in the  $[\text{Cu}(\text{POP})(\text{tmbpy})]^+$  complex. In combination with the bulky POP ligand, these groups limit the photoinduced flattening distortion that the compound can undergo on excitation of an MLCT state. As a result, the nonradiative deactivation to the ground state is significantly reduced, leading to around a 6-fold increase of the emission quantum yield from 9% to 55% (or even 74% for the sample after grinding). These observations demonstrate the increased rigidity enforced upon the structure of **2** compared to that present in **1** as a result of the steric demands of the 6,6'-methyl groups on the bipyridyl ligands.

Most interestingly, for the sterically constrained compound **2**, it was found that at ambient temperature the emission is largely determined by a thermally activated delayed fluorescence. At ambient temperature, the compound emits almost only from the

first excited singlet state  $S_1$  ( $^1\text{MLCT}$ ) which is thermally populated from the  $T_1$  state ( $^3\text{MLCT}$ ). This results in a relatively short emission decay time at ambient temperature of 11  $\mu\text{s}$  as compare to the triplet state decay time of 84  $\mu\text{s}$ . This short emission decay time along with the high emission quantum yield and the occurrence of a TADF make compound **2** highly attractive for the use in electroluminescent devices. Recently, efficient light-emitting electrochemical cells utilizing this class of compounds as emitter materials have been demonstrated.<sup>99</sup>



## 4.2 Cu(I) Complexes with Three Coordinations

A crucial parameter that determines the effectiveness of a thermally activated delayed fluorescence in a particular substance is the energy separation between the first excited singlet and triplet state  $\Delta E(S_1 - T_1)$ . If it is larger than about  $3000\text{ cm}^{-1}$ , a thermal population of the singlet state  $S_1$  from the triplet state  $T_1$  is not effective. Therefore, it is important to understand how  $\Delta E(S_1 - T_1)$  can be controlled by properly engineering the chemical structure of an emitter complex. For this, the two structurally related Cu(I) complexes (IPr)Cu(py<sub>2</sub>-BMe<sub>2</sub>) (**1**) and (Bzl-3,5Me)Cu(py<sub>2</sub>-BMe<sub>2</sub>) (**2**) (IPr = 1,3-bis(2,6-diisopropylphenyl)imidazol-2-ylidene, Bzl-3,5Me = 1,3-bis(3,5-dimethylphenyl)-1H-benzo[d]imidazol-2-ylidene, py<sub>2</sub>-BMe<sub>2</sub> = di(2-pyridyl)dimethylborate) have been investigated. The chemical structures are displayed in Table 4.3. Interestingly, compound **1** shows a highly effective TADF (with  $\Delta E(S_1 - T_1) = 740\text{ cm}^{-1}$ ), whereas for compound **2** only phosphorescence but no TADF is observed at ambient temperature. In this section, a detailed photophysical investigation of the two complexes is presented and it is discussed why despite similar chemical structures the photophysical properties of both compounds differ drastically, especially with respect to the value found for  $\Delta E(S_1 - T_1)$ . Large parts of this section have been published previously in reference 39.

### 4.2.1 Ambient Temperature Phosphorescence versus TADF

Under excitation with UV light, the powders of the studied complexes display intense blue (**1**) and yellow (**2**) luminescence at ambient temperature with short emission decay times of 11  $\mu\text{s}$  and 18  $\mu\text{s}$  and remarkably high emission quantum yields of 76 % (**1**) and 73 % (**2**), respectively. In Figure 4.8, the corresponding emission spectra are displayed.

The spectra are broad and featureless with maxima at 475 nm (**1**) and 575 nm (**2**) at 300 K. The shapes of the spectra indicate that the emission originates from a charge transfer state which, in this case, is mainly of metal-to-ligand charge transfer (MLCT) nature. This assumption is in agreement with literature assignments of other Cu(I) compounds.<sup>5,6,13,30,32-38,40,42,52,68,85,86,95-97,134-139</sup> and is further substantiated by results of DFT and TDDFT calculations presented in reference 68 and below. The emission of **2** is found at significantly lower energy than that of compound **1**. This can be rationalized by the expansion of the  $\pi$ -system of the IPr ligand (compound **2**) which leads to a lower lying LUMO energy than that of the Bzl-3,5Me ligand, whereas the HOMO of both

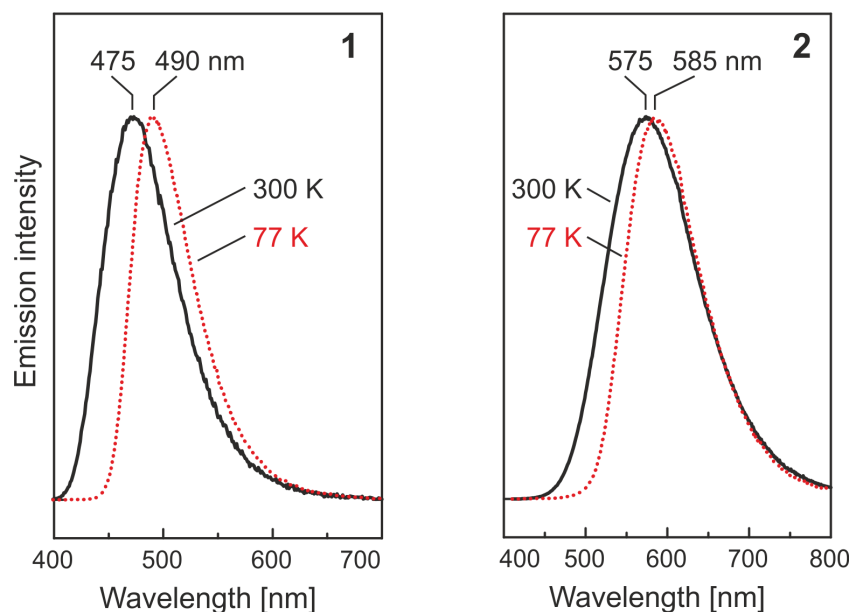
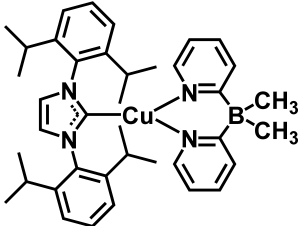
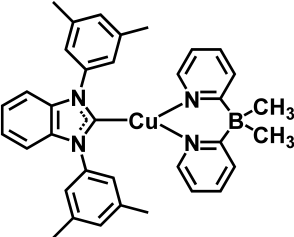


Figure 4.8: Normalized emission spectra of compound **1** and **2** as powders at ambient temperature and at 77 K. The samples were excited at  $\lambda_{exc} = 350$  nm.

compounds are comprised of metal and  $\text{py}_2\text{-BMe}_2$  orbitals, giving HOMO energies that are nearly unchanged. As a result, the HOMO–LUMO gap and therefore, the emission energy is lower for **2** than for **1**.<sup>68</sup>

When cooling from ambient temperature to 77 K, a red-shift of the emission from 475 nm to 490 nm ( $\approx 650$   $\text{cm}^{-1}$ ) is observed for compound **1**. In addition, the emission decay time increases by a factor of about three from 11  $\mu\text{s}$  to 34  $\mu\text{s}$ , whereas the radiative rate  $k_r = \Phi_{PL} \tau^{-1}$  decreases by about the same factor from  $6.9 \times 10^4 \text{ s}^{-1}$  to  $2.7 \times 10^4 \text{ s}^{-1}$ . The significantly longer emission decay time at  $T = 77$  K of 34  $\mu\text{s}$  (compared to the 11  $\mu\text{s}$  found at 300 K) suggests that the emitting state at  $T = 77$  K is the triplet state  $T_1$ . Further proof for this assignment is given in section 4.2.3. However, it is remarked that a triplet decay time of 34  $\mu\text{s}$  is extraordinarily short compared to other Cu(I) presented in this thesis and found in the literature.<sup>5,32,33,35,81,144</sup> This indicates that spin-orbit coupling (SOC) is particularly effective in compound **1**. A more detailed discussion of this is given in sections 4.2.2 and 4.2.3. The observed changes of the emission decay time or the radiative rate and the spectral shift of the emission peaks upon temperature change can be explained by the occurrence of a TADF at  $T = 300$  K and is discussed in more detail in section 4.2.3. In contrast, the emission decay time of compound **2** changes only slightly from 21  $\mu\text{s}$  to 18  $\mu\text{s}$  when heating from  $T = 77$  K to ambient temperature. Almost

Table 4.3: Structures and emission properties of the compounds (IPr)Cu(py<sub>2</sub>-BMe<sub>2</sub>) (**1**) and (Bzl-3,5Me)Cu(py<sub>2</sub>-BMe<sub>2</sub>) (**2**) as powders. The decay time is monoexponential in the entire temperature range above  $\approx 25$  K. The radiative  $k_r$  and non-radiative  $k_{nr}$  rates were calculated according to  $k_r = \Phi_{PL} \tau^{-1}$  and  $k_{nr} = (1 - \Phi_{PL}) \tau^{-1}$ , respectively.

	<b>1</b>		<b>2</b>	
				
Temp. [K]	300	77	300	77
$\lambda_{max}$ [nm]	475	490	575	585
$\Phi_{PL}$ [%]	76	91	73	80
$\tau$ [ $\mu$ s]	11	34	18	21
$k_r$ [ $10^4$ s <sup>-1</sup> ]	6.9	2.7	4.1	3.8
$k_{nr}$ [ $10^4$ s <sup>-1</sup> ]	2.2	0.3	1.5	1.0

no change is found for the radiative rate amounting to  $k_r(77\text{ K}) = 3.8 \times 10^4 \text{ s}^{-1}$  and  $k_r(300\text{ K}) = 4.1 \times 10^4 \text{ s}^{-1}$ , respectively. This indicates that for compound **2** TADF is not effective and that the observed emission even at ambient temperature is a phosphorescence stemming from T<sub>1</sub>. The slight red-shift of the high energy flank observed on cooling may be explained (especially for this triplet emitter) by freezing out energetically higher lying emissions from an inhomogeneously broadened distribution in the powder sample (compare reference 96) and is therefore *not* a result of the freezing out of the singlet emission. This is in contrast to compound **1** for which the entire spectrum is shifted. (4.8) Further support for this rationalization is given by the investigation of the emission spectra in a PMMA (polymethylmethacrylate) matrix at 300 K and 77 K. In this situation, no such spectral change on temperature variation is observed, besides a slight narrowing on cooling.

### 4.2.2 Compound 2 – Typical Triplet Emitter

In this section, the discussion is focused on compound **2**. More specifically, the decay behavior of this compound is investigated in the temperature range between 1.3 K and 300 K (Figure 4.9) which is particularly instructive.

From Figure 4.9, it can be seen that the (thermalized) decay time for compound **2** is almost constant in the temperature range between  $\approx 10$  K and 300 K and amounts to about 20  $\mu\text{s}$ . Also the radiative rate is essentially constant (compare Table 4.3) which allows assigning the emission as phosphorescence stemming from the  $T_1$  state in the entire temperature range. An emission via the TADF mechanism (compare section 4.2.3) is not occurring in this case. Thus, it can be concluded that the energy splitting  $\Delta E(S_1 - T_1)$  between the first excited singlet and triplet state is larger than  $3000\text{ cm}^{-1}$  as for such a large value no significant thermal activation is expected at  $T = 300$  K.

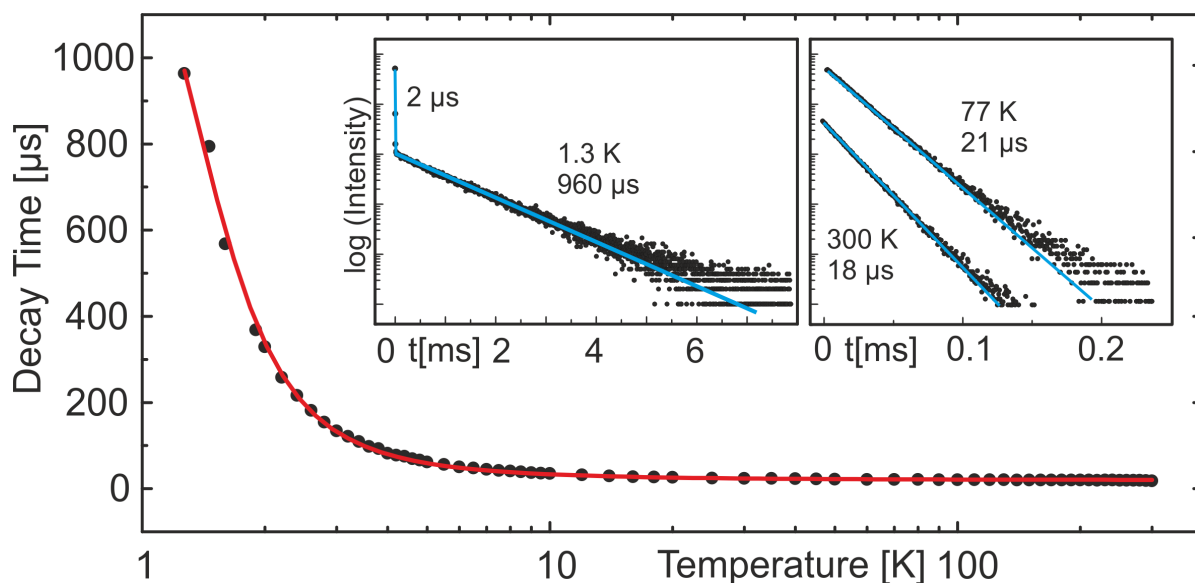


Figure 4.9: Thermalized emission decay time of compound **2** (powder) versus temperature. The sample was excited at  $\lambda_{exc} = 355$  nm and the signal was detected at  $\lambda_{det} = 600$  nm. The red line represents a fit according to equation 4.2. Insets: Decay curves at 1.3 K, 77 K, and 300 K.

Interestingly, when the temperature is decreased below  $\approx 10$  K a steep increase of the decay time from about 20  $\mu\text{s}$  to 1 ms at  $T = 1.3$  K is observed. A similar behavior is well known from other transition metal compounds, such as Ir(III) and Pt(II) compounds,<sup>5,65,76,88,118,145,146</sup> and can be related to the energy splitting of the triplet state into

three substates. This so-called zero-field splitting (ZFS) is a consequence of spin-orbit coupling (SOC). Apart from the fast component with a decay time of 2  $\mu\text{s}$  found at  $T = 1.3\text{ K}$ , the emission decay time at low temperature is governed by a Boltzmann distribution of the three substates I, II, and III. According to the monoexponential decay, these states are in a thermal equilibrium (after several  $\mu\text{s}$ ). At low temperature, mainly emission from the energetically lowest substates I (and II) is observed. With increasing temperature, the higher lying substate III is thermally populated. Since frequently, the radiative rates corresponding to the transitions from the energetically higher lying substates to the  $S_0$  ground state are larger than the rates corresponding to the lowest substate(s), the averaged emission decay time decreases with increasing temperature.<sup>5,28,65,76,88,118,145,146</sup> Accordingly, the data given in Figure 4.9 can be fitted with a modified Boltzmann function (equation 4.2) in order to determine the ZFS values and the decay time constants of the individual triplet substates (compare references 28, 65, 118).

$$\tau(T) = \left[ 1 + e^{-\frac{\Delta E(II-I)}{k_B T}} + e^{-\frac{\Delta E(III-I)}{k_B T}} \right] \times \left[ \tau_I^{-1} + \tau_{II}^{-1} e^{-\frac{\Delta E(II-I)}{k_B T}} + \tau_{III}^{-1} e^{-\frac{\Delta E(III-I)}{k_B T}} \right]^{-1} \quad (4.2)$$

In this equation,  $\tau(T)$  refers to the emission decay time at a given temperature  $T$ ,  $\tau_I$ ,  $\tau_{II}$ , and  $\tau_{III}$  to the individual decay times of the three triplet substates (I, II, and III),  $\Delta E(III - I)$  and  $\Delta E(II - I)$  to the energy splittings between the triplet substates III/I and II/I, respectively, and  $k_B$  to the Boltzmann constant.

As a result of the fitting procedure, a value of  $\Delta E(III - I) = \Delta E(\text{ZFS}) = 5\text{ cm}^{-1}$  was found. Such large ZFS values are only rarely found for Cu(I) complexes and only one example of a similarly large ZFS splitting has been reported recently.<sup>106</sup> However, by this procedure, it could not be determined where substate II is energetically located with respect to substate I and III. If it is assumed that substates I and II are energetically close ( $\Delta E(II - I) \approx 0\text{ cm}^{-1}$ , compare references 5, 33), the emission decay times of the three triplet substates can be obtained. They amount to  $\tau_I \approx \tau_{II} = 1.5\text{ ms}$  and  $\tau_{III} = 7\text{ }\mu\text{s}$ . The results found for compound **2**, especially the value of  $\text{ZFS} = 5\text{ cm}^{-1}$  and the average emission decay time match well with an empirical ordering scheme that correlates  $\Delta E(\text{ZFS})$  with the phosphorescence decay time.<sup>1,5</sup> From this perspective it is

not surprising that a ZFS value of  $5\text{ cm}^{-1}$  is found for a compound with a triplet decay time of about  $20\text{ }\mu\text{s}$ .

The short emission decay component of  $2\text{ }\mu\text{s}$  at  $T = 1.3\text{ K}$  becomes shorter and the component diminishes rapidly with increasing temperature and cannot be observed at temperatures higher than  $\approx 25\text{ K}$ . Such a behavior indicates the occurrence of a relatively slow spin-lattice relaxation (SLR) from the higher lying triplet substate III to the substates I and II according to the *direct* process of SLR.<sup>76,145</sup> Moreover, in a very rough estimate, one can use the measured value of  $\tau(\text{SLR}) = 2\text{ }\mu\text{s}$  to determine the energy separation between the involved states, i. e. the value of  $\Delta E(\text{ZFS})$ . With the relation of  $\Delta E(\text{ZFS})^3 \propto \tau(\text{SLR})^{-1}$  for the direct process of SLR and the corresponding values known from other organo-transition metal compounds,<sup>76,145</sup> one obtains a value of  $4\text{ cm}^{-1}$  which nicely confirms the splitting values as determined from the fitting procedure as discussed above.

### 4.2.3 Compound 1 – Thermally Activated Delayed Fluorescence

In Figure 4.10, the emission decay time of compound **1** is displayed versus temperature. Similar as for compound **2**, two decay components are observed in the temperature range between  $1.3\text{ K}$  and  $\approx 25\text{ K}$  (not displayed in Figure 4.10). The short component can again be assigned to SLR processes, whereas the long component corresponds to the thermalized emission of the three triplet substates (compare previous section). As for compound **2**, a significant reduction of the decay time between  $T = 1.3\text{ K}$  and  $10\text{ K}$  from  $110\text{ }\mu\text{s}$  to  $40\text{ }\mu\text{s}$  is observed. Again, this can be assigned to the thermal population of higher lying triplet substates from the lowest one(s) leading to an average value of  $34\text{ }\mu\text{s}$  between  $\approx 10\text{ K}$  and  $\approx 100\text{ K}$  (“plateau”).

However, in contrast to the behavior of compound **2**, the emission decay time of compound **1** is not constant up to  $T = 300\text{ K}$ . It decreases from about  $34\text{ }\mu\text{s}$  to  $11\text{ }\mu\text{s}$  at ambient temperature. This effect can be rationalized by the following considerations. At low temperature, only the triplet state  $T_1$  is contributing to the emission. With increasing temperature, a thermal population of the energetically higher lying singlet  $S_1$  state becomes possible. As the  $S_1$  state exhibits a significantly shorter emission decay time than the  $T_1$  state, an overall reduction of the emission decay time is observed with increasing temperature. Additionally, a blue-shift of the emission occurs as the  $S_1$  state lies energetically higher than the  $T_1$  state. This emission mechanism corresponds to a

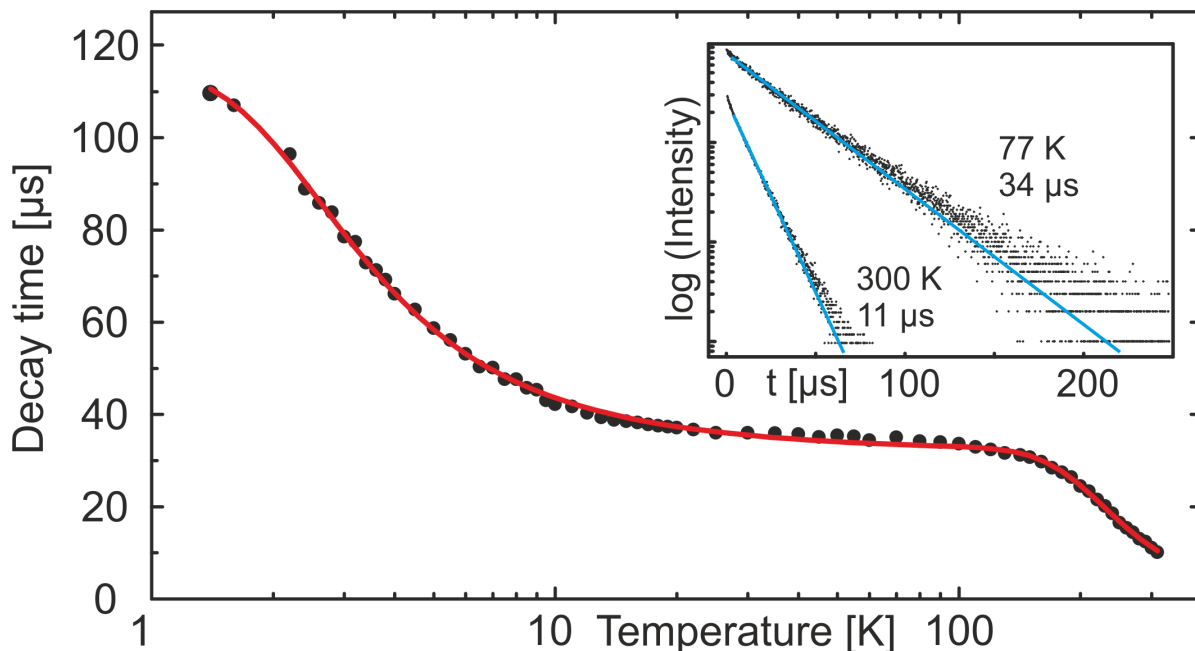


Figure 4.10: Emission decay time of compound **1** as powder versus temperature. The sample was excited at  $\lambda_{exc} = 378$  nm and the signal was detected at  $\lambda_{det} = 490$  nm. The red line represents a fit according to equation 4.3. Inset: Decay curves at  $T = 77$  K and 300 K.

TADF.

The measured data, as displayed in Figure 4.10, can be fitted with equation 4.3, which represents an expansion of equation 4.2 by two additional terms (marked in red), which take the thermal population of the singlet state  $S_1$  into account.

$$\tau(T) = \left[ 1 + e^{-\frac{\Delta E(II-I)}{k_B T}} + e^{-\frac{\Delta E(III-I)}{k_B T}} + e^{-\frac{\Delta E(S_1-T_1)}{k_B T}} \right] \times \left[ \tau_I^{-1} + \tau_{II}^{-1} e^{-\frac{\Delta E(II-I)}{k_B T}} + \tau_{III}^{-1} e^{-\frac{\Delta E(III-I)}{k_B T}} + \tau_{S_1}^{-1} e^{-\frac{\Delta E(S_1-T_1)}{k_B T}} \right]^{-1} \quad (4.3)$$

From the fitting procedure, the decay times of the three triplet substates of  $\tau_I \approx \tau_{II} = 116 \mu\text{s}$  and  $\tau_{III} = 13 \mu\text{s}$  and a value of  $\Delta E(\text{ZFS}) = 4 \text{ cm}^{-1}$  was found. The latter one is only slightly smaller than found for compound **2**. Similarly as for compound **2**, the energy of substate II with respect to substate I and III could not be determined. For the fitting procedure  $\Delta E(\text{II} - \text{I}) = 0 \text{ cm}^{-1}$  was assumed. The energy splitting between the first

excited triplet  $T_1$  and singlet  $S_1$  state is determined to  $\Delta E(S_1 - T_1) = 740 \text{ cm}^{-1}$ . This value is in good agreement with the blue-shift of the emission spectrum when heating from 77 K to 300 K amounting to  $650 \text{ cm}^{-1}$ . The corresponding emission decay time of the singlet state is found to be  $\tau(S_1) = 160 \text{ ns}$ . Such a short decay time emphasizes the singlet nature of this state. It is remarked that in contrast to the delayed fluorescence, a prompt fluorescence is not observed for this compound as intersystem crossing (ISC) from the  $S_1$  to the  $T_1$  state, probably being of the order of 10 ps,<sup>79,86,87</sup> is much faster than the prompt  $S_1 \rightarrow S_0$  emission.

Interestingly, the increase of the radiative rate and the related decrease of the emission decay time with increasing temperature is for compound **1** significantly less pronounced than for other Cu(I) complexes. For example, the copper complexes presented in chapter 3 show an increase of the radiative rates by the TADF process by a factor of 40 to 150, whereas compound **1** exhibits only an increase by a factor of 3. An explanation for this behavior can be given when the emission decay path from the triplet to the singlet ground state is also taken into account. For the compounds in section 3, the triplet state decay times are long, lying between 250  $\mu\text{s}$  and 2200  $\mu\text{s}$ , whereas compound **1** exhibits a decay time of only 34  $\mu\text{s}$ . Therefore, a reduction of the decay time by involving the TADF process at higher temperatures is much less effective.

#### 4.2.4 Controlling TADF by Ligand Orientation

As discussed in section 4.2.1, at ambient temperature compound **1** displays an effective TADF, whereas for compound **2** thermal population of the singlet state is not observed due to the activation energy being greater than  $3000 \text{ cm}^{-1}$ . Obviously, this effect is connected to differences in the chemical structures of the NHC (N-heterocyclic) ligands on the molecules. From Table 4.4 it can be seen that the compounds differ in two aspects. (i) the  $\pi$ -system of the imidazole ring in compound **1** is expanded by benzannulation in compound **2**. (ii) The isopropyl groups at the 2,6-positions on the pendant phenyl rings of the NHC ligand in **1** are replaced by methyl groups at the 3,5-positions giving compound **2**.

For a better understanding of the effects of these modifications on the energy gap  $\Delta E(S_1 - T_1)$  between the first excited singlet and triplet state, DFT and TDDFT calculations were performed for compound **1** and **2** as well as for two further model compounds **1a** and **2a** as are displayed in Table 4.4. Compound **1a** represents a modified



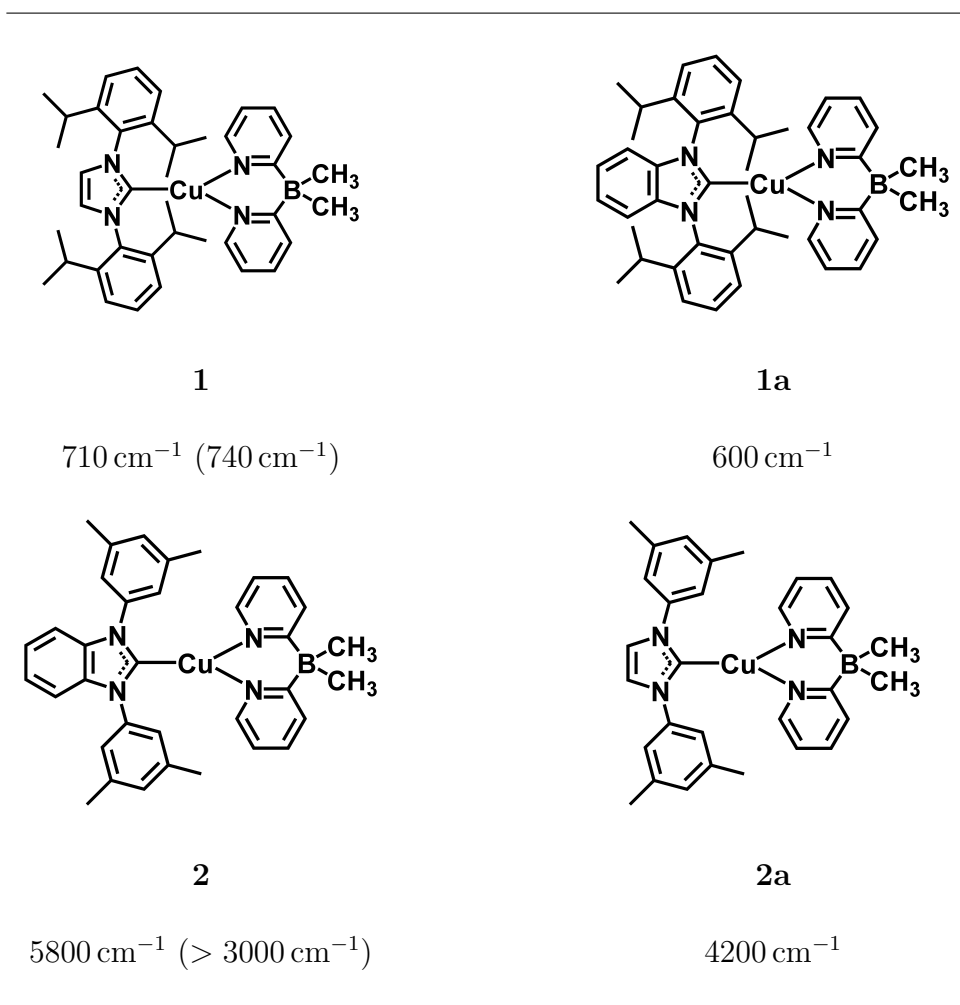
version of compound **1** in which the imidazole ring is  $\pi$ -extended to benzimidazole, but the isopropyl groups on the phenyl rings are retained. Compound **2a** represents a modification of compound **2** where the  $\pi$ -system of the benzimidazole moiety is trimmed to imidazole, but the methyl groups are left unchanged. For all four structures displayed in Table 4.4, a DFT geometry optimization for the electronic ground state was performed. As starting geometry, the crystal structures were used as described and provided in reference 68. The starting geometries of compounds **1a** and **2a** were created by expanding or contracting the  $\pi$ -system, respectively, of the NHC ligand in the structures of compound **1** and **2**. TDDFT calculations were performed on the structures obtained after geometry optimization.

It was found that compound **1** and **1a** exhibit similar (and small) singlet-triplet gaps of  $710\text{ cm}^{-1}$  and  $600\text{ cm}^{-1}$ , respectively. This is in good agreement with the experimental value found for compound **1** amounting to  $\Delta E(S_1 - T_1) = 740\text{ cm}^{-1}$  (compare section 4.2.3). For compound **2** and **2a**, large values of  $5800\text{ cm}^{-1}$  and  $4200\text{ cm}^{-1}$ , respectively, were found (Table 4.4). These results indicate that expanding the  $\pi$ -system of the NHC ligand does not have a strong impact on the singlet-triplet splitting. Therefore, these modifications cannot explain the experimentally found differences with values of  $\Delta E(S_1 - T_1) = 740\text{ cm}^{-1}$  for **1** and of  $\Delta E(S_1 - T_1) > 3000\text{ cm}^{-1}$  for **2**.

Interestingly, the insensitivity of the exchange energy to benzannulation of the imidazole ring indicates that the methyl and isopropyl groups present at the IPr and Bzl-3,5Me ligands play an important role for the  $\Delta E(S_1 - T_1)$  value and the occurrence of TADF. However, it seems unlikely that these groups impart a direct electronic impact on the singlet-triplet splitting. Instead, the alkyl groups can exert steric control over the orientation of the two ligands towards each other and change the electronic behavior of the compounds in this manner. In support, the X-ray structures (compare reference 68) show that for compound **1**, the IPr and the  $\text{py}_2\text{BMe}_2$  are nearly coplanar, whereas for compound **2**, the Bzl-3,5Me and  $\text{py}_2\text{-BMe}_2$  ligands are almost perpendicular to each other (Figure 4.11).

Thus, the influence of the relative orientations of the ligands towards each other on the singlet-triplet energy splitting was investigated using a model compound **1b** (Figure 4.11). In this model compound, the isopropyl groups were removed from the phenyl rings of the NHC ligand. This change allows for variation of the N-C-Cu-N torsion angle (marked green in Figure 4.13) without encountering steric hindrance from the adjacent  $\text{py}_2\text{-BMe}_2$  ligand. The N-C-Cu-N torsion angle of **1b** was then fixed at values between  $0^\circ$  and  $100^\circ$

Table 4.4: Chemical structures of compounds **1** and **2** as well as of the modified versions **1a** and **2a**. The values for  $\Delta E(S_1 - T_1)$  obtained from TDDFT calculations and from experimental investigations (in brackets) are also displayed.



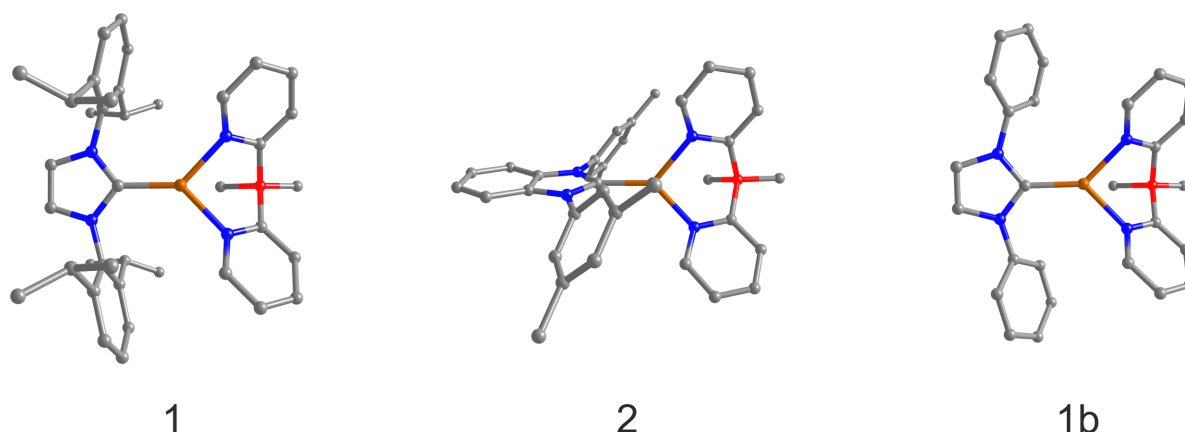


Figure 4.11: Perspective drawing of the optimized geometries of compounds **1** and **2** as well as of the model compound **1b**. Hydrogen atoms were omitted for clarity.

in steps of  $10^\circ$  for a DFT geometry optimization of the singlet ground state. Interestingly, these calculations show that the spatial distribution of the HOMO changes with variation of the torsion angle. In particular, for an angle of  $0^\circ$  the HOMO is localized on the copper center and the  $\text{py}_2\text{-BMe}_2$  ligand, whereas it is extended onto the imidazole ring when the angle is  $90^\circ$  (compare Figure 4.12). In contrast, the LUMO remains localized on the  $\pi^*$ -orbitals of the NHC ligand for all torsion angles. The difference in the HOMO is due to the angular relation between the metal d- and imidazole  $\pi$ -orbitals. When the ligands are coplanar the two sets of orbitals are (spatially) orthogonal and thus do not electronically couple to each other. However, in the perpendicular orientation the orbitals have the appropriate symmetry to conjugate and delocalize their electronic distribution onto both ligands. Consequently, spatial overlap between HOMO and LUMO is small when the torsion angle is  $0^\circ$  (hence a small exchange energy results), whereas a significant overlap exists between the frontier orbitals with a  $90^\circ$  torsion thereby increasing the exchange energy. Since the lowest excited singlet and triplet states are largely comprised from transitions between these frontier orbitals ( $> 94\%$  for the  $S_1$  and  $> 82\%$  for the  $T_1$  state, see Table 4.5) variation in the degree of spatial overlap will strongly alter the value of  $\Delta E(S_1 - T_1)$ .

A more accurate estimate of the dependence of the singlet-triplet splitting on the torsion angle can be made when TDDFT calculations are performed on the (torsion constrained) optimized geometries. As compound **1b** exhibits a symmetry element at all

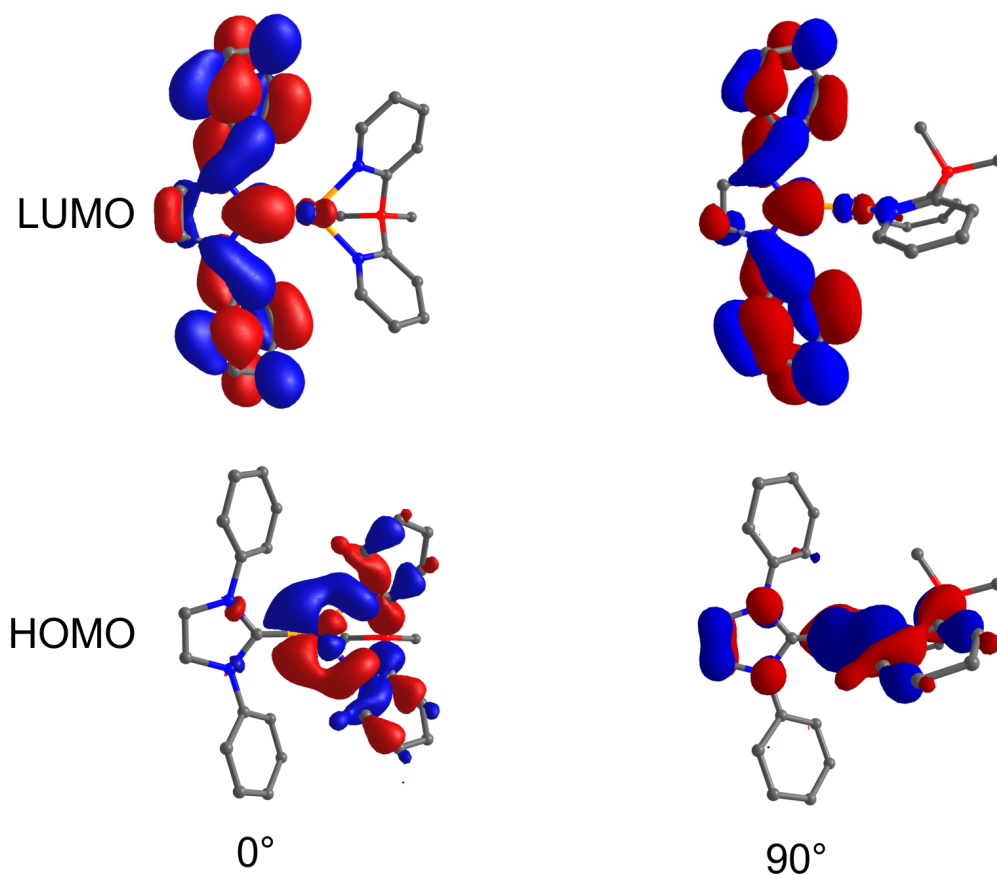


Figure 4.12: HOMOs and LUMOs of model compound **1b** displayed for a torsion angle of 0° and 90°, respectively.

rotations (either a mirror plane or a  $S_2$  axis), the values of  $\Delta E(S_1 - T_1)$  are identical at positive and negative torsion angles. The data, displayed in Figure 4.13, show that the singlet-triplet splitting in **1b** is lowest  $540\text{ cm}^{-1}$  when the N–C–Cu–N torsion angle between the two ligands is 0°. This result is in agreement with the experimental data found for compound **1** with a torsion angle of 5° and a singlet-triplet splitting of  $740\text{ cm}^{-1}$ . In contrast, when the torsion angle is 70° (as realized for compound **2**) a splitting of  $3700\text{ cm}^{-1}$  is obtained from the calculations. For such a large  $\Delta E(S_1 - T_1)$  energy separation no TADF would occur at ambient temperature. These model calculations strongly support the experimental results of a lower  $\Delta E(S_1 - T_1)$  limit of  $3000\text{ cm}^{-1}$  as predicted for compound **2**.

Table 4.5: Percental contribution of the HOMO–LUMO transition to the S<sub>1</sub> and T<sub>1</sub> states. Data given for compound **1b** at the B3LYP/def2-SVP level of theory.

Torsion angle	S <sub>1</sub>	T <sub>1</sub>
0°	0.95	0.93
10°	0.95	0.92
20°	0.95	0.91
30°	0.94	0.90
40°	0.94	0.88
50°	0.95	0.85
60°	0.97	0.82
70°	0.96	0.85
80°	0.98	0.88
90°	0.99	0.88
100°	1.00	0.88

### 4.2.5 Conclusion

Materials that are applied as emitters in organic light-emitting diodes should be able to utilize all injected excitons for the generation of light. At the moment, these requirements are best met by materials that exhibit the triplet harvesting effect, typically based on high-cost Pt(II) or Ir(III) complexes, or the singlet harvesting effect, typically based on low-cost Cu(I) complexes or purely organic materials. Emitters showing the triplet harvesting effect hereby stand out through very effective spin-orbit coupling, whereas emitters exhibiting the singlet harvesting effect excel through a small energy splitting between the first excited triplet and singlet state resulting in a thermally activated delayed fluorescence.

Both mechanisms lead to an effective reduction of the emission decay time and allow exploiting singlet and triplet excitons for the generation of light in an OLED. One of the compounds presented in this section (compound **1**) combines the advantages of both the triplet and the singlet harvesting effect. (i) It exhibits relatively strong spin-orbit coupling which results in a (compared to other Cu(I) compounds known so far) very short triplet emission decay time of only 34  $\mu$ s. (ii) The energy splitting between the first excited singlet and triplet state amounts to only 740  $\text{cm}^{-1}$ . Therefore the compound exhibits an effective TADF. The contribution of each of the two effects to the emission can be quantified according to equations 3.4 and 3.5 in section 3.1.4.

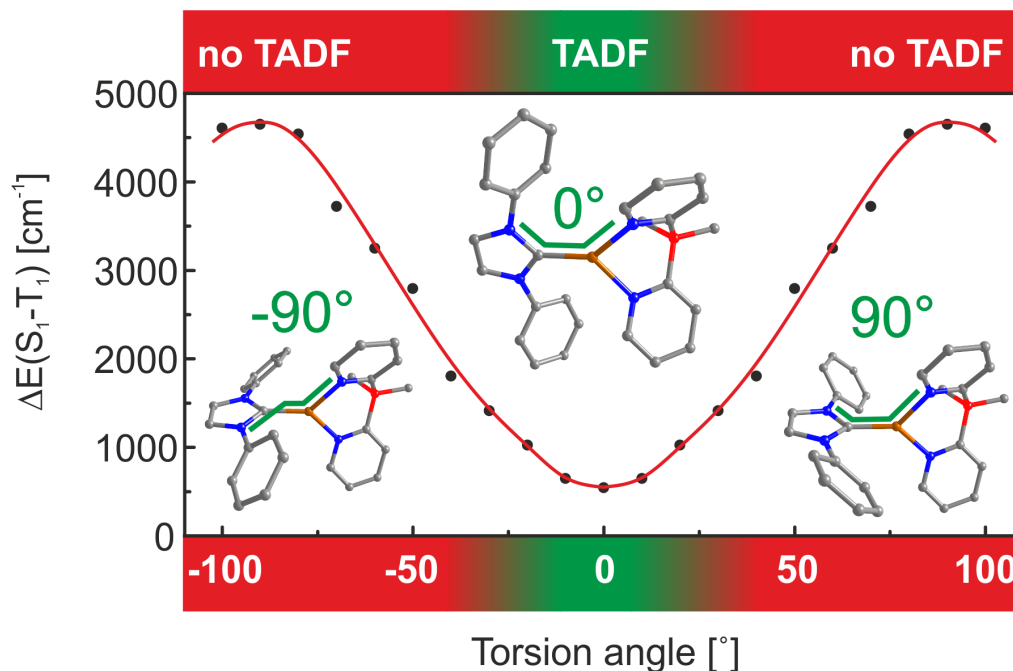


Figure 4.13: Singlet-triplet splitting  $\Delta E(S_1 - T_1)$  in dependence of the torsion angle N-C-Cu-N (marked by the green line) as obtained from DFT and TDDFT calculations on the B3LYP/def2-SVP level of theory.

It is found that at ambient temperature 38 % of the emission intensity stems from the triplet state and 62 % from the singlet state. Accordingly, the deactivation via both radiative decay paths induces a greater overall radiative deactivation rate. Thus, due to the combination of phosphorescence and delayed fluorescence an effective decay time of  $\tau = 11 \mu\text{s}$  can be achieved which is shorter than the decay times of the individual processes ( $\tau_{TADF}(300 \text{ K}) = 16 \mu\text{s}$  and  $\tau_{Ph} = 34 \mu\text{s}$ ).

Another important issue that has been revealed in this investigation is the connection between the orientation of the ligands towards each other and the value of the activation energy for a TADF process. The ligand orientation is crucial for the difference between a good OLED emitter with relatively short decay time and an emitter with too long emission decay time for good OLED performance. Therefore, the results presented here give valuable guidelines for the development of new TADF emitter materials.

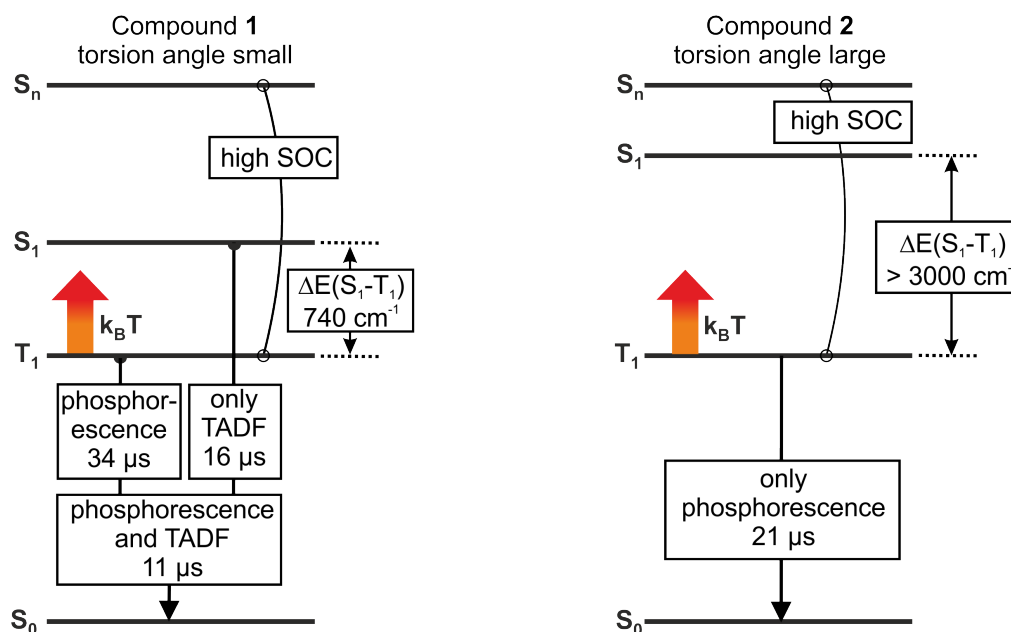


Figure 4.14: Energy level diagrams of compound **1** and **2**. At ambient temperature, compound **2** shows only emission from the triplet state, while compound **1** additionally exhibits a TADF. The combination of TADF *and* triplet emission (phosphorescence) results in a distinct reduction of the emission decay time. The triplet state exhibit zero-field splittings of  $4\text{ cm}^{-1}$  and  $5\text{ cm}^{-1}$  for compound **1** and **2**, respectively. The TADF decay time  $\tau(\text{TADF})$  at  $T = 300\text{ K}$  was calculated according to  $\tau(\text{phosphorescence} + \text{TADF})^{-1} = \tau(\text{phosphorescence})^{-1} + \tau(\text{TADF})^{-1}$ . Note that the given phosphorescence decay times are the  $T = 77\text{ K}$  values.





## Experimental Section

All investigated substances were provided by cooperation partners. The synthetic routes are described in references 36, 41, 68, 95. Emission and excitation spectra were measured with a Fluorolog 3-22 (Horiba Jobin Yvon) spectrometer which was equipped with a cooled photomultiplier (RCA C7164R). For the measurement of the emission decay times the same photomultiplier was used in combination with a FAST multichannel scaler PCI card (Comtec). As excitation source for the decay time measurements a pulsed diode laser (Picobrite PB-375L,) with an excitation wavelength of 378 nm and a pulse width  $< 100$  ps or a pulsed Nd:YAG Laser (IB Laser Inc. DiNY pQ 02) with an excitation wavelength of 355 nm and a pulse width  $< 7$  ns were used. For adjusting the temperature in the range between 1.3 K and 300 K, the samples were placed into a helium cryostat (Cryovac Konti Cryostat IT) in which the helium gas flow and heating were controlled. Absolute measurements of the photoluminescence quantum yields at ambient temperature and at 77 K, respectively, were performed with a C9920-02 (Hamamatsu Photonics) system. Absorption spectra were recorded using a Cary 300 (Varian) two beam spectrometer. For measurements of emission properties in solution, all samples were deoxygenated by at least five freeze-pump-thaw cycles. Measurements were performed in dilute solutions to prevent concentration effects. For the same reason, the doping concentration for measurements in polymethylmethacrylate film was chosen to be less than 1 wt %. DFT and TDDFT calculations were carried out using NWChem 6.3 on a high performance computing cluster.<sup>147</sup> The calculations were performed on the B3LYP/def2-SVP level of theory,<sup>148,149</sup> which has shown to give good results for other Cu(I) compounds.<sup>107</sup>



## Summary

In this thesis, different classes of OLED (Organic Light-Emitting Diodes) relevant Cu(I) and Ag(I) complexes have been investigated. Within each compound class two or more specific complexes with slightly altered chemical structures have been studied to establish relationships between chemical structures and photophysical properties. The compounds have been studied in a wide temperature range between 1.3 K and 300 K. For some materials, also the influence of the surrounding environment on the emission behavior has been investigated. In addition, density functional (DFT) and time-dependent density functional (TDDFT) methods have been applied to get further insight into the electronic structure. In the following, an overview over the results obtained in the scope of this thesis is given. It is noted that parts of these summaries have been extracted from the abstracts of references 36, 39, 41, 42.

### Complexes with two copper centers

In the first part of chapter 3, the four Cu(I) complexes  $[\text{Cu}(\mu\text{-Cl})(\text{PNMe}_2)]_2$ ,  $[\text{Cu}(\mu\text{-Br})(\text{PNMe}_2)]_2$ ,  $[\text{Cu}(\mu\text{-I})(\text{PNMe}_2)]_2$ , and  $[\text{Cu}(\mu\text{-I})(\text{PNpy})]_2$  (structures displayed on page 36) have been investigated. They represent a series of dinuclear compounds in which an aminophosphine ligand is coordinated to each copper center and where the copper centers themselves are bridged by two halides. At ambient temperature, the complexes exhibit strong blue and green emission as powders with emission maxima ranging from  $\lambda_{\text{max}} = 464 \text{ nm}$  to  $506 \text{ nm}$  and emission quantum yields as high as 65 % at decay times as short as  $4 \mu\text{s}$ . Interestingly, it was found that the bridging halides distinctly alter the

emission energy, whereas the spatial separation of the two copper centers does not have a significant impact on this. Moreover, all compounds do not show effects of concentration quenching at high emitter concentration, a property that might be attractive for reducing the efficiency roll-off in OLEDs at higher current densities. An investigation of the emission decay behavior between 1.3 K and 300 K gives insight into the nature of the emitting states. At temperatures below  $\approx 60$  K, the decay times of the studied compounds amount to several hundred microseconds, which indicates that the emission originates from a triplet state ( $T_1$  state). DFT calculations show that this state is of (metal+halide)-to-ligand charge transfer  $^3(M+X)LCT$  character. Studies at  $T = 1.3$  K allow to gain insight into the three triplet substates, in particular, to determine the individual substate decay times being as long as a few milliseconds. The energy splitting of these three substates, the zero-field splitting (ZFS), could be determined to be smaller than  $2 \text{ cm}^{-1}$ . With an analysis of these data, conclusions about the effectiveness of spin-orbit coupling (SOC) can be drawn. Interestingly, the large differences of the spin-orbit coupling (SOC) constants of the halides are not obviously displayed in the triplet state properties. With temperature increase from  $T \approx 60$  K to 300 K, a significant decrease of the emission decay time by almost two orders of magnitude is observed, and at ambient temperature, the decay times amount to only  $4 \mu\text{s} - 7 \mu\text{s}$  without a significant reduction of the emission quantum yield. This drastic decrease of the (radiative) decay time is a result of the thermal population of a short-lived singlet state ( $S_1$  state) that lies energetically only a few hundred wavenumbers ( $460 \text{ cm}^{-1} - 630 \text{ cm}^{-1}$ ) higher than the  $T_1$  state. Such an emission mechanism corresponds to a thermally activated delayed fluorescence (TADF). At ambient temperature, almost only a delayed fluorescence ( $\approx 98\%$ ) is observed.

In the second part of chapter 3, the photophysical investigations are extended to the dinuclear  $\text{Cu}_2\text{Cl}_2(\text{dppb})_2$  complex (structure displayed on page 58). In contrast to the compounds presented in the first part, this complex features diphosphine instead of aminophosphine ligands while the remaining chemical structure is similar. Furthermore, also the Ag(I) homologue  $\text{Ag}_2\text{Cl}_2(\text{dppb})_2$  is studied. The emission maximum of the Cu(I) complex is found to lie at  $\lambda_{max} = 545 \text{ nm}$  and the emission quantum yield amounts to 35%. Compared to this, the emission maximum of the Ag(I) complex is significantly blue shifted by 65 nm resulting in an emission maximum of  $\lambda_{max} = 480 \text{ nm}$ . Interestingly, the emission quantum yield is almost three times higher for the Ag(I) complex amounting to 93%. Therefore, substituting the Cu(I) by an Ag(I) ion represents a promising strategy for engineering highly efficient blue light emitters. Both compounds show a very effective

thermally activated delayed fluorescence with energy splittings  $\Delta E(S_1 - T_1)$  amounting to only  $600 \text{ cm}^{-1}$  for the Cu(I) and  $980 \text{ cm}^{-1}$  for the Ag(I) complex. Consequently, the emission decay times at ambient temperature are short amounting to only  $3 \mu\text{s}$  and  $15 \mu\text{s}$  for the Cu(I) and the Ag(I) complex, respectively. The TADF process is also displayed in the increase of the radiative rate when heating from  $77 \text{ K}$  to  $300 \text{ K}$ . For the Ag(I) complex the radiative rate increases by a factor of 70 from  $8.7 \times 10^2 \text{ s}^{-1}$  to  $6.2 \times 10^4 \text{ s}^{-1}$ . For the Cu(I) complex, the radiative rate even increases by a factor of about 500 from  $2.4 \times 10^2 \text{ s}^{-1}$  to  $1.2 \times 10^5 \text{ s}^{-1}$ . In contrast to this, investigations down to  $T = 30 \text{ K}$  show that emission decay times of the triplet state  $T_1$  are very long amounting to  $\tau = 1.1 \text{ ms}$  for the Ag(I) and to  $\tau = 2.2 \text{ ms}$  for the Cu(I) complex. This indicates that spin-orbit coupling is particularly weak.

Interestingly, from the experimental data obtained from investigations on the dinuclear compounds presented in this chapter, a correlation between the decay time of the singlet state  $S_1$  and the singlet triplet energy splitting  $\Delta E(S_1 - T_1)$  could be proposed. From this it can be concluded that there exists a lower limit for the emission decay time that cannot be overcome by emitters whose emission mechanism corresponds to a pure TADF. For ambient temperature, this limit has been determined to be of the order of about  $4.5 \mu\text{s}$ .

## Complexes with one copper center

In the first part of chapter 4, the two mononuclear complexes  $[\text{Cu(I)(POP)(dmbpy)}]^+$  and  $[\text{Cu(I)(POP)(tmbpy)}]^+$  have been studied (structures displayed on page 70). The compounds exhibit one copper center which is pseudo-tetrahedrally coordinated by the bidentate ligands POP and dmbpy or tmbpy, respectively. At ambient temperature, the emission of  $[\text{Cu(I)(POP)(tmbpy)}]^+$  as powder peaks at  $\lambda_{max} = 555 \text{ nm}$  and the emission quantum yield amounts to 55%. In contrast to this, the emission of  $[\text{Cu(I)(POP)(dmbpy)}]^+$  is red shifted with a maximum at  $\lambda_{max} = 575 \text{ nm}$  and the emission quantum yield is drastically lower amounting to only 9%. Both effects, the red shift of the emission and the lower emission quantum yield, can be related to a flattening distortion from a pseudo-tetrahedral towards a more planar coordination that occurs on excitation. This flattening distortion is assigned to be a consequence of the pronounced metal-to-ligand charge transfer character of the first excited singlet and triplet state. Moreover, the distortion is more pronounced for  $[\text{Cu(I)(POP)(dmbpy)}]^+$ . This is because

$[\text{Cu}(\text{I})(\text{POP})(\text{tmbpy})]^+$  exhibits two additional methyl groups on the tmbpy ligand which sterically interact with the POP ligand and therefore limit the extent of the flattening distortion. Furthermore, it was found that the matrix plays a crucial role for the emission behavior. A relatively rigid matrix, for example solid powder, largely suppresses geometry distortions on excitation whereas in softer matrices, for example fluid solution, this is not the case. As a consequence, the emission of both compounds is red shifted and the emission quantum yield is significantly reduced in solution compared to the powder phase. Interestingly, the emission properties of the powder of  $[\text{Cu}(\text{I})(\text{POP})(\text{tmbpy})]^+$  can be strongly altered by mechanical manipulation, for example by grinding or by compression. Hereby, compression results in an increase of the samples crystallinity, a slight red shift of the emission, and a decrease of the emission quantum yield. This might indicate that compressing the powder sample results in a softer local environment for the emitting molecules. To gain further insight into the electronic structure the emission behavior of  $[\text{Cu}(\text{I})(\text{POP})(\text{tmbpy})]^+$  was investigated in dependence of the temperature. At temperatures lower than  $\approx 100$  K the emission decay time amounts to about 84  $\mu\text{s}$ . With increasing temperature the decay time decreases and reaches 11  $\mu\text{s}$  at ambient temperature. This emission mechanism represents a thermally activated delayed fluorescence. The activation energy for this process could be determined to  $\Delta E(\text{S}_1 - \text{T}_1) = 720 \text{ cm}^{-1}$ .

In the second part of chapter 4, the photophysical properties of the two highly emissive three-coordinate Cu(I) complexes  $(\text{IPr})\text{Cu}(\text{py}_2\text{-BMe}_2)$  and  $(\text{Bzl-3,5Me})\text{Cu}(\text{py}_2\text{-BMe}_2)$  (structures displayed on page 83), with two different N-heterocyclic (NHC) ligands have been investigated in detail. The compounds exhibit remarkably high emission quantum yields of more than 70 % in the powder phase. Despite similar chemical structures of both complexes, at ambient temperature only  $(\text{IPr})\text{Cu}(\text{py}_2\text{-BMe}_2)$  exhibits a thermally activated delayed blue fluorescence ( $\lambda_{\text{max}} = 475 \text{ nm}$ ), whereas compound  $(\text{Bzl-3,5Me})\text{Cu}(\text{py}_2\text{-BMe}_2)$  shows a pure yellow phosphorescence ( $\lambda_{\text{max}} = 575 \text{ nm}$ ). This behavior is related to the torsion angle between the two ligands. Changing this angle has a huge impact on the energy splitting between the first excited singlet  $\text{S}_1$  and triplet  $\text{T}_1$  state and therefore on the TADF properties. In addition, it was found that in both compounds spin-orbit coupling is particularly effective compared to other Cu(I) complexes. This is reflected in short emission decay times of the triplet state of only 34  $\mu\text{s}$  ( $(\text{IPr})\text{Cu}(\text{py}_2\text{-BMe}_2)$ ) and 21  $\mu\text{s}$  ( $(\text{Bzl-3,5Me})\text{Cu}(\text{py}_2\text{-BMe}_2)$ ), respectively, as well as in the zero-field splitting of the triplet state amounting to  $4 \text{ cm}^{-1}$  for  $(\text{IPr})\text{Cu}(\text{py}_2\text{-BMe}_2)$  and  $5 \text{ cm}^{-1}$  for  $(\text{Bzl-3,5Me})\text{Cu}(\text{py}_2\text{-BMe}_2)$ . Accordingly, at ambient temperature, compound

(IPr)Cu(py<sub>2</sub>-BMe<sub>2</sub>) exhibits two radiative decay paths which are thermally equilibrated: one via the S<sub>1</sub> state as TADF path (62%) and one via the T<sub>1</sub> state as phosphorescence (38%). Thus, if the material is applied in an organic light-emitting diode, the generated excitons are harvested mainly in the singlet state, but to a significant portion also in the triplet state. This novel mechanism based on two separate radiative decay paths reduces the overall emission decay time distinctly.





## Conclusion

In recent years it has been recognized that low-cost Cu(I) complexes represent an attractive alternative to high-price Ir(III) and Pt(II) compounds as emitters in organic light-emitting diodes (OLEDs). For this application, Cu(I) complexes should exhibit short emission decay times and high emission quantum yields, properties that strongly depend on the chemical structure of the specific complex. Gaining deeper insight into the structure-property relationship of this emitter class is the central aspect of this thesis.

Typically, emission quantum yields of Cu(I) compounds are relatively low as the complexes undergo pronounced geometry distortions on excitation which results in strong non-radiative deactivation to the ground state. However, if these distortions are largely suppressed the emission quantum yield can be increased significantly. One approach to achieve this is the use of sterically demanding ligands. Another approach is based on an increase of the rigidity of the matrix in which the emitter molecules are embedded. Both concepts have been demonstrated to give good results, but especially the interaction between emitter molecule and matrix environment is underexplored and possesses large potential for an improvement of the emission properties of the guest molecules.

Even if they exhibit high emission quantum yields, most Cu(I) complexes at first sight seem unsuitable for the application in electroluminescent devices due to their long triplet state (phosphorescence) decay times which can amount up to several milliseconds. Such long decay times would result in pronounced saturation effects and significantly lower the efficiency of electroluminescent devices. However, Cu(I) complexes can exhibit a very small energy separation between the first excited singlet and triplet state due to the pronounced charge transfer character of these states. As a consequence, at ambient

temperature a thermally activated delayed fluorescence (TADF) can occur which results in a significant shortening of the decay time.

Interestingly, in this thesis it has been shown that there exists a lower limit for the emission decay time that can be achieved with pure TADF emitters which amounts to approximately 4.5  $\mu\text{s}$ . However, it is suggested that this restriction could be surpassed if an additional radiative decay path is activated. This can be achieved by developing new Cu(I) based emitter materials that exhibit strong spin-orbit coupling (SOC) so that besides the TADF path an efficient radiative deactivation channel via the triplet state as phosphorescence can occur. The combination of both effects, TADF *and* phosphorescence, is well suited to further minimize the emission decay time below the limit mentioned above. However, understanding the processes that lead to efficient SOC in Cu(I) complexes is an object of current research. Further investigations are required to gain an understanding of the SOC process and to systematically develop respective emitter materials.

## Bibliography

- 1 *Highly Efficient OLEDs with Phosphorescent Materials*; Yersin, H., Ed.; Wiley-VCH: Weinheim, Germany, 2008.
- 2 Sasabe, H.; Kido, J. Development of High Performance OLEDs for General Lighting. *J. Mater. Chem. C* **2013**, *1*, 1699.
- 3 Richtlinie über die Förderung zum “Themenfeld Organische Elektronik – Grundlagen der Technologie und Anwendungsszenarien” im Rahmen des Förderprogramms “Photonik Forschung Deutschland”. *BAnz.* **2014**, *AT 18.02.2014 B7*.
- 4 Müller, H. Strahlende Perspektiven., <http://www.welt.de/sonderthemen/light-und-building/article126278393/Strahlende-Perspektiven.html>.
- 5 Yersin, H.; Rausch, A. F.; Czerwieniec, R.; Hofbeck, T.; Fischer, T. The Triplet State of Organo-Transition Metal Compounds. Triplet Harvesting and Singlet Harvesting for Efficient OLEDs. *Coord. Chem. Rev.* **2011**, *255*, 2622.
- 6 Yersin, H.; Rausch, A. F.; Czerwieniec, R., Organometallic Emitters for OLEDs: Triplet Harvesting, Singlet Harvesting, Case Structures, and Trends. In *Physics of Organic Semiconductors*, Brütting, W., Adachi, C., Eds.; Wiley-VCH: Weinheim, Germany, 2012, pp 371–424.
- 7 Brütting, W.; Frischeisen, J.; Schmidt, T. D.; Scholz, B. J.; Mayr, C. Device Efficiency of Organic Light-Emitting Diodes: Progress by Improved Light Outcoupling. *Phys. Status Solidi A* **2013**, *210*, 44.

- 8 Baldo, M. A.; O'Brien, D. F.; You, Y.; Shoustikov, A.; Sibley, S.; Thompson, M. E.; Forrest, S. R. Highly Efficient Phosphorescent Emission from Organic Electroluminescent Devices. *Nature* **1998**, *395*, 151.
- 9 Baldo, M. A.; Lamansky, S.; Burrows, P. E.; Thompson, M. E.; Forrest, S. R. Very High-Efficiency Green Organic Light-Emitting Devices Based on Electrophosphorescence. *Appl. Phys. Lett.* **1999**, *75*, 4.
- 10 Adachi, C.; Baldo, M. A.; Thompson, M. E.; Forrest, S. R. Nearly 100 % Internal Phosphorescence Efficiency in an Organic Light-Emitting Device. *J. Appl. Phys.* **2001**, *90*, 5048.
- 11 Sajoto, T.; Djurovich, P. I.; Tamayo, A. B.; Oxgaard, J.; Goddard, W. A.; Thompson, M. E. Temperature Dependence of Blue Phosphorescent Cyclometalated Ir(III) Complexes. *J. Am. Chem. Soc.* **2009**, *131*, 9813.
- 12 Wagenknecht, P. S.; Ford, P. C. Metal Centered Ligand Field Excited States: Their Roles in the Design and Performance of Transition Metal Based Photochemical Molecular Devices. *Coord. Chem. Rev.* **2011**, *255*, 591.
- 13 Wallesch, M.; Volz, D.; Zink, D. M.; Schepers, U.; Nieger, M.; Baumann, T.; Bräse, S. Bright Opportunities: Multinuclear Cu(I) Complexes with NP Ligands and their Applications. *Chem. Eur. J.* **2014**, *20*, 6578.
- 14 *Electroluminescence I*; Willardson, R., Weber, E., Mueller, G., Eds.; Academic Press: San Diego, CA, United States, 1999.
- 15 Krasnov, A. N. Electroluminescent Displays: History and Lessons Learned. *Displays* **2003**, *24*, 73.
- 16 *Organic Electroluminescence*; Kafafi, Z., Ed.; Taylor & Francis: Boca Raton, FL, United States, 2005.
- 17 Destriau, G. AC Electroluminescence in ZnS. *J. Chim. Phys.* **1936**, *33*, 587.
- 18 Bernanose, A.; Comte, M.; Vouaux, P. Sur un nouveau mode d'émission lumineuse chez certains composés organiques. *J. Chim. Phys.* **1953**, *50*, 64.
- 19 Bernanose, A.; Vouaux, P. Electroluminescence organique: étude du mode d'émission. *J. Chim. Phys.* **1953**, *50*, 261.
- 20 Pope, M.; Kallmann, H. P.; Magnante, P. Electroluminescence in Organic Crystals. *J. Chem. Phys.* **1963**, *38*, 2042.

- 21 Vincett, P.; Barlow, W.; Hann, R.; Roberts, G. Electrical Conduction and Low Voltage Blue Electroluminescence in Vacuum-Deposited Organic Films. *Thin Solid Films* **1982**, *94*, 171.
- 22 Tang, C. W.; VanSlyke, S. A. Organic Electroluminescent Diodes. *Appl. Phys. Lett.* **1987**, *51*, 913.
- 23 Yersin, H.; Finkenzeller, W. J., Triplet Emitters for Organic Light-Emitting Diodes: Basic Properties. In *Highly Efficient OLEDs with Phosphorescent Materials*, Yersin, H., Ed.; Wiley-VCH: Weinheim, Germany, 2008, pp 1–97.
- 24 Reineke, S.; Thomschke, M.; Lüssem, B.; Leo, K. White Organic Light-Emitting Diodes: Status and Perspective. *Rev. Mod. Phys.* **2013**, *85*, 1245.
- 25 Yang, X.; Yao, C.; Zhou, G. Highly Efficient Phosphorescent Materials Based on Platinum Complexes and Their Application in Organic Light-Emitting Devices (OLEDs). *Platin. Met. Rev.* **2013**, *57*, 2.
- 26 Cheng, G.; Chow, P.-K.; Kui, S. C. F.; Kwok, C.-C.; Che, C.-M. High-Efficiency Polymer Light-Emitting Devices with Robust Phosphorescent Platinum(II) Emitters Containing Tetradentate Dianionic ONCN Ligands. *Adv. Mater.* **2013**, *25*, 6765.
- 27 Wang, Q.; Oswald, I. W. H.; Perez, M. R.; Jia, H.; Shahub, A. A.; Qiao, Q.; Gnade, B. E.; Omary, M. A. Doping-Free Organic Light-Emitting Diodes with Very High Power Efficiency, Simple Device Structure, and Superior Spectral Performance. *Adv. Funct. Mater.* **2014**, *24*, 4746.
- 28 Blasse, G.; McMillin, D. R. On the Luminescence of Bis(Triphenylphosphine) Phenanthroline Copper(I). *Chem. Phys. Lett.* **1980**, *70*, 1.
- 29 Ma, Y.-G.; Chan, W.-H.; Zhou, X.-M.; Che, C.-M. Light-Emitting Diode Device from a Luminescent Organocopper(I) Compound. *New J. Chem.* **1999**, *23*, 263.
- 30 Tsuboyama, A.; Kuge, K.; Furugori, M.; Okada, S.; Hoshino, M.; Ueno, K. Photo-physical Properties of Highly Luminescent Copper(I) Halide Complexes Chelated with 1,2-Bis(diphenylphosphino)benzene. *Inorg. Chem.* **2007**, *46*, 1992.
- 31 Yersin, H.; Monkowius, U. Komplexe mit kleinen Singulett-Triplett-Energie-Abständen zur Verwendung in opto-elektronischen Bauteilen (Singulett-Harvesting-Effekt)., DE 10 2008 033563 A1, 2008.

- 32 Deaton, J. C.; Switalski, S. C.; Kondakov, D. Y.; Young, R. H.; Pawlik, T. D.; Giesen, D. J.; Harkins, S. B.; Miller, A. J. M.; Mickenberg, S. F.; Peters, J. C. E-Type Delayed Fluorescence of a Phosphine-Supported  $\text{Cu}_2(\mu\text{-NAr}_2)_2$  Diamond Core: Harvesting Singlet and Triplet Excitons in OLEDs. *J. Am. Chem. Soc.* **2010**, *132*, 9499.
- 33 Czerwieniec, R.; Yu, J.; Yersin, H. Blue-Light Emission of Cu(I) Complexes and Singlet Harvesting. *Inorg. Chem.* **2011**, *50*, 8293.
- 34 Hashimoto, M.; Igawa, S.; Yashima, M.; Kawata, I.; Hoshino, M.; Osawa, M. Highly Efficient Green Organic Light-Emitting Diodes Containing Luminescent Three-Coordinate Copper(I) Complexes. *J. Am. Chem. Soc.* **2011**, *133*, 10348.
- 35 Czerwieniec, R.; Kowalski, K.; Yersin, H. Highly Efficient Thermally Activated Fluorescence of a New Rigid Cu(I) Complex  $[\text{Cu}(\text{dmp})(\text{phanephos})]^+$ . *Dalton T.* **2013**, *42*, 9826.
- 36 Leitl, M. J.; K uchle, F. R.; Mayer, H. A.; Wesemann, L.; Yersin, H. Brightly Blue and Green Emitting Cu(I) Dimers for Singlet Harvesting in OLEDs. *J. Phys. Chem. A* **2013**, *117*, 11823.
- 37 Zink, D. M.; Volz, D.; Baumann, T.; Mydlak, M.; Fl ugge, H.; Friedrichs, J.; Nieger, M.; Br ase, S. Heteroleptic, Dinuclear Copper(I) Complexes for Application in Organic Light-Emitting Diodes. *Chem. Mater.* **2013**, *25*, 4471.
- 38 Igawa, S.; Hashimoto, M.; Kawata, I.; Yashima, M.; Hoshino, M.; Osawa, M. Highly Efficient Green Organic Light-Emitting Diodes Containing Luminescent Tetrahedral Copper(I) Complexes. *J. Mater. Chem. C* **2013**, *1*, 542.
- 39 Leitl, M. J.; Krylova, V. A.; Djurovich, P. I.; Thompson, M. E.; Yersin, H. Phosphorescence versus Thermally Activated Delayed Fluorescence. Controlling Singlet-Triplet Splitting in Brightly Emitting and Sublimable Cu(I)-Compounds. *J. Am. Chem. Soc.* **2014**, *136*, 16032.
- 40 Liu, Z. W.; Qiu, J.; Wei, F.; Wang, J. Q.; Liu, X. C.; Helander, M. G.; Rodney, S.; Wang, Z. B.; Bian, Z. Q.; Lu, Z. H.; Thompson, M. E.; Huang, C. H. Simple and High Efficiency Phosphorescence Organic Light-Emitting Diodes with Codeposited Copper(I) Emitter. *Chem. Mater.* **2014**, *26*, 2368.

- 41 Yersin, H.; Leitl, M. J.; Czerwieniec, R. TADF for Singlet Harvesting – Next Generation OLED Materials Based on Brightly Green and Blue Emitting Cu(I) and Ag(I) Compounds. *P. SPIE* **2014**, *9183*, 91830N.
- 42 Linfoot, C. L.; Leitl, M. J.; Richardson, P.; Rausch, A. F.; Chepelin, O.; White, F. J.; Yersin, H.; Robertson, N. Thermally Activated Delayed Fluorescence (TADF) and Enhancing Photoluminescence Quantum Yields of [CuI(diimine)(diphosphine)]<sup>+</sup> Complexes – Photophysical, Structural, and Computational Studies. *Inorg. Chem.* **2014**, *53*, 10854.
- 43 Gneuß, T.; Leitl, M. J.; Finger, L. H.; Rau, N.; Yersin, H.; Sundermeyer, J. A New Class of Luminescent Cu(I) Complexes with Tripodal Ligands – TADF Emitters for the Yellow to Red Color Range. *Dalton T.* **2014**, DOI: 10.1039/C4DT02631D.
- 44 Zhang, Q.; Li, J.; Shizu, K.; Huang, S.; Hirata, S.; Miyazaki, H.; Adachi, C. Design of Efficient Thermally Activated Delayed Fluorescence Materials for Pure Blue Organic Light Emitting Diodes. *J. Am. Chem. Soc.* **2012**, *134*, 14706.
- 45 Uoyama, H.; Goushi, K.; Shizu, K.; Nomura, H.; Adachi, C. Highly Efficient Organic Light-Emitting Diodes from Delayed Fluorescence. *Nature* **2012**, *492*, 234.
- 46 Nasu, K.; Nakagawa, T.; Nomura, H.; Lin, C. J.; Cheng, C. H.; Tseng, M. R.; Yasuda, T.; Adachi, C. A Highly Luminescent Spiro-Anthracenone-Based Organic Light-Emitting Diode Exhibiting Thermally Activated Delayed Fluorescence. *Chem. Commun.* **2013**, *49*, 10385.
- 47 Zhang, Q. S.; Li, B.; Huang, S. P.; Nomura, H.; Tanaka, H.; Adachi, C. Efficient Blue Organic Light-Emitting Diodes Employing Thermally Activated Delayed Fluorescence. *Nat. Photonics* **2014**, *8*, 326.
- 48 Sun, J. W.; Lee, J. H.; Moon, C. K.; Kim, K. H.; Shin, H.; Kim, J. J. A Fluorescent Organic Light-Emitting Diode with 30 % External Quantum Efficiency. *Adv. Mater.* **2014**, *26*, 5684.
- 49 Kawamura, Y.; Goushi, K.; Brooks, J.; Brown, J. J.; Sasabe, H.; Adachi, C. 100 % Phosphorescence Quantum Efficiency of Ir(III) Complexes in Organic Semiconductor Films. *Appl. Phys. Lett.* **2005**, *86*, 071104.
- 50 Reineke, S.; Baldo, M. A. Recent Progress in the Understanding of Exciton Dynamics within Phosphorescent OLEDs. *Phys. Status Solidi A* **2012**, *209*, 2341.

- 51 Murawski, C.; Leo, K.; Gather, M. C. Efficiency Roll-Off in Organic Light-Emitting Diodes. *Adv. Mater.* **2013**, *25*, 6801.
- 52 Chen, X. L.; Yu, R. M.; Zhang, Q. K.; Zhou, L. J.; Wu, C. Y.; Zhang, Q.; Lu, C. Z. Rational Design of Strongly Blue-Emitting Cuprous Complexes with Thermally Activated Delayed Fluorescence and Application in Solution-Processed OLEDs. *Chem. Mater.* **2013**, *25*, 3910.
- 53 Wei, F.; Zhang, T.; Liu, X.; Li, X.; Jiang, N.; Liu, Z.; Bian, Z.; Zhao, Y.; Lu, Z.; Huang, C. Efficient Nondoped Organic Light-Emitting Diodes with Cu<sup>I</sup> Complex Emitter. *Organic Electronics* **2014**, *15*, 3292.
- 54 Nowy, S.; Frischeisen, J.; Brütting, W. Simulation Based Optimization of Light-Outcoupling in Organic Light-Emitting Diodes. *P. SPIE* **2009**, *7415*, 74151C1.
- 55 Brütting, W.; Frischeisen, J.; Scholz, B. J.; Schmidt, T. D. More Light from Organic Light-Emitting Diodes. *Europhys. News* **2011**, *42*, 20.
- 56 Kim, K. H.; Moon, C. K.; Lee, J. H.; Kim, S. Y.; Kim, J. J. Highly Efficient Organic Light-Emitting Diodes with Phosphorescent Emitters Having High Quantum Yield and Horizontal Orientation of Transition Dipole Moments. *Adv. Mater.* **2014**, *26*, 3844.
- 57 Kunz, D. A.; Leitl, M. J.; Schade, L.; Schmid, J.; Bojer, B.; Schwarz, U. T.; Ozin, G. A.; Yersin, H.; Breu, J. Quasi-Epitaxial Growth of [Ru(bpy)<sub>3</sub>]<sup>2+</sup> by Confinement in Clay Nanoplatelets Yields Polarized Emission. *Small* **2014**, *11*, 792.
- 58 Pfeiffer, M.; Forrest, S.; Leo, K.; Thompson, M. Electrophosphorescent p-i-n Organic Light-Emitting Devices for Very-High-Efficiency Flat-Panel Displays. *Adv. Mater.* **2002**, *14*, 1633.
- 59 *Organic Light-Emitting Devices: A Survey*; Shinar, J., Ed.; Springer: New York, NY, United States, 2004.
- 60 Gustafsson, G.; Cao, Y.; Treacy, G. M.; Klavetter, F.; Colaneri, N.; Heeger, A. J. Flexible Light-Emitting Diodes Made from Soluble Conducting Polymers. *Nature* **1992**, *357*, 477.
- 61 Tsutsui, T., Electroluminescence in Small Molecules. In *Organic Electroluminescence*, Kafafi, Z., Ed.; Taylor & Francis: Boca Raton, FL, United States, 2005, pp 1–21.



- 62 Baldo, M. A.; Forrest, S. R.; Thompson, M. E., Organic Electrophosphorescence. In *Organic Electroluminescence*, Kafafi, Z., Ed.; Taylor & Francis: Boca Raton, FL, United States, 2005, pp 367–305.
- 63 Turro, N., *Modern Molecular Photochemistry*; University Science Books: Sausalito, CA, United States, 1991.
- 64 Rausch, A. F.; Thompson, M. E.; Yersin, H. Blue Light Emitting Ir(III) Compounds for OLEDs – New Insights into Ancillary Ligand Effects on the Emitting Triplet State. *J. Phys. Chem. A* **2009**, *113*, 5927.
- 65 Hofbeck, T.; Yersin, H. The Triplet State of fac-Ir(ppy)<sub>3</sub>. *Inorg. Chem.* **2010**, *49*, 9290.
- 66 Karatsu, T.; Takahashi, M.; Yagai, S.; Kitamura, A. Photophysical Properties of Substituted Homoleptic and Heteroleptic Phenylimidazolinato Ir(III) Complexes as a Blue Phosphorescent Material. *Inorg. Chem.* **2013**, *52*, 12338.
- 67 Fernandez-Hernández, J. M.; Beltran, J. I.; Lemaun, V.; Galvez-Lopez, M.-D.; Chien, C.-H.; Polo, F.; Orselli, E.; Fröhlich, R.; Cornil, J.; De Cola, L. Iridium(III) Emitters Based on 1,4-Disubstituted-1H-1,2,3-triazoles as Cyclometalating Ligand: Synthesis, Characterization, and Electroluminescent Devices. *Inorg. Chem.* **2013**, *52*, 1812.
- 68 Krylova, V. A.; Djurovich, P. I.; Conley, B. L.; Haiges, R.; Whited, M. T.; Williams, T. J.; Thompson, M. E. Control of Emission Colour with N-Heterocyclic Carbene (NHC) Ligands in Phosphorescent Three-Coordinate Cu(I) complexes. *Chem. Commun.* **2014**, *50*, 7176.
- 69 Greiner, H. Light Extraction from Organic Light Emitting Diode Substrates: Simulation and Experiment. *Jpn. J. Appl. Phys.* **2007**, *46*, 4125.
- 70 Reineke, S.; Lindner, F.; Schwartz, G.; Seidler, N.; Walzer, K.; Lussem, B.; Leo, K. White Organic Light-Emitting Diodes with Fluorescent Tube Efficiency. *Nature* **2009**, *459*, 234.
- 71 Yersin, H. Organometallic Triplet Emitters for OLED Applications. Controlling of Emission Properties by Chemical Variation. *P. SPIE* **2003**, *5214*, 124.
- 72 Yersin, H. Triplet Emitters for OLED Applications. Mechanisms of Exciton Trapping and Control of Emission Properties. *Top. Curr. Chem.* **2004**, *241*, 1.

- 73 Hellwege, K. H., *Einführung in die Festkörperphysik*; Springer-Verlag: Berlin, Germany, 1976, p 509.
- 74 Donges, D.; Nagle, J. K.; Yersin, H. Intraligand Charge Transfer in Pt(qol)<sub>2</sub>. Characterization of Electronic States by High-Resolution Shpol'skii Spectroscopy. *Inorg. Chem.* **1997**, *36*, 3040.
- 75 Yersin, H.; Donges, D.; Nagle, J. K.; Sitters, R.; Glasbeek, M. Intraligand Charge Transfer in the Pd(II) Oxinate Complex Pd(qol)<sub>2</sub>. Site-Selective Emission, Excitation, and Optically Detected Magnetic Resonance. *Inorg. Chem.* **2000**, *39*, 770.
- 76 Yersin, H.; Donges, D. Low-Lying Electronic States and Photophysical Properties of Organometallic Pd(II) and Pt(II) Compounds. Modern Research Trends Presented in Detailed Case Studies. *Top. Curr. Chem.* **2001**, *214*, 81.
- 77 Hedley, G. J.; Ruseckas, A.; Samuel, I. D. W. Ultrafast Luminescence in Ir(ppy)<sub>3</sub>. *Chem. Phys. Lett.* **2008**, *450*, 292.
- 78 Hsu, C.-W.; Lin, C.-C.; Chung, M.-W.; Chi, Y.; Lee, G.-H.; Chou, P.-T.; Chang, C.-H.; Chen, P.-Y. Systematic Investigation of the Metal-Structure-Photophysics Relationship of Emissive d<sup>10</sup>-Complexes of Group 11 Elements: The Prospect of Application in Organic Light Emitting Devices. *J. Am. Chem. Soc.* **2011**, *133*, 12085.
- 79 Tschierlei, S.; Karnahl, M.; Rockstroh, N.; Junge, H.; Beller, M.; Lochbrunner, S. Substitution-Controlled Excited State Processes in Heteroleptic Copper(I) Photosensitizers Used in Hydrogen Evolving Systems. *Chem. Phys. Chem* **2014**, *15*, 3709.
- 80 Constable, E. C.; Ertl, C. D.; Housecroft, C. E.; Zampese, J. A. Green-Emitting Iridium(III) Complexes Containing Culfanyl- or Sulfone-Functionalized Cyclometallating 2-Phenylpyridine Ligands. *Dalton T.* **2014**, *43*, 5343.
- 81 Osawa, M. Highly Efficient Blue-Green Delayed Fluorescence from Copper(I) Thiolate Complexes: Luminescence Color Alteration by Orientation Change of the Aryl Ring. *Chem. Commun.* **2014**, *50*, 1801.
- 82 Parker, C. A.; Hatchard, C. G. Triplet-Singlet Emission in Fluid Solutions. Phosphorescence of Eosin. *T. Faraday Soc.* **1961**, *57*, 1894.

- 83 Rausch, A. Der Einfluss von Molekülstruktur und Matrix auf die Emissionseigenschaften phosphoreszierender Übergangsmetallkomplexe für OLED-Anwendungen., Ph.D. Thesis, Universität Regensburg, 2011.
- 84 Czerwieniec, R.; Leitl, M.; Yersin, H. Optische Sauerstoff-Sensoren mit Kupfer(I)-Komplexen., DE 10 2012 101067 A1, 2012.
- 85 Ford, P. C. Photochemical and Photophysical Studies of Tetranuclear Copper(I) Halide Clusters: An Overview. *Coord. Chem. Rev.* **1994**, *132*, 129.
- 86 Iwamura, M.; Watanabe, H.; Ishii, K.; Takeuchi, S.; Tahara, T. Coherent Nuclear Dynamics in Ultrafast Photoinduced Structural Change of Bis(diimine)copper(I) Complex. *J. Am. Chem. Soc.* **2011**, *133*, 7728.
- 87 Hua, L.; Iwamura, M.; Takeuchi, S.; Tahara, T. Substituent Effect on the MLCT Excited State Dynamics of Cu(I) Complexes Studied by Femtosecond Time-Resolved Absorption and Observation of Coherent Nuclear Wavepacket Motion. *Phys. Chem. Chem. Phys.* **2015**, *17*, 2067.
- 88 Rausch, A. F.; Homeier, H. H. H.; Yersin, H. Organometallic Pt(II) and Ir(III) Triplet Emitters for OLED Applications and the Role of Spin-Orbit Coupling: A Study Based on High-Resolution Optical Spectroscopy. *Top. Organomet. Chem.* **2010**, *29*, 193.
- 89 Azumi, T.; O'Donnell, C. M.; McGlynn, S. P. On the Multiplicity of the Phosphorescent State of Organic Molecules. *J. Chem. Phys.* **1966**, *45*, 2735.
- 90 Cunningham, C. T.; Moore, J. J.; Cunningham, K. L. H.; Fanwick, P. E.; McMillin, D. R. Structural and Photophysical Studies of Cu(NN)<sup>2+</sup> Systems in the Solid State. Emission at Last from Complexes with Simple 1,10-Phenanthroline Ligands. *Inorg. Chem.* **2000**, *39*, 3638.
- 91 Felder, D.; Nierengarten, J.-F.; Barigelletti, F.; Ventura, B.; Armaroli, N. Highly Luminescent Cu(I)-Phenanthroline Complexes in Rigid Matrix and Temperature Dependence of the Photophysical Properties. *J. Am. Chem. Soc.* **2001**, *123*, 6291.
- 92 Siddique, Z. A.; Yamamoto, Y.; Ohno, T.; Nozaki, K. Structure-Dependent Photophysical Properties of Singlet and Triplet Metal-to-Ligand Charge Transfer States in Copper(I) Bis(diimine) Compounds. *Inorg. Chem.* **2003**, *42*, 6366.

- 93 Shaw, G. B.; Grant, C. D.; Shirota, H.; Castner, E. W.; Meyer, G. J.; Chen, L. X. Ultrafast Structural Rearrangements in the MLCT Excited State for Copper(I) bis-Phenanthrolines in Solution. *J. Am. Chem. Soc.* **2007**, *129*, 2147.
- 94 Vorontsov, I. I.; Graber, T.; Kovalevsky, A. Y.; Novozhilova, I. V.; Gembicky, M.; Chen, Y.-S.; Coppens, P. Capturing and Analyzing the Excited-State Structure of a Cu(I) Phenanthroline Complex by Time-Resolved Diffraction and Theoretical Calculations. *J. Am. Chem. Soc.* **2009**, *131*, 6566.
- 95 Linfoot, C. L.; Richardson, P.; Hewat, T. E.; Moudam, O.; Forde, M. M.; Collins, A.; White, F.; Robertson, N. Substituted [Cu(I)(POP)(bipyridyl)] and Related Complexes: Synthesis, Structure, Properties and Applications to Dye-Sensitised Solar Cells. *Dalton T.* **2010**, *39*, 8945.
- 96 Coppens, P.; Sokolow, J.; Trzop, E.; Makal, A.; Chen, Y. On the Biexponential Decay of the Photoluminescence of the Two Crystallographically-Independent Molecules in Crystals of [Cu(I)(phen)(PPh<sub>3</sub>)<sub>2</sub>][BF<sub>4</sub>]. *J. Phys. Chem. Lett.* **2013**, *4*, 579.
- 97 Bergmann, L.; Friedrichs, J.; Mydlak, M.; Baumann, T.; Nieger, M.; Bräse, S. Outstanding Luminescence from Neutral Copper(I) Complexes with Pyridyl-Tetrazolate and Phosphine Ligands. *Chem. Commun.* **2013**, *49*, 6501.
- 98 Nishikawa, M.; Sawamura, S.; Haraguchi, A.; Morikubo, J.; Takao, K.; Tsubomura, T. Highly Emissive Copper(I) Complexes Bearing Diimine and bis(diphenylphosphinomethyl)-2,2-dimethyl-1,3-dioxolane. *Dalton T.* **2015**, *44*, 411.
- 99 Keller, S.; Constable, E. C.; Housecroft, C. E.; Neuburger, M.; Prescimone, A.; Longo, G.; Pertegas, A.; Sessolo, M.; Bolink, H. J. [Cu(bpy)(PP)]<sup>+</sup> Containing Light-Emitting Electrochemical Cells: Improving Performance Through Simple Substitution. *Dalton T.* **2014**, *43*, 16593.
- 100 Liu, Z.; Djurovich, P. I.; Whited, M. T.; Thompson, M. E. Cu<sub>4</sub>I<sub>4</sub> Clusters Supported by PN-type Ligands: New Structures with Tunable Emission Colors. *Inorg. Chem.* **2012**, *51*, 230.
- 101 Tsuge, K. Luminescent Complexes Containing Halogeno-bridged Dicopper(I) Unit [Cu<sub>2</sub>(μ-X)<sub>2</sub>] (X = Cl, Br, and I). *Chem. Lett.* **2013**, *42*, 204.

- 102 Zink, D. M.; Bächle, M.; Baumann, T.; Nieger, M.; Kuhn, M.; Wang, C.; Klopfer, W.; Monkowius, U.; Hofbeck, T.; Yersin, H.; Bräse, S. Synthesis, Structure, and Characterization of Dinuclear Copper(I) Halide Complexes with PN Ligands Featuring Exciting Photoluminescence Properties. *Inorg. Chem.* **2013**, *52*, 2292.
- 103 Zink, D. M.; Baumann, T.; Friedrichs, J.; Nieger, M.; Bräse, S. Copper(I) Complexes Based on Five-Membered PN Heterocycles: Structural Diversity Linked to Exciting Luminescence Properties. *Inorg. Chem.* **2013**, *52*, 13509.
- 104 Zink, D. M.; Bergmann, L.; Ambrosek, D.; Wallesch, M.; Volz, D.; Mydlak, M. Singlet Harvesting Copper-Based Emitters: A Modular Approach Towards Next-Generation OLED Technology. *Transl. Mater. Res.* **2014**, *1*, 015003.
- 105 Maini, L.; Mazzeo, P. P.; Farinella, F.; Fattori, V.; Braga, D. Mechanochemical Preparation of Copper Iodide Clusters of Interest for Luminescent Devices. *Farad. Discuss.* **2014**, *170*, 93.
- 106 Hofbeck, T.; Monkowius, U.; Yersin, H. Highly Efficient Luminescence of Cu(I) Compounds – TADF Combined with Short-Lived Phosphorescence. *J. Am. Chem. Soc.* **2014**, *137*, 399.
- 107 Jesser, A.; Rohrmüller, M.; Schmidt, W. G.; Herres-Pawlis, S. Geometrical and Optical Benchmarking of Copper Guanidine-Quinoline Complexes: Insights from TD-DFT and Many-Body Perturbation Theory. *J. Comput. Chem.* **2014**, *35*, 1.
- 108 Arnby, C. H.; Jagner, S.; Dance, I. Questions for Crystal Engineering of Halocuprate Complexes: Concepts for a Difficult System. *Cryst. Eng. Comm.* **2004**, *6*, 257.
- 109 Dexter, D. L.; Schulman, J. H. Theory of Concentration Quenching in Inorganic Phosphors. *J. Chem. Phys.* **1954**, *22*, 1063.
- 110 Sakaki, S.; Mizutani, H.; Kase, Y. Geometry, Electronic Structure, and Coordination Ability of  $[\text{Cu}(\text{diN})(\text{PH}_3)_2]^+$  (diN = HN=4HCH=NH) at the Lowest Energy Triplet Metal-to-Ligand Charge-Transfer Excited State. A Theoretical Study. *Inorg. Chem.* **1992**, *31*, 4575.
- 111 Rössler, U.; Yersin, H. Destabilization of a Self-Trapped Exciton in a Quasi-One-Dimensional Semiconductor:  $\text{Mg}[\text{Pt}(\text{CN})_4] \cdot 7\text{H}_2\text{O}$  with Hydrostatic Pressure. *Phys. Rev. B* **1982**, *26*, 3187.

- 112 Schläfer, H.; Gliemann, G., *Basic Principles of Ligand Field Theory*; Wiley-Interscience: New York, 1969.
- 113 Hill, M. G.; Bailey, J. A.; Miskowski, V. M.; Gray, H. B. Spectroelectrochemistry and Dimerization Equilibria of Chloro(terpyridine)platinum(II). Nature of the Reduced Complexes. *Inorg. Chem.* **1996**, *35*, 4585.
- 114 Atkins, P.; Friedman, R., *Molecular Quantum Mechanics*; Oxford University Press: Oxford, 2010.
- 115 Nozaki, K. Theoretical Studies on Photophysical Properties and Mechanism of Phosphorescence in [fac-Ir(2-phenylpyridine)<sub>3</sub>]. *J. Chin. Chem. Soc.* **2006**, *53*, 101.
- 116 Rausch, A. F.; Homeier, H. H. H.; Djurovich, P. I.; Thompson, M. E.; Yersin, H. Spin-Orbit Coupling Routes and OLED Performance – Studies of Blue Light Emitting Ir(III) and Pt(II) Complexes. *P. SPIE* **2007**, *6655*, 66550F.
- 117 Tinti, D. S.; El-Sayed, M. A. New Techniques in Triplet State Phosphorescence Spectroscopy: Application to the Emission of 2,3-Dichloroquinoxaline. *J. Chem. Phys.* **1971**, *54*, 2529.
- 118 Rausch, A. F.; Thompson, M. E.; Yersin, H. Triplet State Relaxation Processes of the OLED Emitter Pt(4,6-dFppy)(acac). *Chem. Phys. Lett.* **2009**, *468*, 46.
- 119 Finkenzeller, W. J.; Stöbel, P.; Yersin, H. Emission and Absorption of Ir(ppy)<sub>2</sub>(CO)(Cl) – Temperature Dependence, Phosphorescence Decay Dynamics, and Assignment of Excited States. *Chem. Phys. Lett.* **2004**, *397*, 289.
- 120 Czerwieniec, R.; Finkenzeller, W. J.; Hofbeck, T.; Starukhin, A.; Wedel, A.; Yersin, H. Photophysical Properties of Re(pbt)(CO)<sub>4</sub> Studied by High Resolution Spectroscopy. *Chem. Phys. Lett.* **2009**, *468*, 205.
- 121 Schmidt, J.; Wiedenhofer, H.; von Zelewsky, A.; Yersin, H. Time-Resolved Vibrational Structures of the Triplet Sublevel Emission of Pd(2-thpy)<sub>2</sub>. *J. Phys. Chem.* **1995**, *99*, 226.
- 122 Fischer, T.; Czerwieniec, R.; Hofbeck, T.; Osminina, M. M.; Yersin, H. Triplet State Properties of a Red Light Emitting [Pt(s-thpy)(acac)] Compound. *Chem. Phys. Lett.* **2010**, *486*, 53.

- 123 Rausch, A. F.; Monkowius, U. V.; Zabel, M.; Yersin, H. Bright Sky-Blue Phosphorescence of  $[\text{n-Bu}_4\text{N}][\text{Pt}(4,6\text{-dFppy})(\text{CN})_2]$ : Synthesis, Crystal Structure, and Detailed Photophysical Studies. *Inorg. Chem.* **2010**, *49*, 7818.
- 124 Manenkov, A.; Orbach, R., *Spin-Lattice Relaxation in Ionic Solids*; Harper & Row: New York, NY, United States, 1966.
- 125 Abragam, A.; Bleaney, B., *Electron Paramagnetic Resonance of Transition Ions*; Clarendon Press: Oxford, United Kingdom, 1970.
- 126 Henderson, B.; Imbusch, G., *Optical Spectroscopy of Inorganic Solids*; Clarendon Press: Oxford, United Kingdom, 1989.
- 127 Obara, S.; Itabashi, M.; Okuda, F.; Tamaki, S.; Tanabe, Y.; Ishii, Y.; Nozaki, K.; Haga, M.-a. Highly Phosphorescent Iridium Complexes Containing Both Tridentate Bis(benzimidazolyl)-benzene or -pyridine and Bidentate Phenylpyridine: Synthesis, Photophysical Properties, and Theoretical Study of Ir-Bis(benzimidazolyl)benzene Complex. *Inorg. Chem.* **2006**, *45*, 8907.
- 128 Jansson, E.; Minaev, B.; Schrader, S.; Ågren, H. Time-Dependent Density Functional Calculations of Phosphorescence Parameters for fac-tris(2-phenylpyridine) Iridium. *Chem. Phys.* **2007**, *333*, 157.
- 129 Jacko, A. C.; McKenzie, R. H.; Powell, B. J. Models of Organometallic Complexes for Optoelectronic Applications. *J. Mater. Chem.* **2010**, *20*, 10301.
- 130 Murov, S.; Hug, G.; Carmichael, I., *Handbook of Photochemistry*, 2nd edition; Marcel Dekker: New York, NY, United States, 1993, pp 339–341.
- 131 Li, X.; Minaev, B.; Ågren, H.; Tian, H. Theoretical Study of Phosphorescence of Iridium Complexes with Fluorine-Substituted Phenylpyridine Ligands. *Eur. J. Inorg. Chem.* **2011**, *2011*, 2517.
- 132 Osawa, M.; Hoshino, M.; Hashimoto, M.; Kawata, I.; Igawa, S.; Yashima, M. Application of Three-Coordinate Copper(I) Complexes with Halide Ligands in Organic Light-Emitting Diodes that Exhibit Delayed Fluorescence. *Dalton T.* **2015**, DOI: 10.1039/C4DT02853H.
- 133 *D'Ans-Lax Taschenbuch für Chemiker und Physiker, Band III: Eigenschaften von Atomen und Molekülen*; Schäfer, K., Synowietz, C., Eds.; Springer-Verlag: Berlin, Germany, 1970.

- 134 Femoni, C.; Muzzioli, S.; Palazzi, A.; Stagni, S.; Zacchini, S.; Monti, F.; Accorsi, G.; Bolognesi, M.; Armaroli, N.; Massi, M.; Valenti, G.; Marcaccio, M. New Tetrazole-Based Cu(I) Homo- and Heteroleptic Complexes with Various PP Ligands: Synthesis, Characterization, Redox and Photophysical Properties. *Dalton T.* **2013**, *42*, 997.
- 135 Manbeck, G. F.; Brennessel, W. W.; Eisenberg, R. Photoluminescent Copper(I) Complexes with Amido-Triazolato Ligands. *Inorg. Chem.* **2011**, *50*, 3431.
- 136 Wada, A.; Zhang, Q.; Yasuda, T.; Takasu, I.; Enomoto, S.; Adachi, C. Efficient Luminescence from a Copper(I) Complex Doped in Organic Light-Emitting Diodes by Suppressing C-H Vibrational Quenching. *Chem. Commun.* **2012**, *48*, 5340.
- 137 Armaroli, N.; Accorsi, G.; Holler, M.; Moudam, O.; Nierengarten, J. F.; Zhou, Z.; Wegh, R. T.; Welter, R. Highly Luminescent Cu(I) Complexes for Light-Emitting Electrochemical Cells. *Adv. Mater.* **2006**, *18*, 1313.
- 138 Krylova, V. A.; Djurovich, P. I.; Whited, M. T.; Thompson, M. E. Synthesis and Characterization of Phosphorescent Three-Coordinate Cu(I)-NHC Complexes. *Chem. Commun.* **2010**, *46*, 6696.
- 139 Krylova, V. A.; Djurovich, P. I.; Aronson, J. W.; Haiges, R.; Whited, M. T.; Thompson, M. E. Structural and Photophysical Studies of Phosphorescent Three-Coordinate Copper(I) Complexes Supported by an N-Heterocyclic Carbene Ligand. *Organometallics* **2012**, *31*, 7983.
- 140 Volz, D.; Nieger, M.; Friedrichs, J.; Baumann, T.; Bräse, S. How the Quantum Efficiency of a Highly Emissive Binuclear Copper Complex is Enhanced by Changing the Processing Solvent. *Langmuir* **2013**, *29*, 3034.
- 141 Benito, Q.; Le Goff, X. F.; Maron, S.; Fargues, A.; Garcia, A.; Martineau, C.; Taulelle, F.; Kahlal, S.; Gacoin, T.; Boilot, J.-P.; Perruchas, S. Polymorphic Copper Iodide Clusters: Insights into the Mechanochromic Luminescence Properties. *J. Am. Chem. Soc.* **2014**, *136*, 11311.
- 142 Volz, D.; Wallesch, M.; Grage, S. L.; Göttlicher, J.; Steininger, R.; Batchelor, D.; Vitova, T.; Ulrich, A. S.; Heske, C.; Weinhardt, L.; Baumann, T.; Bräse, S. Labile or Stable: Can Homoleptic and Heteroleptic PyrPHOS-Copper Complexes be Processed from Solution? *Inorg. Chem.* **2014**, *53*, 7837.



- 143 Harrigan, R. W.; Crosby, G. A. Symmetry Assignments of the Lowest CT Excited States of Ruthenium (II) Complexes via a Proposed Electronic Coupling Model. *J. Chem. Phys.* **1973**, *59*, 3468.
- 144 Zhang, Q.; Komino, T.; Huang, S.; Matsunami, S.; Goushi, K.; Adachi, C. Triplet Exciton Confinement in Green Organic Light-Emitting Diodes Containing Luminescent Charge-Transfer Cu(I) Complexes. *Adv. Funct. Mater.* **2012**, *22*, 2327.
- 145 Yersin, H.; Strasser, J. Triplets in Metal-Organic Compounds. Chemical Tunability of Relaxation Dynamics. *Coord. Chem. Rev.* **2000**, *208*, 331.
- 146 Bossi, A.; Rausch, A. F.; Leitl, M. J.; Czerwieniec, R.; Whited, M. T.; Djurovich, P. I.; Yersin, H.; Thompson, M. E. Photophysical Properties of Cyclometalated Pt(II) Complexes: Counterintuitive Blue Shift in Emission with an Expanded Ligand  $\pi$  System. *Inorg. Chem.* **2013**, *52*, 12403.
- 147 Valiev, M.; Bylaska, E. J.; Govind, N.; Kowalski, K.; Straatsma, T. P.; Van Dam, H. J. J.; Wang, D.; Nieplocha, J.; Apra, E.; Windus, T. L.; de Jong, W. A. NWChem: A Comprehensive and Scalable Open-Source Solution for Large Scale Molecular Simulations. *Comput. Phys. Commun.* **2010**, *181*, 1477.
- 148 Becke, A. D. Density-Functional Thermochemistry. III. The Role of Exact Exchange. *J. Chem. Phys.* **1993**, *98*, 5648.
- 149 Weigend, F.; Ahlrichs, R. Balanced Basis Sets of Split Valence, Triple Zeta Valence and Quadruple Zeta Valence Quality for H to Rn: Design and Assessment of Accuracy. *Phys. Chem. Chem. Phys.* **2005**, *7*, 3297.



## Danksagung

An dieser Stelle bedanke ich mich bei allen Kollegen, Freunden und Familienmitgliedern, die mich während meiner Promotion unterstützt haben. Mein Dank gilt ...

...insbesondere Prof. Dr. Hartmut Yersin für die Möglichkeit, meine Dissertation in seiner Arbeitsgruppen anzufertigen. Die intensive Betreuung sowie die zahlreichen offenen und ausführlichen Diskussionen habe ich sehr geschätzt.

...Prof. Dr. Bernhard Dick für die Möglichkeit, am Lehrstuhl für Physikalische und Theoretische Chemie zu arbeiten, für die Bereitstellung der für die Forschung nötigen Infrastruktur sowie für die Einblicke in andere Forschungsgebiete und die interessanten Diskussionen im Rahmen der Lehrstuhlseminare.

...allen aktuellen und ehemaligen Mitgliedern der Arbeitsgruppe von Prof. Dr. Hartmut Yersin, vor allem Dr. Thomas Hofbeck für die Unterstützung bei der Lösung experimenteller und technischer Probleme, Dr. Rafał Czerwieniec und Dr. Natalia-Larisa Mataranga-Popa für die Hilfe bei chemischen Fragestellungen sowie Dr. Andreas Rausch für die Unterstützung beim Start in die Promotion. Außerdem danke ich M.Sc. Alexander Schinabeck, M.Sc. Oliver Masur, M.Sc. Axel Bolz, Dipl.-Phys. Alexander Hupfer und Dr. Tobias Fischer für die vielen wissenschaftlichen Diskussionen, aber auch für die unwissenschaftlichen Gespräche und Kaffeerunden, die manchmal notwendig sind, um den Kopf wieder frei zu kriegen.

... allen Kooperationspartnern für die konstruktive und erfolgreiche Zusammenarbeit. Insbesondere bedanke ich mich bei Prof. Dr. Mark E. Thompson (University of Southern California, Los Angeles) und den Mitgliedern seiner Arbeitsgruppe, vor allem Prof. Dr. Peter I. Djurovich und Dr. Valentina A. Krylova, für die interessanten wissenschaftlichen Diskussionen sowie für die große Gastfreundschaft während meiner Aufenthalte an der USC, bei Prof. Dr. Jörg Sundermeyer und seinem Mitarbeiter M.Sc. Timo Gneuß (Universität Marburg) für die intensive und erfolgreiche Zusammenarbeit in den letzten Jahren, bei Prof. Dr. Josef Breu, Dr. Daniel Kunz und M.Sc. Matthias Stöter (Universität Bayreuth), sowie Dr. Lukas Schade (IAF Freiburg) für die Bereitstellung und die Untersuchung eines spannenden Materialsystems für polarisierte Emission, bei Prof. Dr. Lars Wesemann und Prof. Dr. Hermann A. Mayer (Universität Tübingen) sowie den Mitgliedern ihrer Arbeitsgruppen für die erfolgreiche mehrjährige Zusammenarbeit.

... allen wissenschaftlichen und nicht-wissenschaftlichen Mitarbeitern des Lehrstuhls für Physikalische und Theoretisch Chemie für das angenehme Arbeitsklima.

... Randy Rückner für die Unterstützung bei der Nutzung des High Performance Computing Clusters des Rechenzentrums der Universität Regensburg.

... allen Mitarbeitern der Mechanik- und Elektronikwerkstatt sowie der Glasbläserei für die schnelle und professionelle Ausführung aller Aufträge.

... meiner Familie und meinen Freunden, insbesondere meiner Freundin Kathrin, die mich während meiner Zeit an der Universität Regensburg immer in allen Belangen unterstützt haben und ohne die das Studium und die Promotion nur halb soviel Spaß gemacht hätte.

Vielen Dank euch allen!!!

## Erklärung

Ich versichere hiermit, dass ich die vorliegende Arbeit selbst verfasst und keine anderen als die angegebenen Quellen und Hilfsmittel verwendet habe.

Regensburg, den \_\_\_\_\_

\_\_\_\_\_  
Markus Leitl